POLITECNICO DI TORINO

Master Degree course in Communications Engineering

Master Degree Thesis

Comparison between OFDM and OTFS communication techniques for 6G applications

Supervisors
Prof. Carla Fabiana Chiasserini
Ing. Alessandro Nordio

Candidate
Andrea Conese

Academic Year 2024-2025

Acknowledgements

First and foremost, I would like to thank **Professor Carla Fabiana Chiasserini**, my supervisor, and **Alessandro Nordio**, my co-supervisor, for giving me the opportunity to carry out this thesis work. I am deeply grateful for their availability, dedication, and continuous support throughout this journey.

A special thank you goes to my **family**, who made it possible for me to complete my studies away from home, never letting me miss anything and always supporting me in every moment.

My heartfelt thanks also go to all my **friends**, whether near or far, because each of them has contributed in some way to making my days brighter with a laugh, a piece of advice, or simply their presence.

A warm thought to my second family, **Pier** and **Marco**, with whom, despite everything, we somehow managed not to set the house on fire!

A special thanks to **Andrea**, who, from day zero of my arrival in Turin, has been a companion in study, adventures, and countless shared experiences over these two years.

Finally, I want to thank **myself**, for the determination, commitment, and strength that allowed me to make it this far.

Abstract

The development of 6G wireless networks demands more robust, efficient, and reliable communication technologies to support emerging applications such as autonomous systems, holographic communications, and Internet of Things (IoT). This thesis explores and compares two prominent modulation techniques: Orthogonal Frequency Division Multiplexing (OFDM) and Orthogonal Time Frequency Space (OTFS), with a focus on their suitability for 6G communication systems. The theoretical analysis of both techniques is presented, highlighting their respective strengths, weaknesses, and performance in challenging high-mobility environments. OFDM, a widely adopted technique in 4G and 5G systems, is known for its high spectral efficiency but suffers from severe performance degradation due to Doppler shifts in fast-moving channels. On the other hand, OTFS, a more recent modulation scheme, is designed to mitigate the impact of Doppler shift by operating in the delay-Doppler domain. This thesis provides a comprehensive comparison of the two techniques, offering insights into their potential advantages for 6G applications. Furthermore, laboratory experiments and MATLAB simulations are conducted to validate the theoretical findings and demonstrate the practical performance of OFDM and OTFS in realistic wireless communication scenarios. The results indicate that OTFS offers superior robustness in high-mobility environments, making it a promising candidate for future wireless systems.

Contents

List of Figures

List of Tables

Acronyms

5G Fifth Generation

6G Sixth Generation

OFDM Orthogonal Frequency Division Multiplexing

OTFS Orthogonal Time Frequency Space

MIMO Multiple Input Multiple Output

LTE Long Term Evolution

NR New Radio

NOMA Non-Orthogonal Multiple Access

SDMA Space Division Multiple Access

TDMA Time Division Multiple Access

FDMA Frequency Division Multiple Access

SC-FDMA Single Carrier Frequency Division Multiple Access

QAM Quadrature Amplitude Modulation

QPSK Quadrature Phase Shift Keying

PSK Phase Shift Keying

QAM Quadrature Amplitude Modulation

BPSK Binary Phase Shift Keying

IoT Internet of Things

SNR Signal-to-Noise Ratio

DFT Discrete Fourier Transform

IFFT Inverse Fast Fourier Transform

FFT Fast Fourier Transform

DZT Discrete Zak Transform

IDZT Inverse Discrete Zak Transform

ZT Zak Transform

ZC Zero-Crossing

Chapter 1

Introduction

The rapid evolution of wireless communication technologies continues to reshape modern society, driving an ever-growing demand for networks that are not only faster and more efficient, but also capable of supporting a wide range of advanced and critical applications. As digital infrastructure becomes increasingly embedded in daily life, the expectations placed on wireless networks rise significantly. The shift from 4G to 5G has already demonstrated substantial improvements in terms of data throughput, latency reduction, and overall network capacity. Yet, even these advancements are beginning to approach their functional limits in the face of emerging demands for ultra-reliable, low-latency communication (URLLC), ubiquitous connectivity, and support for massive-scale device deployment.

Looking ahead, the sixth generation (6G) of wireless communication systems is expected to play a pivotal role in enabling revolutionary technologies. These include autonomous transportation systems, real-time immersive experiences such as holographic telepresence, and a fully interconnected Internet of Things (IoT) ecosystem. To meet such demanding requirements, future networks must guarantee extremely high data rates, near-instantaneous response times, and robust performance even under challenging propagation conditions. As such, 6G is not merely a generational upgrade, but a fundamental rethinking of how wireless communication should be designed to support a hyper-connected, intelligent society.

Achieving these goals, however, entails addressing numerous technical challenges—one of the most critical being the efficient management of the wireless channel. Wireless propagation is inherently affected by impairments such as multipath fading, interference, and Doppler shifts, with the latter posing significant issues in high-mobility scenarios like vehicular or aerial communication. The current state-of-the-art modulation scheme, Orthogonal Frequency Division Multiplexing (OFDM), has proven effective in mitigating frequency-selective fading in low-to-moderate mobility environments. Nonetheless, its reliance on strict subcarrier orthogonality renders it vulnerable to Doppler-induced distortions, which degrade performance through inter-carrier interference (ICI).

In response to these limitations, the research community has proposed a novel modulation technique known as Orthogonal Time Frequency Space (OTFS). Unlike OFDM, OTFS maps information symbols onto the delay-Doppler domain rather than the time-frequency

domain. This unique approach takes advantage of the sparse nature of wireless channels in the delay-Doppler representation, offering enhanced robustness against mobility-induced impairments and time-variant fading. By effectively converting a rapidly varying channel into a quasi-static form, OTFS introduces a paradigm shift in the way modulation is conceptualized, particularly in high-mobility environments.

This thesis is motivated by the pressing need to identify and evaluate modulation strategies that can sustain the ambitious performance targets of future 6G networks. In particular, it seeks to determine whether OTFS presents a viable and superior alternative to OFDM under realistic channel conditions, especially in high-mobility scenarios. The study is grounded in both theoretical analysis and practical validation. It presents a comparative evaluation of OFDM and OTFS, focusing on critical performance metrics such as bit error rate (BER) and resilience to Doppler effects.

Through MATLAB-based simulations and controlled laboratory experiments, this research aims to contribute to the growing body of knowledge on next-generation wireless modulation techniques. The insights obtained are expected to assist engineers, researchers, and system designers in making informed decisions regarding physical layer strategies for 6G systems. By highlighting the limitations of existing methods and exploring innovative alternatives, this work aspires to play a small but meaningful role in shaping the future of wireless communication.

Chapter 2

Wireless Communication Channel

A **wireless channel** refers to the medium through which electromagnetic waves propagate to enable communication between a transmitter and a receiver. Unlike wired channels, which rely on physical conductors, wireless channels are affected by various factors such as path loss, fading, interference, and noise. These factors can cause signal degradation and variability over time and frequency. Wireless channels can be classified based on their characteristics, including **line-of-sight (LoS)** and **non-line-of-sight (NLoS)** propagation.
In the following sections, some key aspects necessary for a deeper understanding of the discussion will be analyzed in more detail.

2.1 Frequency response and spectrum

In a linear time-invariant (LTI) wireless channel, the relationship between the power spectral densities (PSD) of the transmitted signal $s(t)$ and the received signal $r(t)$ is given by:

$$G_r(f) = |H(f)|^2 \cdot G_s(f) \tag{2.1}$$

where:

- $G_s(f)$ is the power spectral density (PSD) of the transmitted signal $s(t)$,
- $G_r(f)$ is the power spectral density (PSD) of the received signal $r(t)$,
- $H(f)$ is the channel frequency response, representing the effect of the channel on different frequency components,
- $|H(f)|^2$ is the channel's power gain, indicating how the channel attenuates or amplifies the transmitted signal at each frequency.

The PSD of the output signal is given by the PSD of the input signal multiplied by the squared magnitude of the system's frequency response.
The equation highlights that in a **flat fading channel**, where $|H(f)|$ is approximately constant over the signal bandwidth, all frequency components experience the same gain

or attenuation. However, in a **frequency-selective fading channel**, different frequency components are affected differently due to variations in $H(f)$, so in order to have $r(t) = s(t)$, $|H(f)|^2$ should be flat.

It is important to underline that the signal is transmitted only inside the band B which is assigned to the communication channel and not over the entire frequency axis, this means that the frequency response $|H(f)|^2$ should be flat inside B.

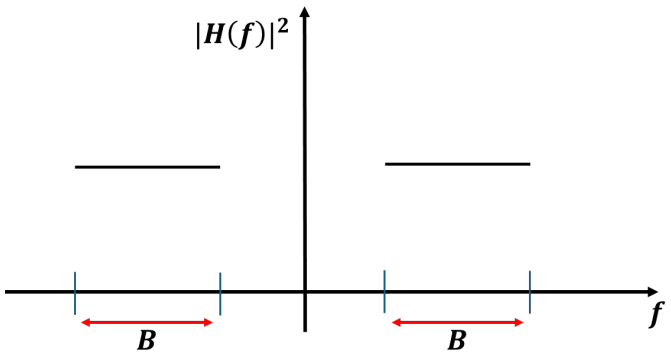

Figure 2.1: Frequency response flat inside B.

2.1.1 Fading

The dynamic nature of the transmission medium, usually in wireless communication systems, causes a received signal's intensity to fluctuate over time, distance, or frequency. This phenomenon is known as **fading**. Multiple processes, including radio waves' reflection, diffraction, and scattering as they move through the environment, contribute to their occurrence. As the signal travels to the receiver, these factors cause it to vary, which can result in signal attenuation or, in certain situations, deep fades where the signal may be lost entirely. There are two main forms of fading: **large-scale fading** (gradual variations over greater distances) and **small-scale fading** (rapid fluctuations over short distances or time periods). Designing reliable communication systems requires an understanding of fading, which impacts wireless link performance and signal quality.

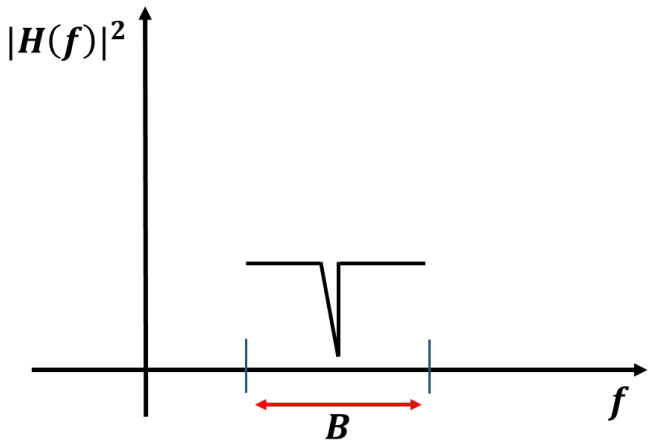

Figure 2.2: Fading.

2.2 Flat Fading vs. Frequency Selective Fading

From a frequency domain perspective, fading can be categorized into two main types:

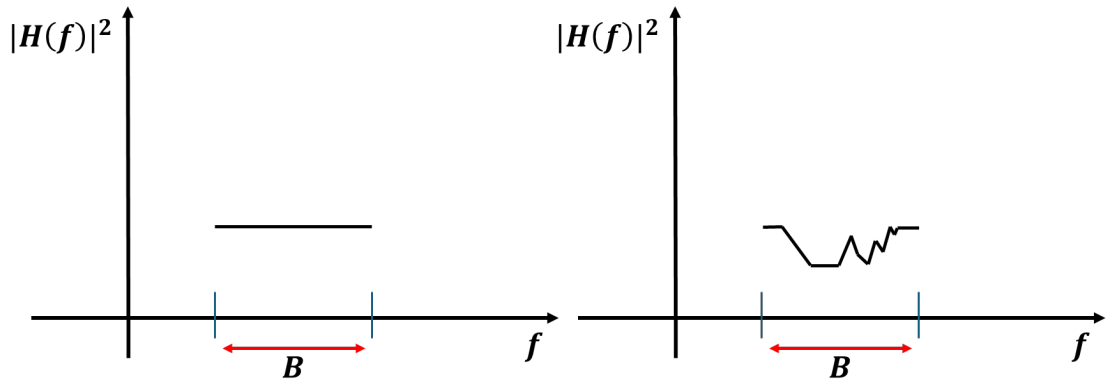

Figure 2.3: Flat Fading vs. Frequency Selective Fading inside B.

FLAT FADING

All of the signal's frequency components suffer from the same fading effects when the signal's bandwidth is small in comparison to the channel's coherence bandwidth. This phenomenon is known as flat fading. In this instance, the channel has a consistent effect on the entire signal, either attenuating or amplifying it. The entire signal may be greatly weakened or momentarily lost if there is a deep fade at the frequency. Flat fading, as contrast to frequency-selective fading, only affects the signal's amplitude rather than its structure.

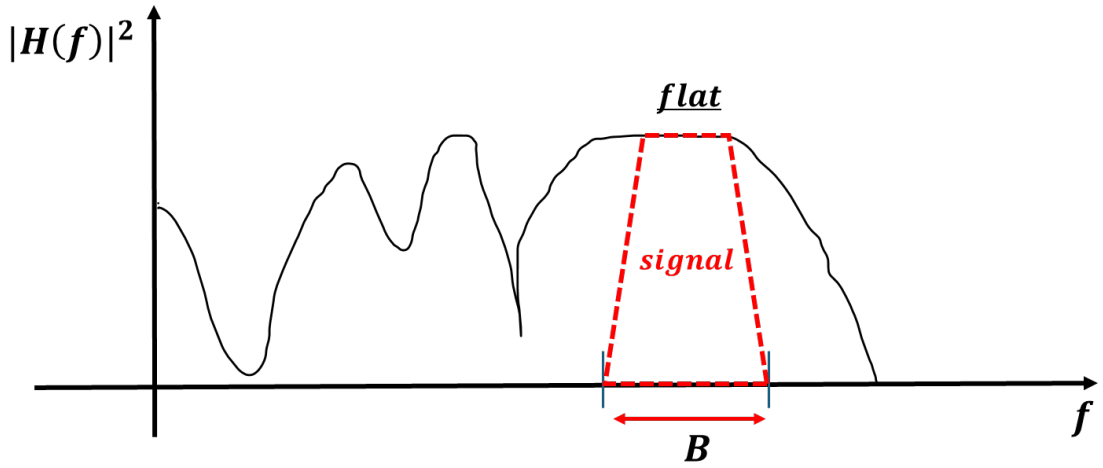

Figure 2.4: Flat Fading.

FREQUENCY-SELECTIVE FADING

This kind of fading happens when the transmitted signal's various frequency components experience various channel conditions. Wideband transmissions, which span a wide frequency range, are usually linked to it. A wideband signal can successfully span a range of wavelengths since wavelength and frequency are inversely related. Consequently, depending on the multipath components and their delays, certain portions of the signal may experience constructive interference while others may encounter destructive interference. The expression "frequency-selective" refers to the distortion that results from the variable attenuation or delay of distinct frequency components. Even in the absence of noise, the received signal in these situations may differ greatly from the transmitted one, necessitating equalization procedures and complicating signal recovery.

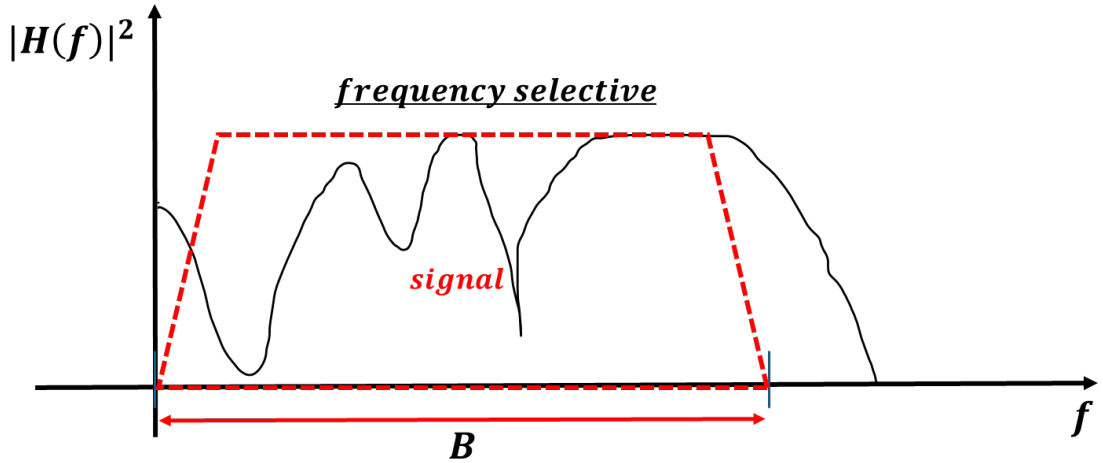

Figure 2.5: Frequency Selective Fading.

VISUAL INTERPRETATION

In the referenced figures, the red shape represents the transmitted signal in the frequency domain, and the black curve represents the current channel response across frequency.
The narrowband signal lies entirely within a portion of the channel that has a relatively constant response, thus experiencing flat fading.
The wideband signal spans a much broader frequency range, where the channel response varies significantly, leading to frequency-selective fading.

2.2.1 Theoretical Analysis and Equations

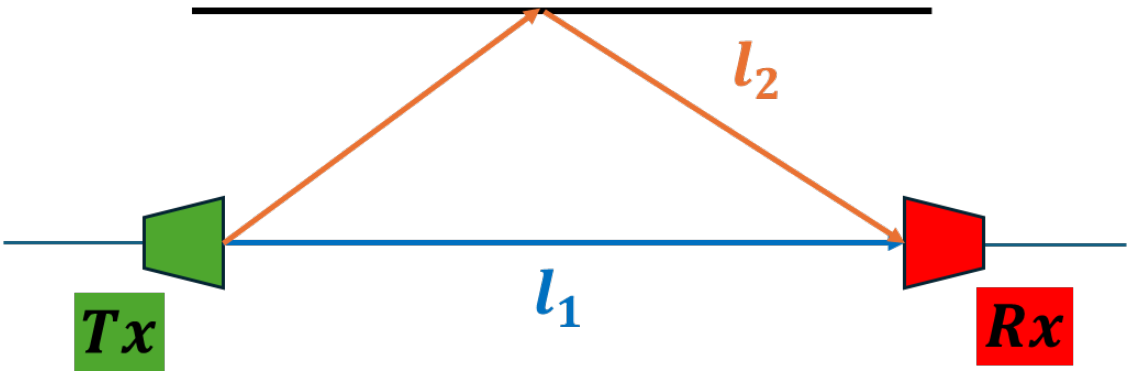

Figure 2.6: Directed path + one reflected path.

TWO-RAY CHANNEL

For a two-ray channel the impulse response is given by:

$$h(t) = \alpha_1 \delta(t - D_1) + \alpha_2 \delta(t - D_2) \tag{2.2}$$

where the delays are:

$$D_1 = \frac{l_1}{c}, D_2 = \frac{l_2}{c} \tag{2.3}$$

Taking the Fourier Transform, we obtain the channel frequency response:

$$H(f) = \mathcal{F}\{h(t)\} = \alpha_1 e^{-j2\pi f D_1} + \alpha_2 e^{-j2\pi f D_2} \tag{2.4}$$

Rewriting the equation:

$$H(f) = \alpha_1 e^{-j2\pi f D_1} \left(1 + \alpha e^{-j2\pi f D_2}\right) \tag{2.5}$$

where:

$$\alpha = \frac{\alpha_2}{\alpha_1} \tag{2.6}$$

and the delay spread is defined as:

$$D = D_2 - D_1 \tag{2.7}$$

The magnitude squared of the frequency response is:

$$|H(f)|^2 = \alpha_1^2 \left|1 + \alpha e^{-j2\pi fD}\right|^2 \tag{2.8}$$

Expanding the exponentials:

$$|H(f)|^2 = \alpha_1^2 \left|1 + \alpha(\cos(2\pi fD) - j\sin(2\pi fD))\right|^2 \tag{2.9}$$

Taking the magnitude:

$$|H(f)|^2 = \alpha_1^2 \left[1 + \alpha^2 \cos^2(2\pi fD) + 2\alpha\cos(2\pi fD) + \alpha^2 \sin^2(2\pi fD)\right] \tag{2.10}$$

Since $\cos^2(x) + \sin^2(x) = 1$, the final expression:

$$|H(f)|^2 = \alpha_1^2 \left[1 + \alpha^2 + 2\alpha\cos(2\pi fD)\right] \tag{2.11}$$

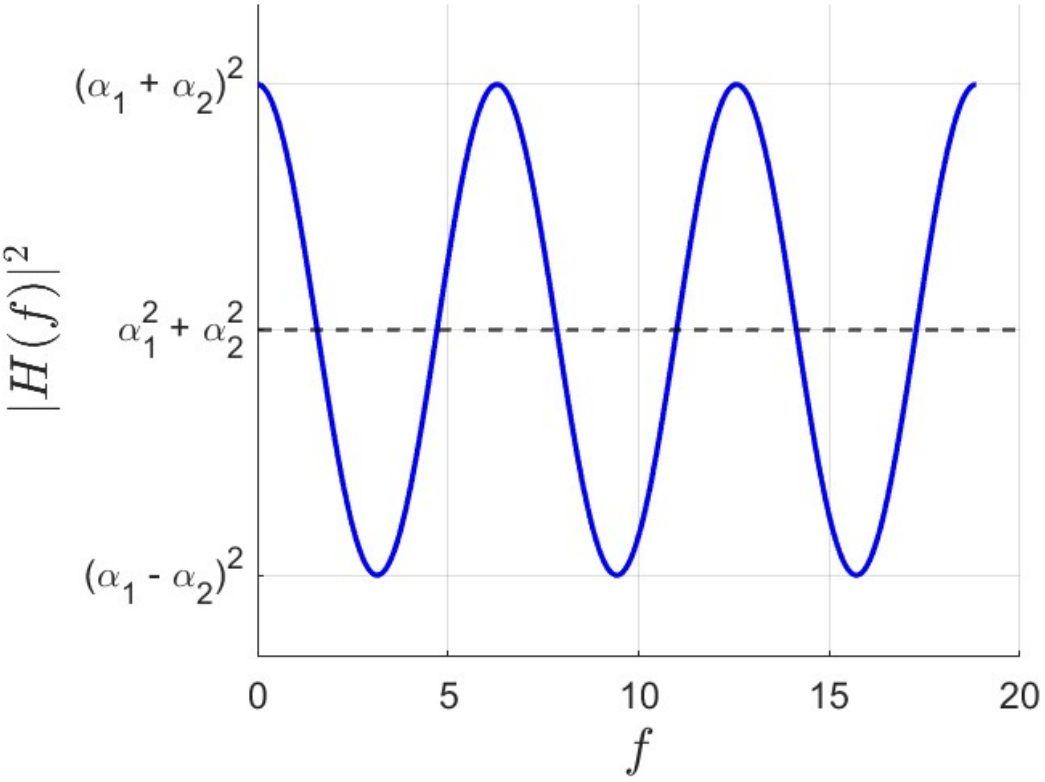

Figure 2.7: Directed path + one reflected path.

so when:

- $cos(2\pi fD) = +1 \rightarrow \alpha_1^2 \left(1 + \alpha^2 + 2\alpha\right) = \alpha_1^2 \left(1 + \alpha\right)^2 = \left(\alpha_1 + \alpha_2\right)^2$
- $cos(2\pi fD) = -1 \rightarrow \alpha_1^2 \left(1 + \alpha^2 - 2\alpha\right) = \left(\alpha_1 - \alpha_2\right)^2$
- $cos(2\pi fD) = 0 \rightarrow \alpha_1^2 \left(1 + \alpha^2\right) = \alpha_1^2 + \alpha_2^2$

The squared magnitude of the frequency response of the system is given by the following equation:

$$|H(f)|^2 = \alpha_1^2 \left[1 + \alpha^2 + 2\alpha \cos(2\pi fD)\right] \tag{2.12}$$

This equation describes the dependence of the system's frequency response on the parameters α_1, α, and the frequency f, with a cosine term involving the delay D.
To simplify the cosine term, a condition is imposed on the frequency, namely:

$$2\pi fD = k2\pi \tag{2.13}$$

where k is an integer. This condition ensures that the argument of the cosine is an integer multiple of 2π, thereby simplifying the cosine term to 1.
Solving for f, the frequency is obtained as:

$$f = k\frac{1}{D} \tag{2.14}$$

The term $\frac{1}{D}$ represents a frequency that is inversely proportional to the delay D. Since frequency and period are related by the equation $f = \frac{1}{T}$, it follows that D must correspond to the period of the oscillation.
Therefore, D represents the time period of the system, and the reciprocal $\frac{1}{D}$ is the fundamental frequency.
In the context of wireless communication, D is related to the coherence time, which indicates the time duration over which the channel can be considered "static". The reciprocal $\frac{1}{D}$ corresponds to the coherence bandwidth, which defines the range of frequencies over which the channel's impulse response is essentially constant.
Thus, the coherence bandwidth B_c is given by:

$$B_c = \frac{1}{D} \tag{2.15}$$

This implies that the period D is the inverse of the coherence bandwidth B_c.
Flat Fading Condition: If the bandwidth B of the transmitted signal is much smaller than the coherence bandwidth B_c, i.e.,

$$B \ll B_c \tag{2.16}$$

then the channel can be considered to have flat fading, meaning the channel response is approximately constant across the signal's bandwidth. In this case, the entire signal experiences the same fading, and the frequency response remains essentially flat.

Frequency Selective Fading Condition: Conversely, if the bandwidth B of the signal is comparable to or greater than the coherence bandwidth B_c, i.e.,

$$B \geq B_c \tag{2.17}$$

then the channel exhibits frequency selective fading, where different frequency components of the signal experience different amounts of fading. This occurs because the channel's response is not uniform across the entire signal bandwidth.
In summary, the coherence bandwidth $B_c = \frac{1}{D}$ plays a key role in determining whether flat fading or frequency selective fading occurs. Flat fading conditions arise when the signal's bandwidth is much smaller than the coherence bandwidth, while frequency selective fading occurs when the signal's bandwidth exceeds or is comparable to the coherence bandwidth.
In multicarrier systems (such as OFDM), the total available bandwidth is divided into many small subbands, each with bandwidth $\Delta = \frac{B}{N}$, where N is the number of subcarriers. To ensure that flat fading occurs in each subband, the following condition must hold:

$$\Delta \ll \frac{1}{D} \tag{2.18}$$

This ensures that each subband is small enough such that the coherence bandwidth B_c is much larger than the bandwidth of each subband, resulting in flat fading within each individual subband. In this way, each subcarrier experiences independent flat fading, and the system can mitigate frequency selective fading by treating each subband as a flat fading channel.
This approach helps combat frequency selective fading and improves the reliability of the system.

2.3 Line of Sight (LoS) - FRIIS equation

The Friis transmission equation describes the power received by an antenna under ideal free-space conditions, given a transmitting antenna located some distance away. It is fundamental in wireless communication for understanding signal propagation. The equation is given by:

$$P_{rx} = P_{tx} \cdot \left(\frac{G_{tx} G_{rx} \lambda^2}{(4\pi d)^2} \right) \tag{2.19}$$

where:

- P_{rx} is the received power (W),
- P_{tx} is the transmitted power (W),
- G_{tx} and G_{rx} are the gains of the transmitting and receiving antennas, respectively,
- λ is the wavelength of the transmitted signal (m),
- d is the distance between the antennas (m),

- $4\pi d$ represents the spherical spreading of the wavefront.

The Friis equation assumes that:

- The antennas are in free space with no obstacles or interference.
- The signal propagates purely via LoS without reflections or diffraction.
- The antennas are properly aligned to maximize gain.

This equation highlights the inverse square law behavior of signal power, meaning that as the distance d increases, the received power P_{rx} decreases proportionally to d^2. This principle is crucial for designing wireless communication links, particularly for satellite, radio, and microwave systems, where LoS conditions are often required for optimal performance.

2.4 Attenuation

The main reason why it is necessary to move to high frequencies is to achieve high bit rates. However, this means having higher attenuation and the need to have large bands.

1. FSPL in Linear Form:

$$FSPL = \left(\frac{4\pi df}{c}\right)^2 \tag{2.20}$$

This formula expresses the path loss as a **power ratio** (not in dB). Path loss increases **quadratically** with both **distance** d and **frequency** f. Higher frequencies and longer distances lead to more attenuation.

2. FSPL in Decibel (dB) Form:

$$FSPL(dB) = 32.4 + 20\log_{10}(d) + 20\log_{10}(f) \tag{2.21}$$

This version is used for practical calculations where d is in **m** and f is in **GHz**. The **32.4 dB constant** comes from converting the units and incorporating the constant $\frac{4\pi}{c}$.

2.5 Shadowing

The presence of obstacles between the Tx and the Rx leads to have grater attenuation.

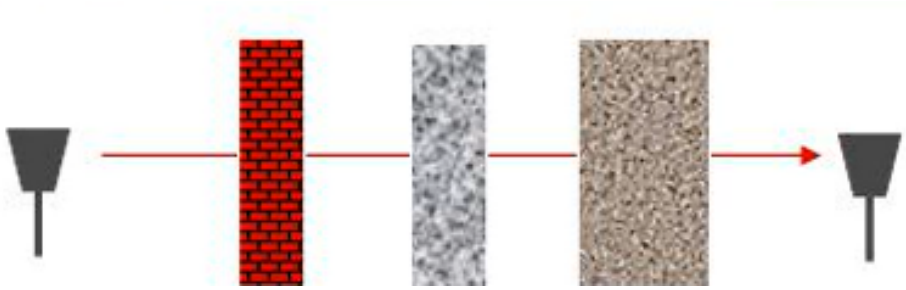

Figure 2.8: Shadowing.

So the following model is used:

$$FSPL(dB) = 32.4 + 10 \cdot n \log_{10}(d) + 20 \log_{10}(f) + A_{SH} \tag{2.22}$$

where typical values for n are

$$2 \leq n \leq 4$$

and A_{SH} is modelled as a gaussian random variable with $\mu = 0, \sigma^2 = 8dB$ and represents the sum of a sequence of different materials with different attenuations.

2.6 Multipath Fading

As already said, in wireless communication systems, the transmitted signal often reaches the receiver through multiple propagation paths due to reflection, scattering, and diffraction. Each of these paths can be characterized by a certain delay and attenuation, leading to what is commonly known as a *multipath channel*. The overall effect of these multiple rays can be modeled as a discrete-time finite impulse response (FIR) filter, where each tap corresponds to a delayed and scaled version of the transmitted signal.

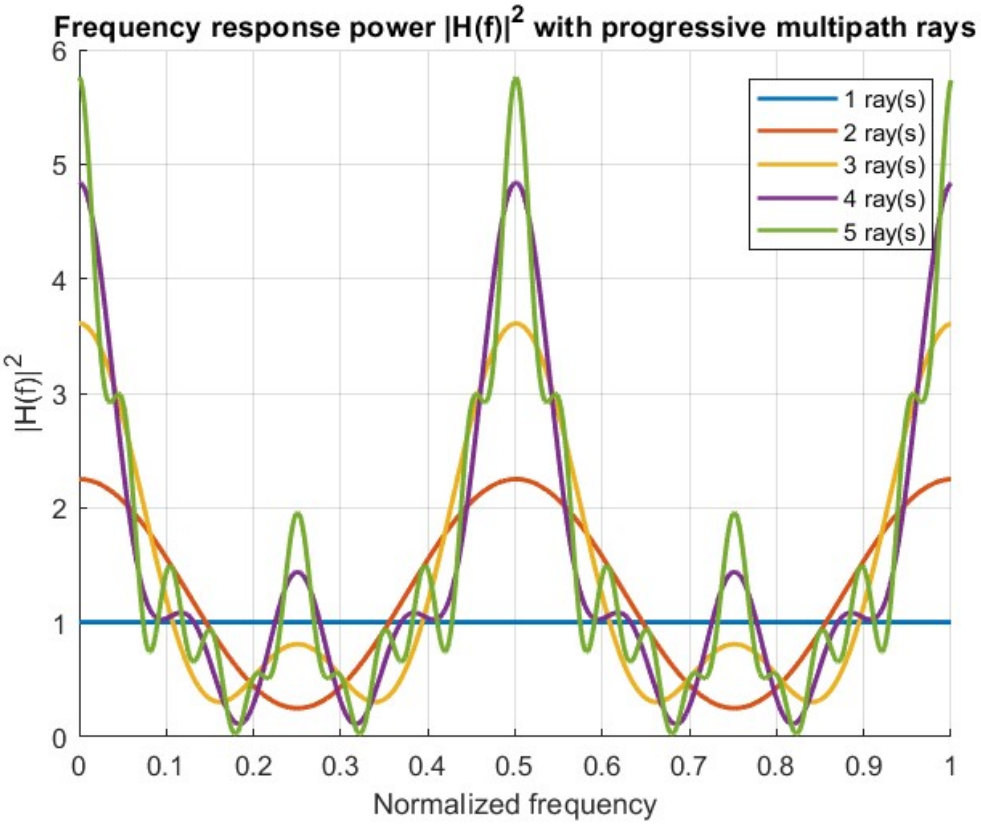

Figure 2.9: Multipath fading with 5 different paths.

The figure shows the squared magnitude of the frequency response, $|H(f)|^2$, of a multipath channel as additional propagation rays are progressively added. The first curve represents the frequency response of a single-ray (line-of-sight) channel, which is flat across all frequencies, indicating a frequency non-selective channel. As more rays are introduced each with its own delay and attenuation the frequency response becomes increasingly irregular and exhibits fading notches. This is due to constructive and destructive interference among the rays, which causes frequency-selective behavior.
The final response, with five rays included, clearly shows how the channel selectively attenuates certain frequencies while amplifying others. This frequency selectivity becomes more pronounced as the delay spread increases, confirming the impact of multipath components on the overall channel behavior. Understanding this frequency response is crucial for the design of robust communication systems, especially in OFDM and wideband systems where inter-symbol interference (ISI) can severely degrade performance.

Chapter 3

Orthogonal Frequency Division Multiplexing (OFDM)

A highly effective modulation method, orthogonal frequency division multiplexing (OFDM) is utilized extensively in contemporary communication systems, such as digital television, broadband internet, and wireless networks. OFDM's primary benefit is its capacity to manage large data rates while reducing the impact of channel impairments like interference and multipath fading.

The way OFDM operates is by splitting the available bandwidth into several closely spaced subcarriers, each of which is modulated with a stream of low-rate data. Because the subcarriers are mutually orthogonal, they can share the same spectrum efficiently without causing interference to each other. High spectral efficiency is made possible by the use of orthogonal subcarriers, which makes OFDM the perfect option for settings where data flow is crucial and bandwidth is at a premium.

Initially, the method was presented as a way to address the issues with conventional frequency-division multiplexing (FDM) systems, which have inter-symbol interference (ISI) in settings with high multipath propagation. OFDM is a viable option for both wired and wireless communication systems because it enables effective implementation through the use of sophisticated signal processing techniques like the Fast Fourier Transform (FFT).

OFDM remains a key component of next-generation technologies, including as 4G LTE, 5G, and Wi-Fi, in light of the rising demand for high-speed internet and the complexity of communication networks. Its capacity to adapt to diverse channel circumstances and efficiently employ available spectrum makes it a vital modulation technique in modern telecommunication.

3.1 OFDM Waveforms

3.1.1 Signal Representation and Frequency-Domain Considerations:

A given signal can be represented as a carrier waveform (a sine wave at a specific frequency) multiplied by a rectangular function that turns the carrier on and off. Since

multiplication in the time domain corresponds to convolution in the frequency domain, this operation has important implications for signal representation.

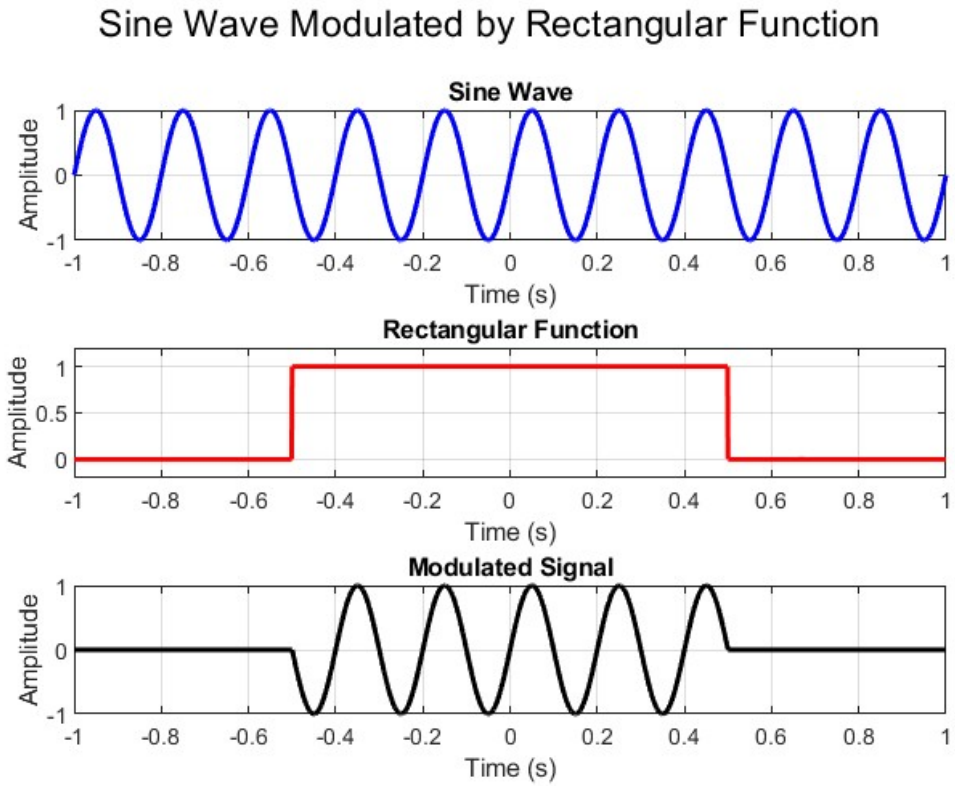

Figure 3.1: Sine wave modulated by rectangular function.

Mathematically, the Fourier transform of a rectangular function is a sinc function:

$$\mathcal{F}\{\text{rect}(t)\} = \text{sinc}(f)$$

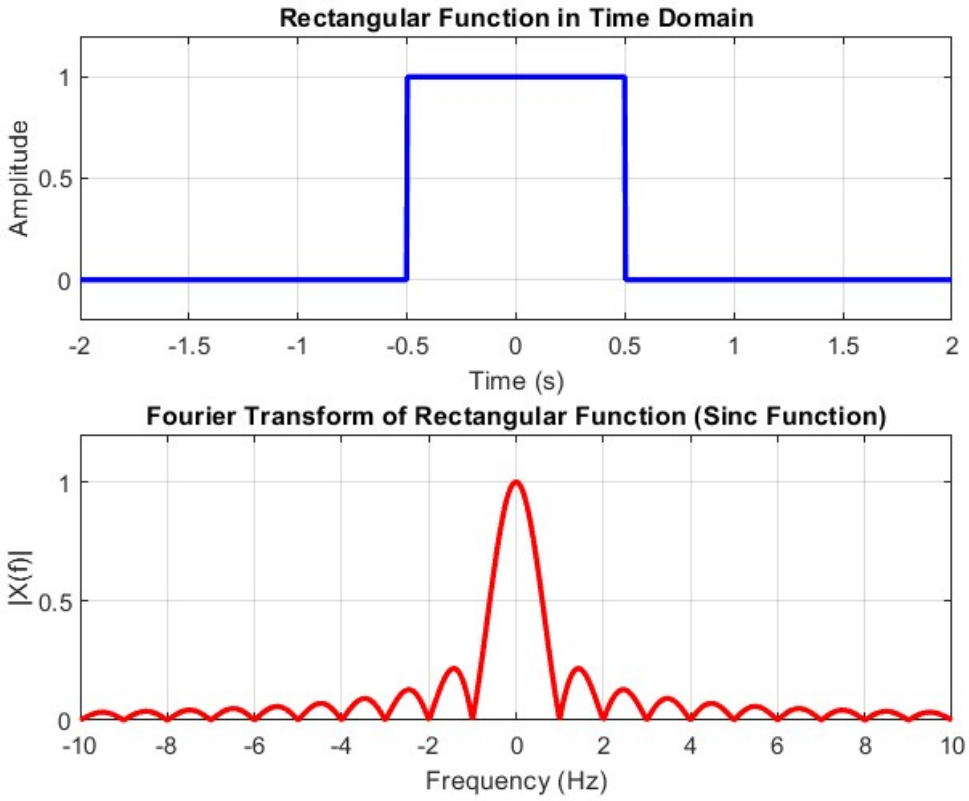

Figure 3.2: Fourier transform of a rectangular function.

3.1.2 Frequency Division Multiplexing (FDM):

FDM enables multiple signals to be transmitted on the same channel at different frequencies. The key principle is to space the main lobes of the sinc functions such that they do not interfere with each other's side lobes. However, due to the presence of side lobes, there is still some level of interference between adjacent carriers.

To maximize spectral efficiency, these carriers are placed as close together as possible, ensuring that all carrier frequencies are exact multiples of each other. This allows for efficient utilization of bandwidth while maintaining orthogonality.

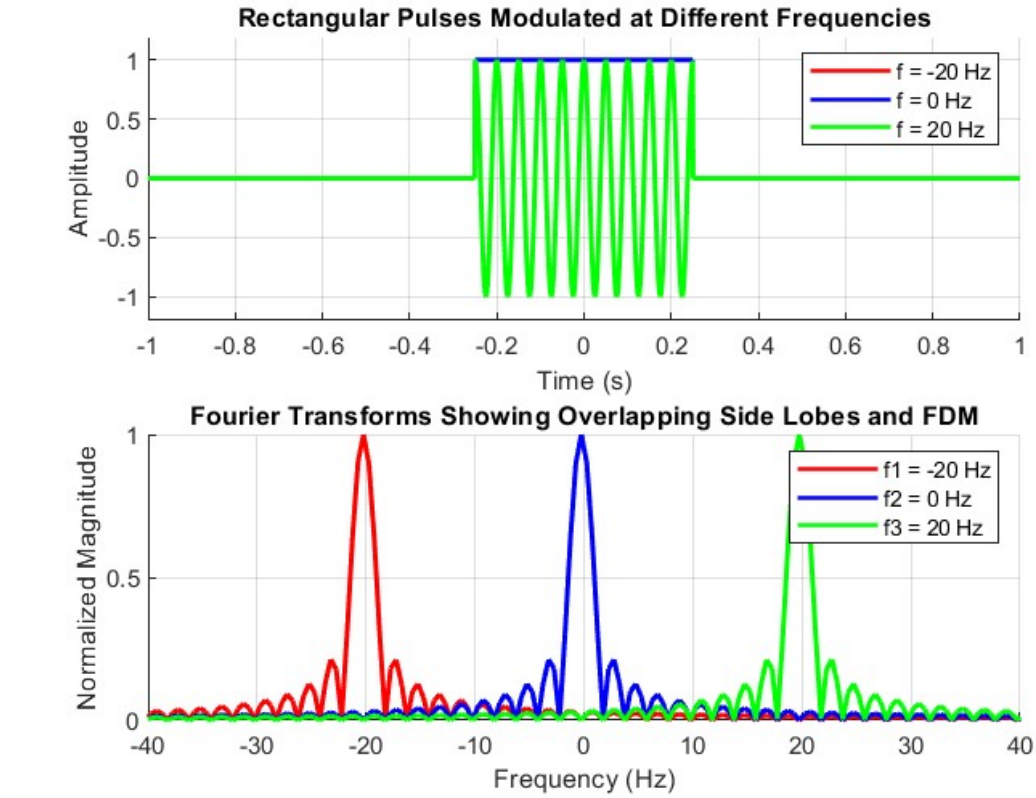

Figure 3.3: FDM.

3.1.3 Orthogonality in the Time Domain:

By considering in the time domain one cycle of a signal $S_1(t)$ and another signal $S_2(t)$ with a frequency that is double that of $S_1(t)$, we observe that $S_2(t)$ completes two cycles in the same period as $S_1(t)$. If these signals are carefully chosen, their product over one period results in zero when integrated.

Mathematically, this can be expressed as:

$$\int_0^T S_1(t)S_2(t)\,dt = 0 \tag{3.1}$$

This property is exploited in digital communication systems, where the matched filter at the receiver performs this integration. Since the multiplication of $S_1(t)$ and $S_2(t)$ results in zero over the integration period, the receiver can separate the signals without interference.

Thus, it is possible to transmit data using both $S_1(t)$ and $S_2(t)$, ensuring that the matched filter for $S_1(t)$ extracts only $S_1(t)$ while experiencing no interference from $S_2(t)$, and vice versa.

3.1.4 Orthogonality in the Frequency Domain:

In the frequency domain, orthogonality means that the sinc-shaped spectra of different subcarriers are perfectly aligned. The peak of each sinc function is positioned exactly at the first zero of its neighboring subcarrier's main lobe, ensuring that the subcarriers do not interfere with one another.

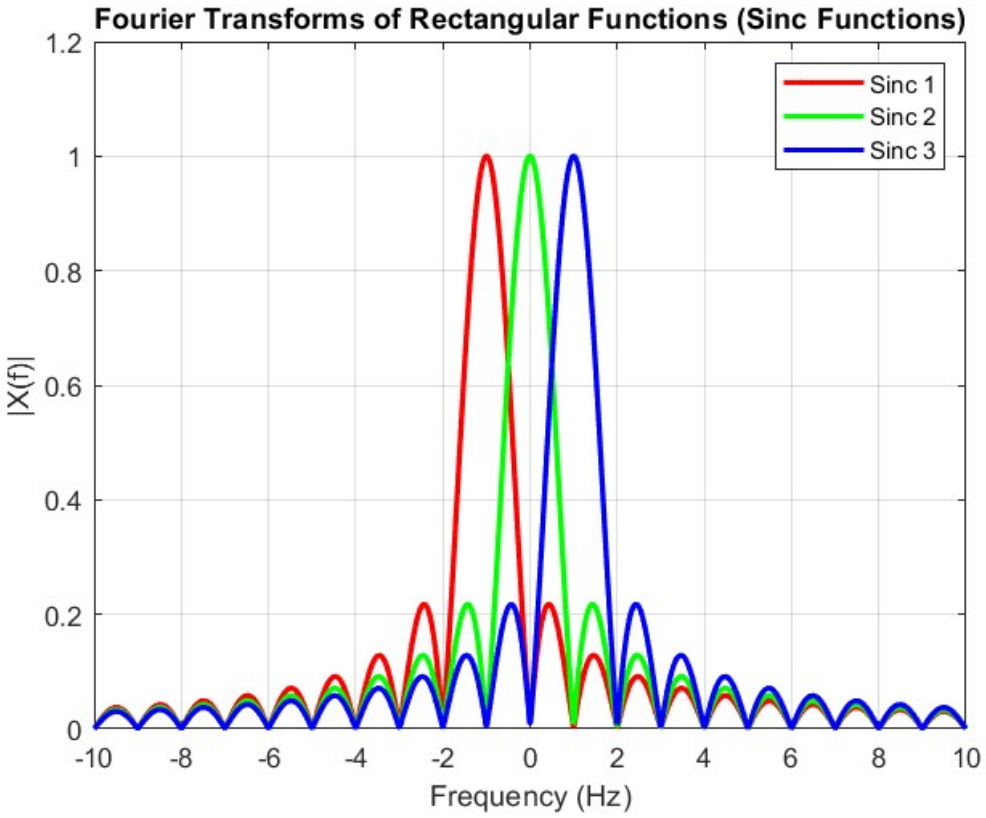

Figure 3.4: Orthogonality in frequency.

Mathematically, this property ensures that:

$$\text{sinc functions satisfy} \quad \text{sinc}(f - f_n) \perp \text{sinc}(f - f_{n+1})$$

Although the signals are transmitted simultaneously across the same channel and overlap in the frequency domain, their careful spacing ensures that they remain recoverable at the receiver. Due to their orthogonality, the matched filter in the receiver can extract each signal independently with zero interference from the others.
Furthermore, to reduce the interference on adjacent bands due to high secondary lobes of rectangular shaping filter, a drastic solution can be applied: the external subcarriers are not used (to turn off external tones dummy siymbols equal to 0 are transmitted over them). In the following plot, the resulting spectrum is shown where on each tone a random 4-QAM constellation is transmitted.

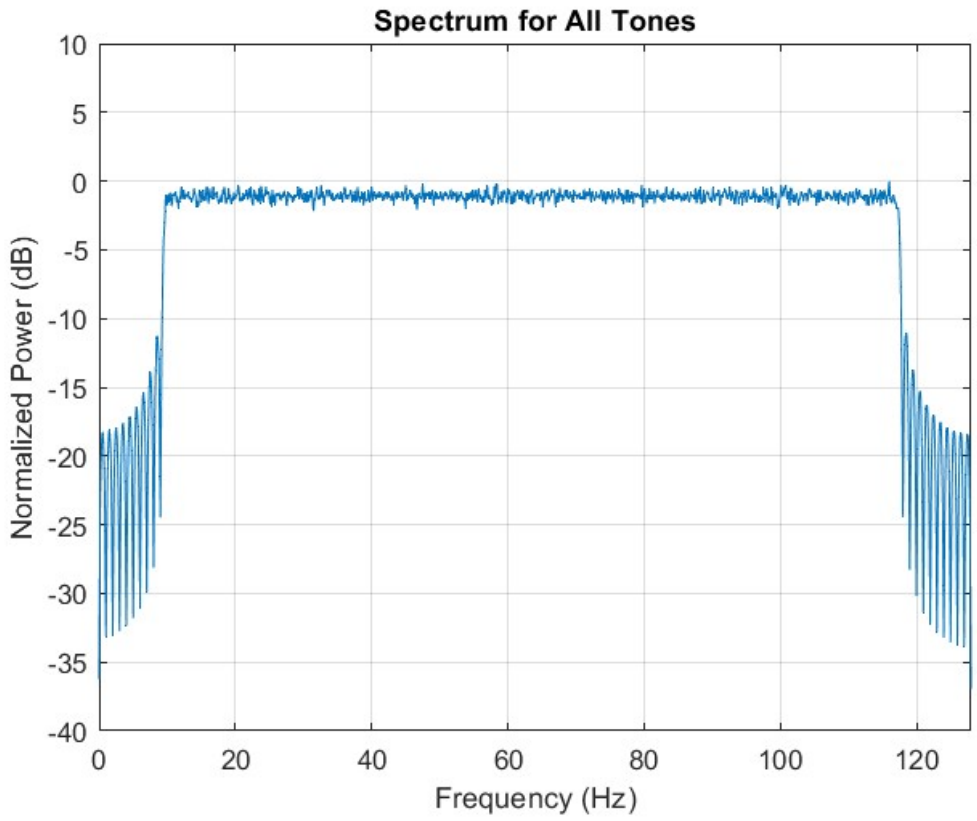

Figure 3.5: OFDM Spectrum (external tones not used).

3.2 OFDM System and DFT-Based Processing

The fundamental processing steps in an OFDM system can be summarized as follows:

1. **Serial-to-parallel conversion**: The input data stream is divided into N parallel data symbols.

2. **Modulation and mapping**: Each symbol is mapped onto a complex constellation (e.g., QAM or PSK).

3. **Inverse Discrete Fourier Transform (IDFT)**: The frequency-domain symbols are converted into a time-domain signal using the IDFT, which is mathematically defined as:
$$x_n = \frac{1}{N} \sum_{k=0}^{N-1} X_k e^{j2\pi kn/N}, \quad n = 0, 1, \ldots, N-1 \tag{3.2}$$

4. **Parallel-to-serial conversion**: The IDFT output is converted back into a serial data stream.

5. **Digital-to-analog conversion (DAC)**: The discrete-time signal is converted into a continuous-time waveform.

6. **Upconversion and transmission**: The baseband signal is modulated to the carrier frequency and transmitted over the communication channel.

7. **Reception and downconversion**: At the receiver, the signal is downconverted to baseband and sampled.

8. **Discrete Fourier Transform (DFT)**: The time-domain samples are transformed back into the frequency domain using the DFT:

$$X_k = \sum_{n=0}^{N-1} x_n e^{-j2\pi kn/N}, \quad k = 0, 1, \ldots, N-1 \tag{3.3}$$

9. **Demapping and decoding**: The received symbols are mapped back to the original data stream.

10. **Parallel-to-serial conversion**: The parallel data is converted back into a serial bitstream for further processing.

In the frequency domain, the IDFT process corresponds to the modulation of multiple orthogonal subcarriers, while the DFT at the receiver demodulates these subcarriers, recovering the transmitted data. The use of a cyclic prefix helps mitigate inter-symbol interference (ISI) caused by multipath propagation, ensuring reliable signal reconstruction.

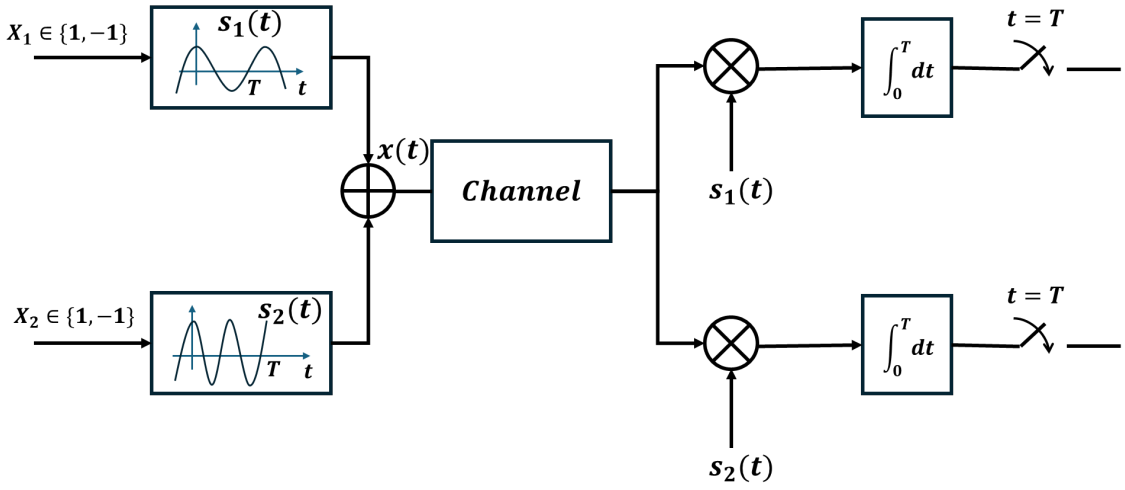

Figure 3.6: Block scheme OFDM and DFT.

$$\int_0^T [X_1 S_1(t) + X_2 S_2(t)]\, S_1(t)\, dt \tag{3.4}$$

$$X_1 \int_0^T S_1(t)^2 \, dt + X_2 \int_0^T S_1(t) S_2(t) \, dt \tag{3.5}$$

Since $S_1(t)$ and $S_2(t)$ are orthogonal, we know that:

$$\int_0^T S_1(t) S_2(t) \, dt = 0 \tag{3.6}$$

Therefore, the second term in the original integral disappears, and we are left with:

$$X_1 \int_0^T S_1(t)^2 \, dt \tag{3.7}$$

Thus, the integral simplifies to:

$$\int_0^T \left[X_1 S_1(t) + X_2 S_2(t) \right] S_1(t) \, dt = X_1 \int_0^T S_1(t)^2 \, dt \tag{3.8}$$

So at the output we can detect the digital data that was in X_1 without having any effect from X_2 and vice versa.
If the concept is extended to more orthogonal signals:

$$x(t) = \sum_{k=0}^{N-1} X_k e^{j \frac{2\pi k}{T} t} \tag{3.9}$$

that corresponds exactly to the Inverse Discrete Fourier Transform (IDFT) equation.
So the frequency is picked very carefully with k integer multiple of $\frac{1}{T}$ to have them orthogonal and to avoid the effect of other channels on each of the interested ones.
At this stage all the analog electronics can be replaced by digital computations of **Inverse Discrete Fourier Transform (IDFT)** and **Discrete Fourier Transform (DFT)**. This computation can be done very fast and efficiently on OFDM chips.

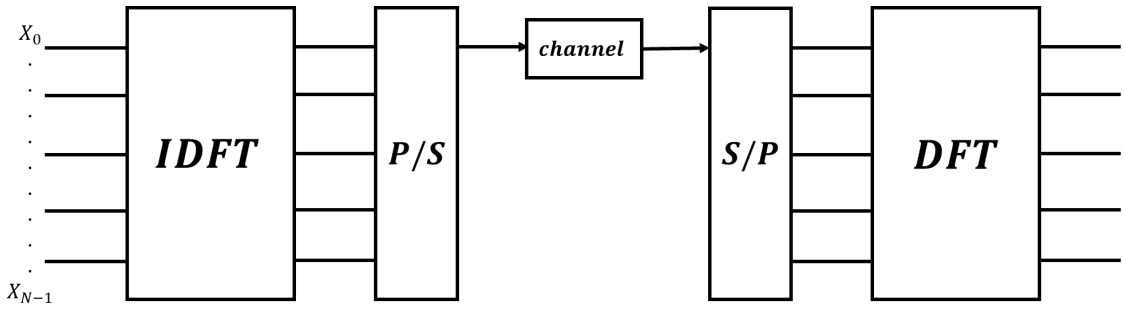

Figure 3.7: Block scheme with IDFT and DFT.

where P/S stands for **parallel to serial converter** and vice versa for S/P, P/S is a digital circuit that takes multiple parallel bits of data (i.e., multiple bits transmitted simultaneously) and converts them into a single serial stream of data (i.e., one bit transmitted at a time).

3.3 Equalization techniques

In Orthogonal Frequency Division Multiplexing (OFDM) systems, equalization techniques are crucial for mitigating channel impairments such as multipath fading and Doppler shifts. These techniques are particularly important in the context of OFDM schemes, where the received signal may suffer from distortions due to the channel. While the specifics of their implementation are beyond the scope of this work, it is necessary to mention these methods to provide a more complete understanding of their importance in enhancing system performance. The reader should recognize that equalization is essential for ensuring reliable communication, especially in challenging channel conditions.

Several equalization methods have been proposed, including the Zero Forcing (ZF) equalizer, the Minimum Mean Square Error (MMSE) equalizer, and the decision-feedback equalizer (DFE). The ZF equalizer attempts to invert the channel response by using the pseudo-inverse of the channel matrix, leading to a solution where the symbol vector is obtained as:

$$\hat{\mathbf{x}} = (\mathbf{H}^H\mathbf{H})^{-1}\mathbf{H}^H\mathbf{y} \tag{3.10}$$

where $\mathbf{H}$ is the channel matrix, $\mathbf{H}^H$ its Hermitian transpose, $\mathbf{y}$ is the received signal, and $\hat{\mathbf{x}}$ represents the estimated transmitted symbols. The MMSE equalizer aims to minimize the mean square error between the transmitted and estimated symbols by incorporating noise statistics into the equalization process:

$$\hat{\mathbf{x}} = (\mathbf{H}^H\mathbf{H} + \sigma^2\mathbf{I})^{-1}\mathbf{H}^H\mathbf{y} \tag{3.11}$$

where σ^2 denotes the noise power and $\mathbf{I}$ is the identity matrix. The DFE, on the other hand, uses past decisions to cancel interference from previous symbols, which is particularly effective in channels with inter-symbol interference. The equalized output of the DFE can be expressed as:

$$\hat{\mathbf{x}}_n = \mathbf{d}_n - \sum_{k=1}^{n-1} \mathbf{H}_{n,k}\hat{\mathbf{x}}_k \tag{3.12}$$

where $\mathbf{d}_n$ is the received signal and $\mathbf{H}_{n,k}$ represents the interference terms. Each of these techniques aims to improve the reliability of the received signal by reducing the impact of channel distortions.

3.4 OFDM subcarriers

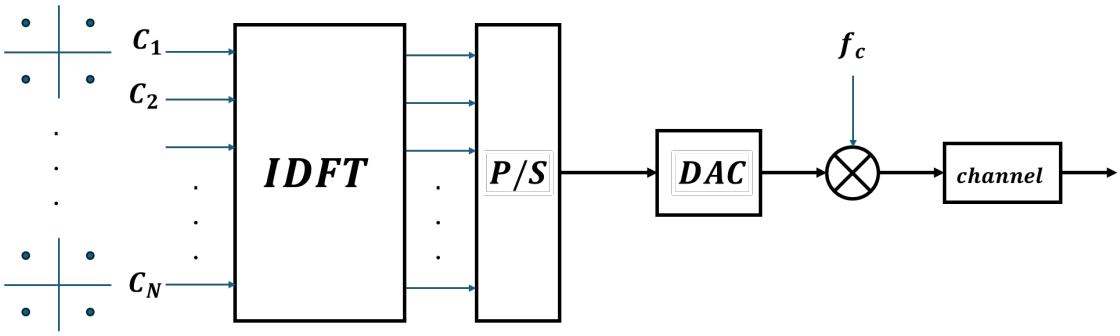

Figure 3.8: OFDM system.

In the transmission of an OFDM system, the following steps occur:

1. Complex numbers $C_1, C_2, \ldots, C_N$ are taken as input. These numbers come from a constellation that represents data.

2. These complex numbers are converted through the **Inverse Discrete Fourier Transform (IDFT)**, producing a vector of length N.

3. This vector is converted from parallel to serial.

4. The serial data is then passed through a **Digital-to-Analog Converter (DAC)** to generate a waveform.

5. Finally, this waveform is upconverted to the carrier frequency and transmitted over the channel.

For better understanding, the following example can be observed:

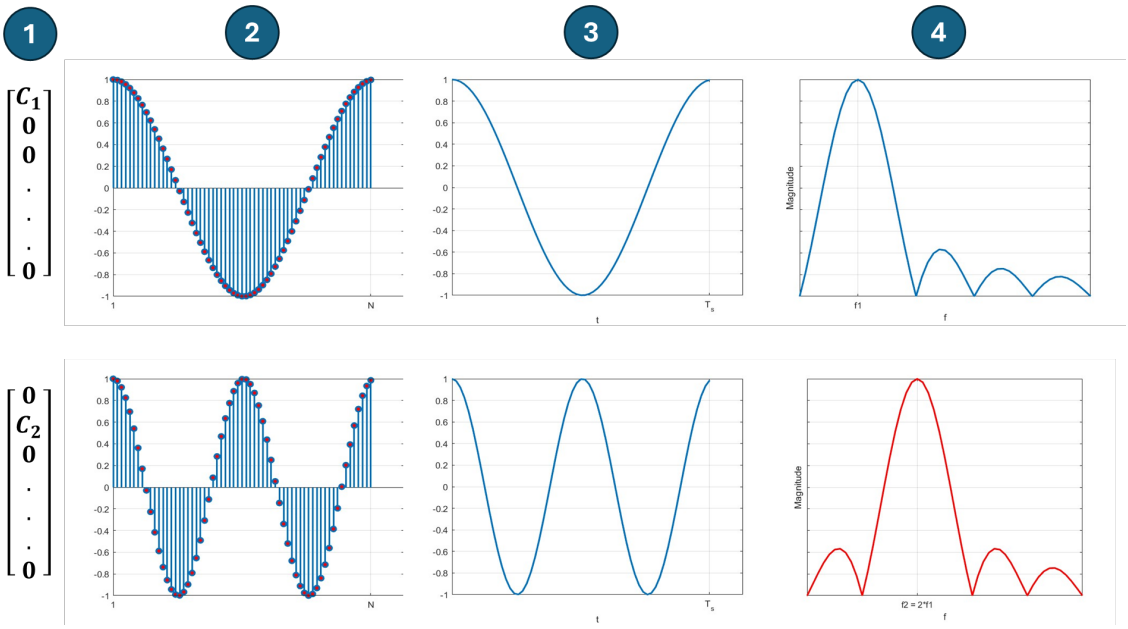

Figure 3.9: Example.

Where by looking at the first row of plots:

1. The input vector is considered.

2. The sinusoidal waveform at the fundamental frequency is obtained after the IDFT, spanning one cycle over the length of the vector. A cosine waveform is shown, as the phase is assumed to be zero.

3. The continuous-time waveform exists only within the interval $0 \leq t \leq T_s$, where T_s represents the symbol time. This function, expressed in the time domain, is given by:

$$\left[e^{j2\pi f_1 t} + e^{j2\pi f_1 t}\right] \cdot \text{rect}\left(\frac{t - T_s/2}{T_s}\right) \tag{3.13}$$

which corresponds to the multiplication of a cosine waveform, represented in its complex exponential form, and a rectangular function. The rectangular function is defined as:

$$\text{rect}\left(\frac{t - T_s/2}{T_s}\right) = \begin{cases} 0, & t < 0 \\ 1, & 0 \leq t \leq T_s \\ 0, & t > T_s \end{cases} \tag{3.14}$$

The presence of this rectangular function results in sinc functions in the frequency domain. This occurs because, in the frequency domain, the multiplication in the time domain translates into a convolution operation. Given that the Fourier transform of a rectangular function is a sinc function:

$$\mathcal{F}\{\text{rect}(t)\} = \text{sinc}(f), \tag{3.15}$$

and the Fourier transform of an exponential function corresponds to a delta function:

$$\mathcal{F}\left\{e^{j2\pi f_0 t}\right\} = \delta(f - f_0), \tag{3.16}$$

convolving the delta function with the sinc function results in sinc functions centered at the locations of the delta function.

4. A sinc function appears at the positive frequency corresponding to the frequency of the complex exponential.

All the above considerations also apply to the second row of plots. However, in this case, the fundamental frequency is doubled. Specifically, after the IDFT, two cycles can now be observed within the period N. When converted into continuous time, this results in a cosine waveform at frequency $f_2 = 2f_1$.

3.4.1 Subcarrier frequencies

All subcarrier frequencies are an integer multiple of Δ:

$$f_0 = i_0 \cdot \Delta \tag{3.17}$$

$$f_i = f_0 + i \cdot \Delta = (i_0 + i) \cdot \Delta, \quad i_0 \in \mathbb{Z}^+ \tag{3.18}$$

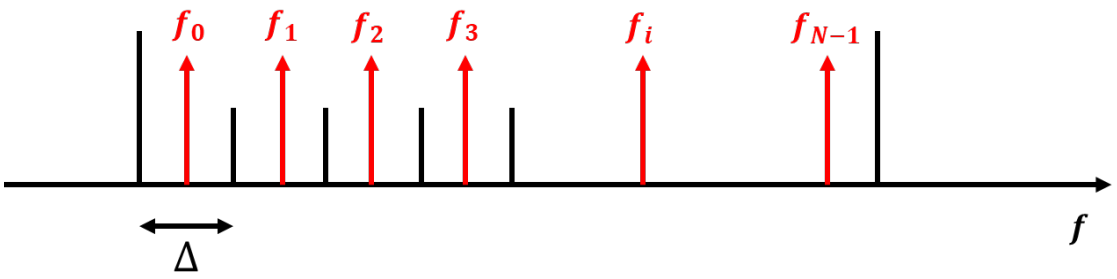

Figure 3.10: Subcarrier frequencies.

This procedure allows to have a big advantage at the Rx side. Since all the frequencies are multiple of Δ, the main point is to estimate Δ and to do this **pilot symbols** are used (they do not carry data).

3.4.2 Symbol rate

On each sub-band it is possible to transmit a PSK/QAM with **symbol rate**

$$R_s = \Delta \tag{3.19}$$

Typically, for single carrier

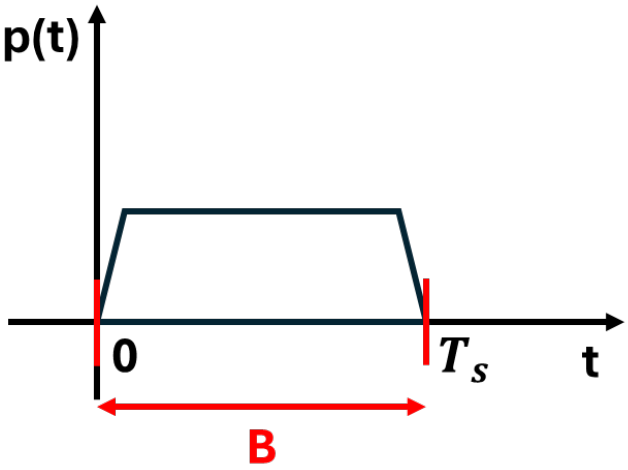

Figure 3.11: Typical pulse shaping.

$$B = R_s \cdot (1 + \alpha), \quad 0 \leq \alpha \leq 1 \tag{3.20}$$

$$R_s = \frac{B}{1 + \alpha} < B \tag{3.21}$$

instead the OFDM solution uses a rectangular shaping filter so

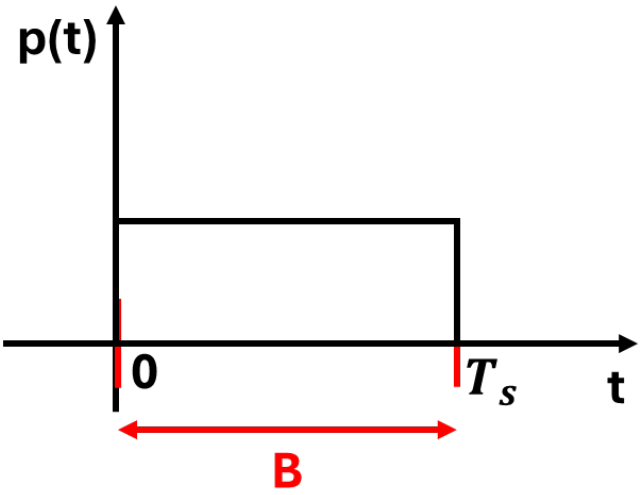

Figure 3.12: Rectangular pulse shaping.

$$R_s = B \tag{3.22}$$

3.5 Inter Symbol Interference for realistic channels (ISI)

Inter Symbol Interference occurs when symbols in a digital signal overlap, causing distortion and errors in data transmission; in the following sections, its nature will be explored in more detail.

3.5.1 Single path channel

Figure 3.13: Single path scheme.

$$h(t) = h_1 \cdot \delta(t - D_1) \tag{3.23}$$

where

$$D_1 = \frac{l_1}{c}, \quad c = 299792458 \text{ m/s (speed of light)} \tag{3.24}$$

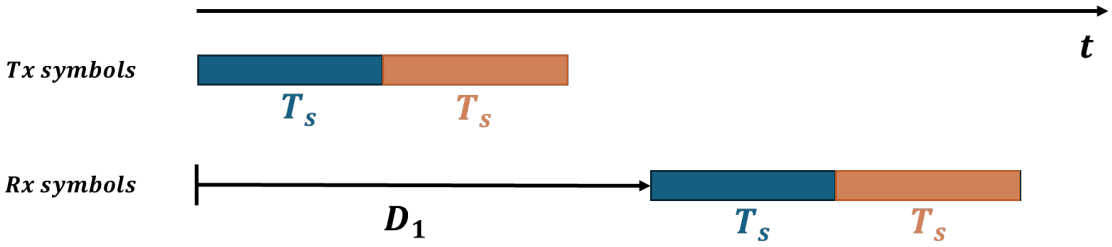

Figure 3.14: Single path channel.

In this scenario everything works, ISI and Inter Carrier Interference (ICI) don't affect the channel. What is received inside T_s does not depend on previous symbols.

3.5.2 Two-ray channel

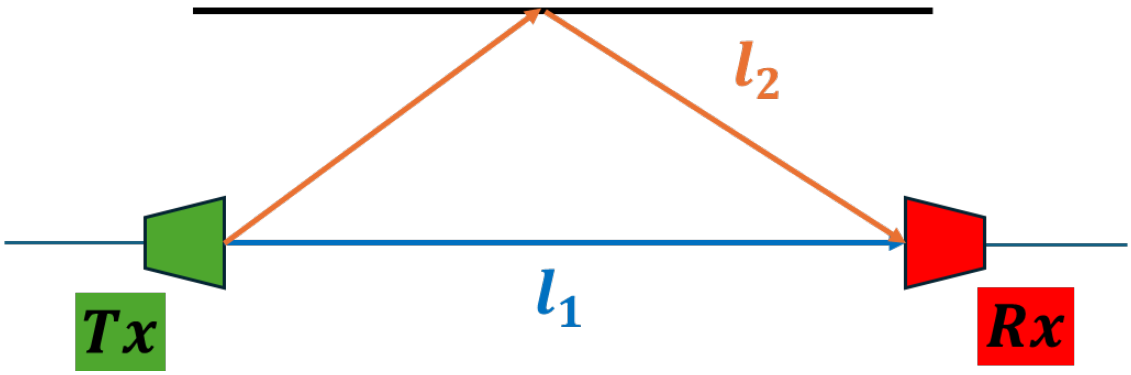

Figure 3.15: Two-ray scheme

$$h(t) = h_1 \cdot \delta(t - D_1) + h_2 \cdot \delta(t - D_2) \tag{3.25}$$

$$D_1 = \frac{l_1}{c} \quad D_2 = \frac{l_2}{c} \tag{3.26}$$

$$D = D_2 - D_1 \quad \text{(Delay spread)} \tag{3.27}$$

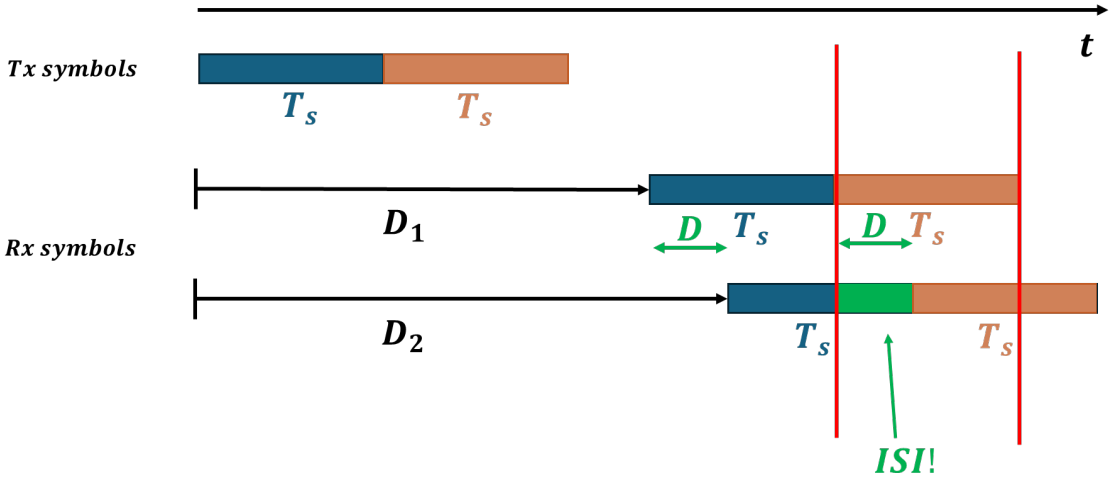

Figure 3.16: Two-ray channel.

If $D \ll T_s$, then

$$\frac{1}{D} \gg \frac{1}{T_s} \tag{3.28}$$

Since $R_s = \frac{1}{T_s}$ and $R_s = \Delta$, when OFDM is used:

$$\Delta \ll \frac{1}{D} \tag{3.29}$$

so in this condition ISI is limited, but the final objective is to have no ISI.

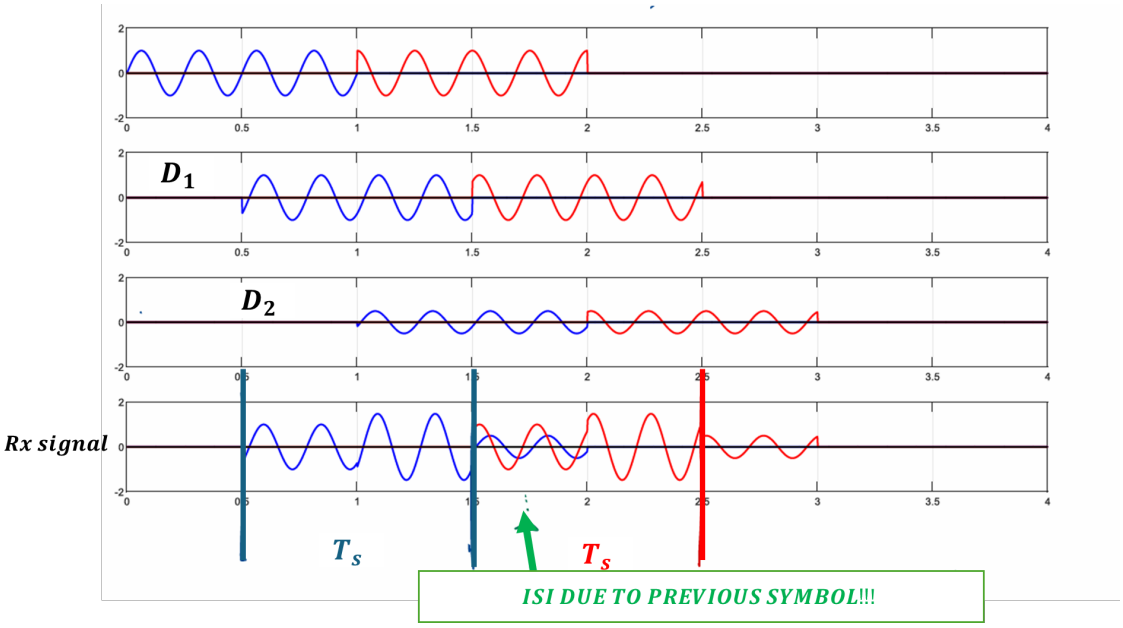

Figure 3.17: ISI.

3.5.3 Guard time solution for ZERO ISI

A possible solution to cancel ISI is to separate the Tx symbols. This can be done by introducing a **guard time** period T_{CP} (Cyclic Prefix).

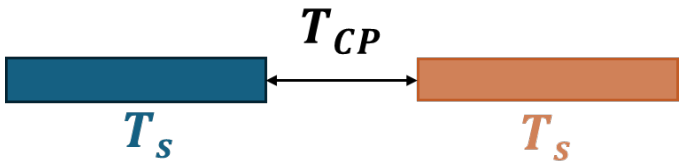

Figure 3.18: Guard time.

where

$$T_{CP} \geq D \tag{3.30}$$

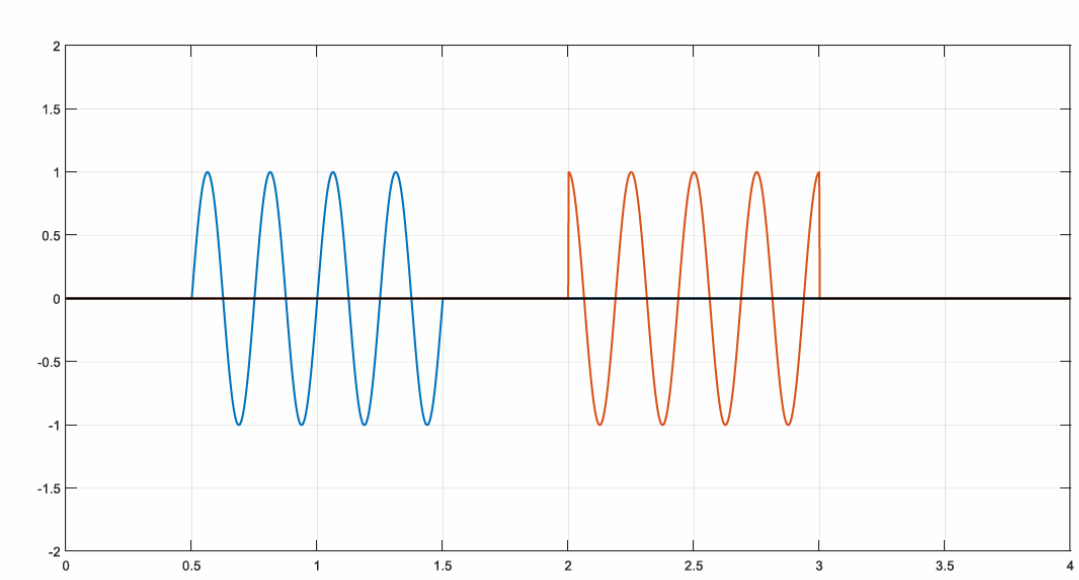

Figure 3.19: Tx symbols with guard time.

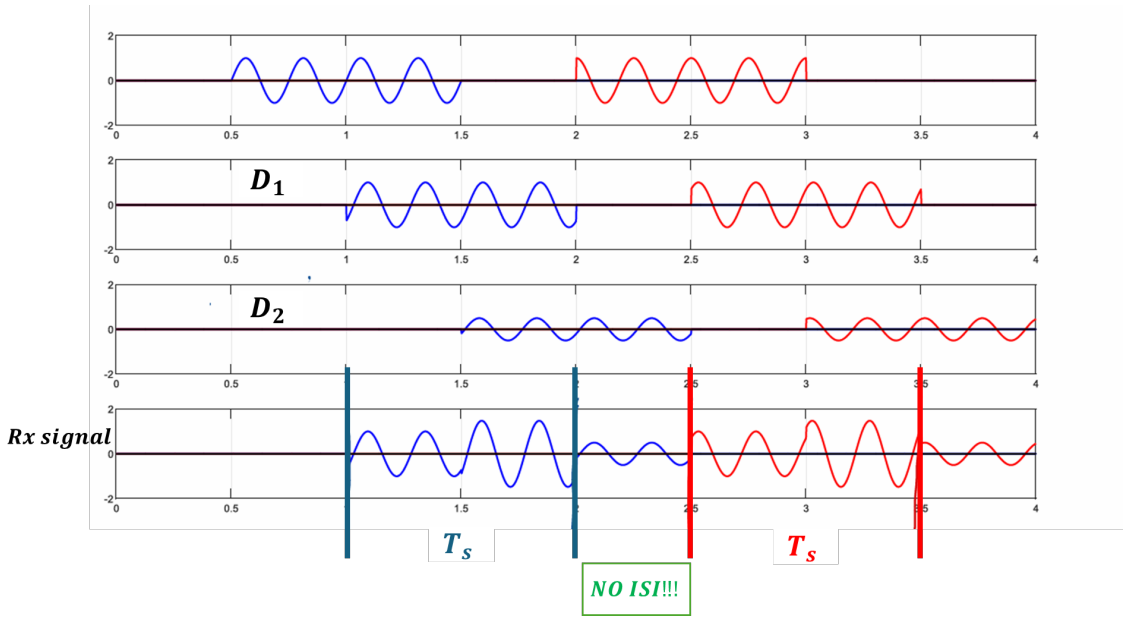

Figure 3.20: NO ISI.

In this way ISI is not present and what is received in a symbol time slot (T_s) does not depend on the previous symbols. The only price to pay is related to the bit rate. In particular the bit rate now is reduced:

$$T_s' = T_s + T_{CP} \tag{3.31}$$

$$R'_s = \frac{1}{T'_s} = \frac{1}{T_s + T_{CP}} \cdot \frac{T_s}{T_s} = R_s \cdot \frac{T_s}{T_s + T_{CP}} \tag{3.32}$$

$$R'_s < R_s \tag{3.33}$$

Link between T_{CP} and L_{MAX}

An important aspect to analyze is the maximum difference (L_{MAX}) between the longest and the shortest path that the guard time is able to absorbe.
In a two-ray channel scenario as before:

$$D_1 = \frac{l_1}{c} \quad D_2 = \frac{l_2}{c} \tag{3.34}$$

$$D = D_2 - D_1 = \frac{l_2 - l_1}{c} = \frac{L}{c} \tag{3.35}$$

$$D \cdot c = L, \quad D < T_{CP} \tag{3.36}$$

3.6 Intercarrier Interference (ICI)

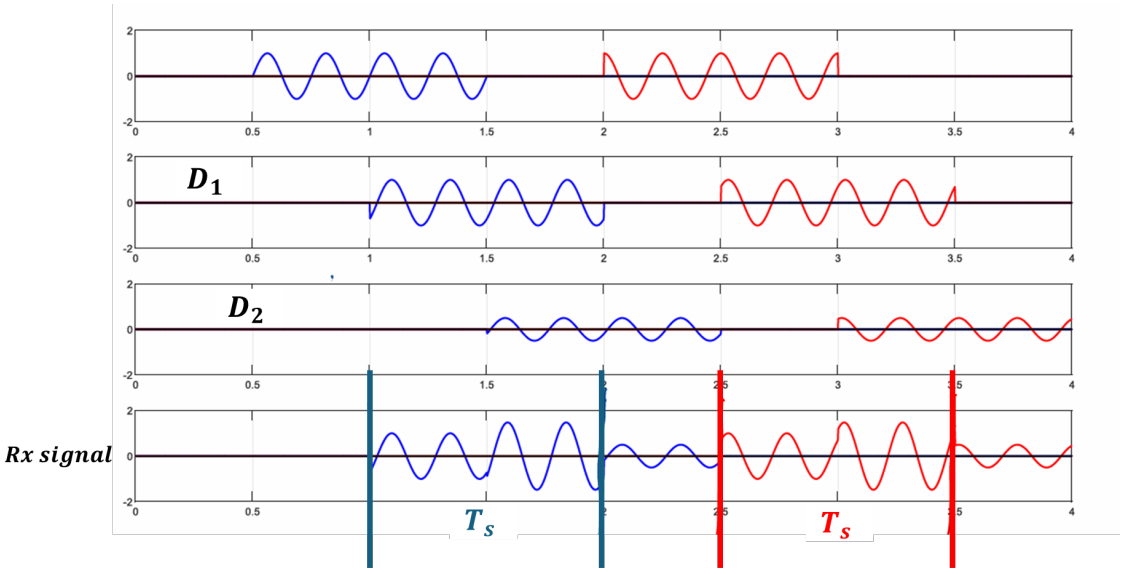

Figure 3.21: ICI.

Unfortunately, what is received inside T_s is not a pure sinusoidal signal at frequency f_i. The OFDM subcarriers are no longer orthogonal, which leads to the experience of Inter-Carrier Interference (ICI).

$$\int_0^{T_s} \cos(2\pi f_i t) \cdot \cos(2\pi f_j t)\, dt = 0 \tag{3.37}$$

only if the signal received inside T_s is a pure sinusoidal signal.

If a sinusoidal signal enters a **Linear Time Invariant (LTI)** system, the corresponding output is also a sinusoidal signal.

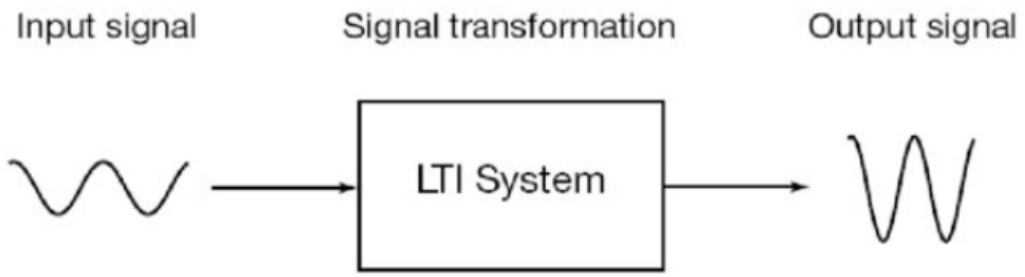

Figure 3.22: LTI system.

In OFDM the input signal is a truncated sinusoidal signal

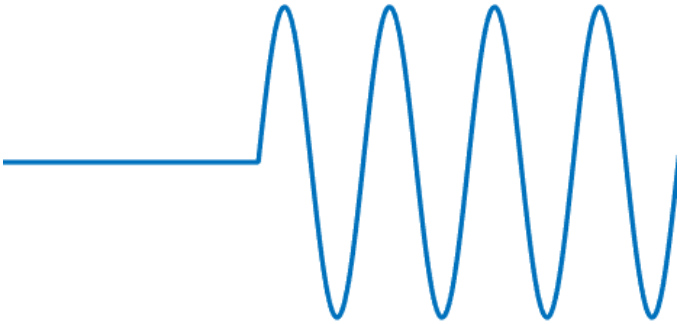

Figure 3.23: Truncated sinusoidal signal.

and the main problem is verified when the impulse response $h(t)$ has a given length.

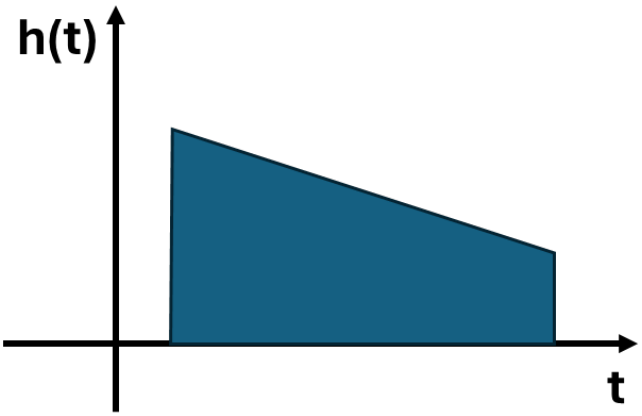

Figure 3.24: Impulse response.

The following graph illustrates the various steps of convolution in the time domain between the input signal and the system's impulse response.

$$y(t) = \int_{-\infty}^{\infty} x(\tau) \cdot h(t-\tau)\, d\tau \tag{3.38}$$

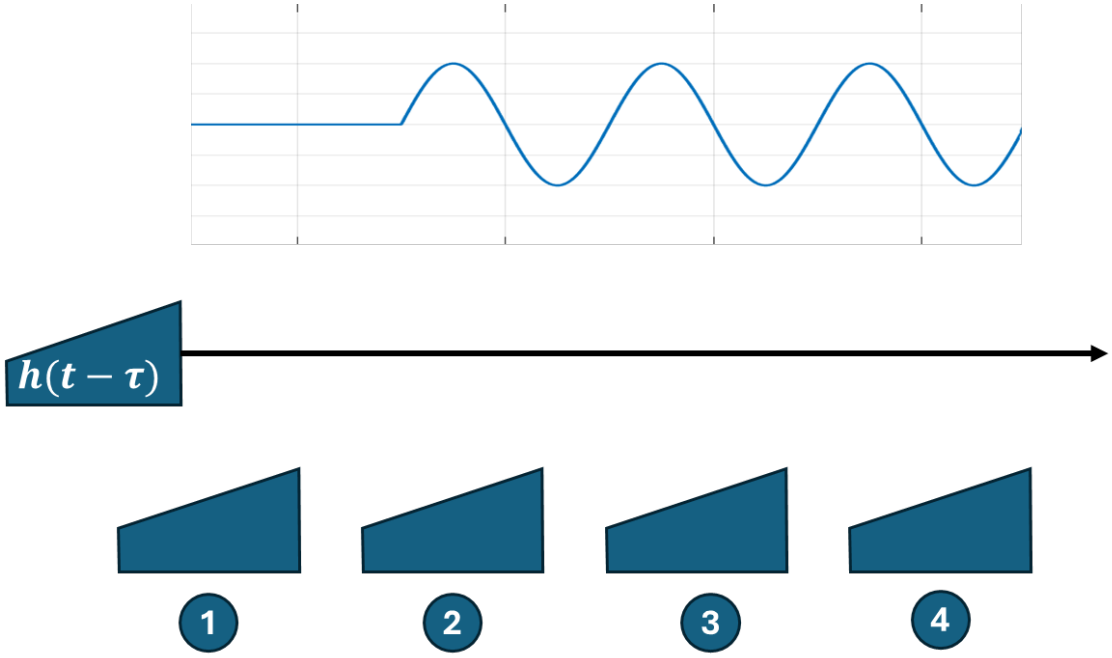

Figure 3.25: Convolution steps in time domain.

1. $h(t-\tau)$ is compared with 0 so the output is 0

2. $h(t-\tau)$ is partially overlapped to the sinusoidal signal so the output is a sinusoidal signal too

3. $h(t-\tau)$ is completely overlapped to the sinusoidal signal so the output is the same sinusoidal signal but different from 2.

4. same as 3.

3.7 Cyclic prefix in OFDM

The cyclic prefix concept involves transmitting a continuous sinusoidal signal during the guard time, rather than leaving it empty. More specifically, the end of the symbol is transmitted during the guard time. The output within the symbol period is obtained by comparing $h(t-\tau)$ with the same continuous sinusoidal signal. This ensures that all subcarriers remain orthogonal, preventing any inter-carrier interference (ICI).

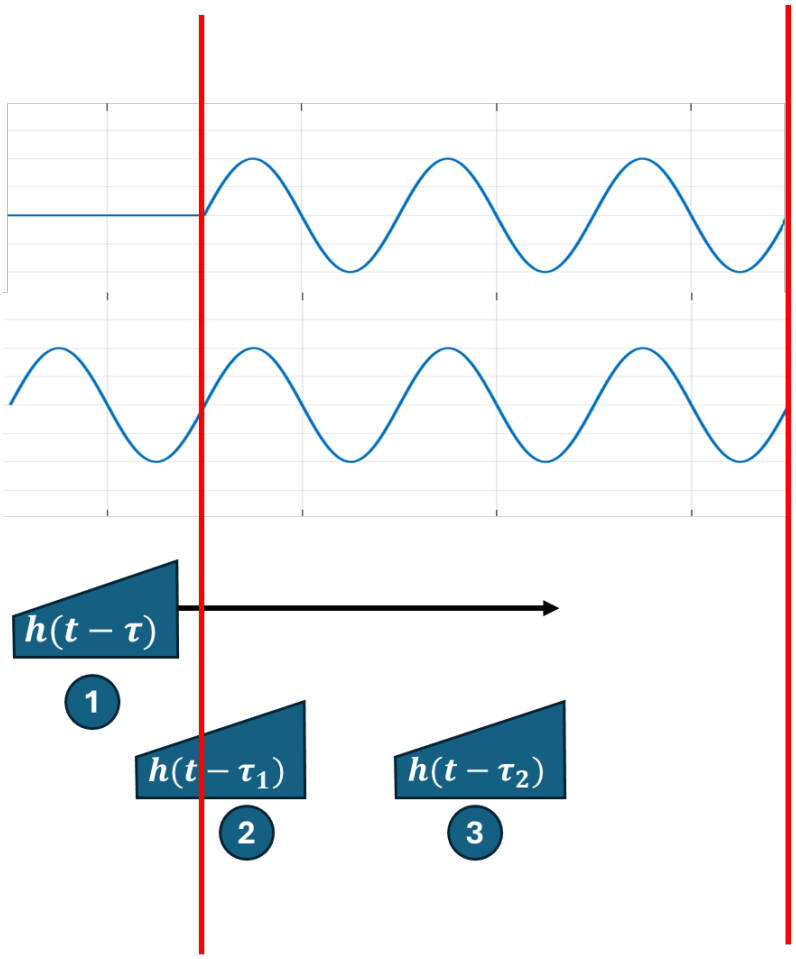

Figure 3.26: Convolution steps in time domain with cyclic prefix.

It is ensured that a continuous sinusoidal signal is obtained because all subcarriers are integer multiples of Δ, and the symbol rate $R_s = \Delta$. As a result, the symbol time contains an integer number of periods. When the tail of the symbol is copied into the guard time, the phase remains the same, which guarantees the creation of a continuous sinusoidal signal. This holds true for all subcarriers and their sum (the entire OFDM signal).

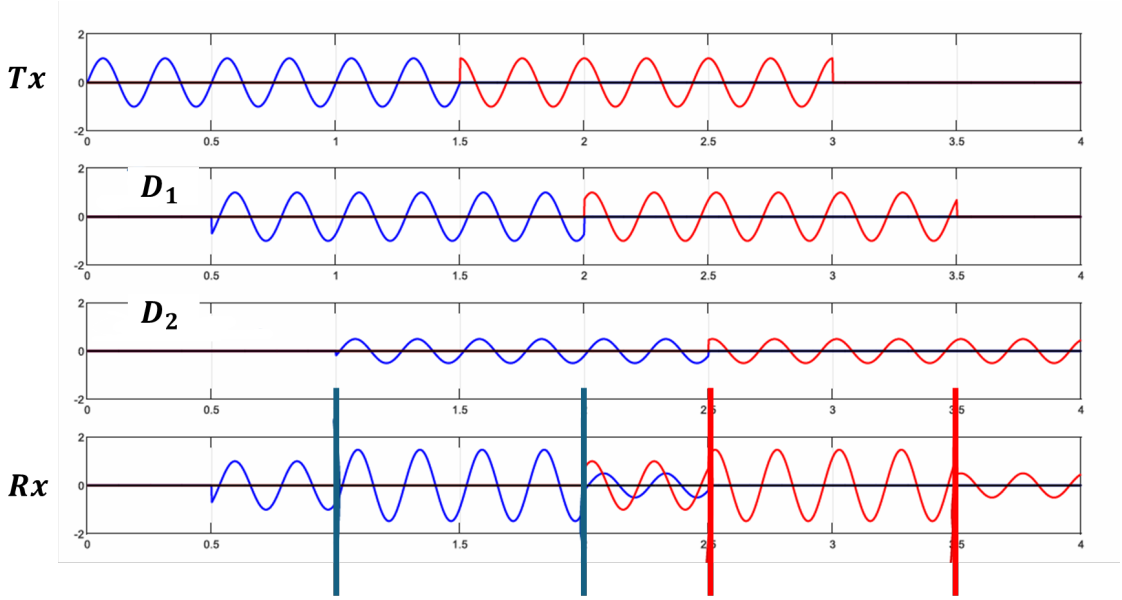

Figure 3.27: No ISI, No ICI.

CP-OFDM solution

In OFDM, the entire tail of the OFDM signal is replicated within the guard time, but this comes at the cost of increased power consumption. An additional portion of the OFDM signal is transmitted, resulting in power waste.

3.8 Considerations for High-Frequency Operation in OFDM

Considering the observations made so far, when working at high frequencies, we encounter the following effects:

- **High attenuation:** As the frequency increases, attenuation also increases significantly. This is especially evident in high-frequency bands.
- **Smaller cells:** Due to high attenuation, the coverage area per cell decreases, requiring the deployment of smaller cells (small cells) to ensure coverage and maintain a good signal quality. Small cells are low-power base stations that cover a much smaller area than traditional macro cells. They are deployed in high density to compensate for the higher attenuation at high frequencies, ensuring consistent coverage and maintaining good signal quality.

- **Lower delay spread:** With higher frequencies, the delay spread (the time difference between the earliest and latest arriving multipath signals) decreases. This means that the signal will experience less dispersion over time.
- **Larger Δ:** The subcarrier spacing (Δ) can be larger because the channel's coherence time and bandwidth are reduced due to the higher frequencies. This allows the system to handle higher data rates with smaller time intervals.
- **Smaller T_s (symbol duration):** The symbol duration (T_s) is smaller due to higher frequencies. With OFDM, this helps increase the data rate and allows for faster symbol transmission.
- **Smaller T_{CP} (cyclic prefix):** The cyclic prefix (T_{CP}), which helps prevent inter-symbol interference (ISI) in OFDM, also becomes smaller with higher frequencies. This is because the delay spread is reduced, meaning less guard time is needed.
- **Smaller L_{max}:** The maximum path length (L_{max}) is reduced with smaller cells, allowing for better control over the propagation environment, but also requiring denser cell deployment.

These effects make high-frequency operation suitable for high-throughput applications like 5G, but they also require careful system design, including the use of small cells, reduced cyclic prefixes, and larger subcarrier spacing to maintain system performance.
The increased subcarrier spacing in 5G, particularly at higher frequencies, is primarily driven by the need to counteract the **Doppler effect**, which poses a significant challenge in mobile communication. As user mobility introduces frequency shifts, these variations lead to ICI in OFDM transmissions, degrading signal quality.
This issue becomes particularly severe at higher carrier frequencies, where the Doppler shift is more pronounced due to its direct proportionality to frequency. Given that the shift is defined by

$$f_D = \frac{v}{c} \cdot f_c \tag{3.39}$$

it increases with both velocity and carrier frequency. Consequently, at higher frequencies, even moderate mobility can lead to significant frequency deviations, disrupting the orthogonality of closely spaced subcarriers.
To mitigate this effect, 5G employs a **scalable subcarrier spacing** approach, increasing the spacing between subcarriers as the operating frequency rises. This adjustment reduces symbol duration and enhances robustness against Doppler-induced interference.
For example, while LTE utilizes a fixed 15 kHz subcarrier spacing, 5G can adopt 30 kHz, 60 kHz, 120 kHz or even 240 kHz, particularly in higher-frequency deployments. This strategy is essential for maintaining reliable communications in high-mobility environments such as vehicular networks and aerial applications, where Doppler shifts are more significant.
To better understand, let's assume a speed $v = 100\,\text{km/h} \approx 27.8\,\text{m/s}$. This allows us to perform some computations and observations based on the table of subcarrier spacing in 4G and 5G technologies.

Mobile network technology	f_c **[GHz]**	f_D **[KHz]**	**% of subcarrier spacing**
4G	2	0.19	1.2% of 15KHz
5G	6	0.5	3.3% of 15KHz
	28	2.6	17.3% of 15KHz or 1% of 240KHz

Table 3.1: Subcarrier spacing in 4G and 5G example.

As the subcarrier spacing increases — particularly in some 5G numerologies — the relative impact of Doppler shift decreases. This has important implications for system performance:

- **4G (2 GHz):** The Doppler shift is very small compared to the 15 kHz subcarrier spacing, with a relative value of about 1.2%. While this is low, Doppler-induced interference can still occur at higher speeds.
- **5G (6 GHz):** Increasing the carrier frequency to 6 GHz increases the Doppler shift to about 0.5 kHz, which is 3.3% of the 15 kHz subcarrier spacing. This means Doppler effects are more noticeable than in 4G, but the use of different numerologies in 5G can help mitigate the impact.
- **5G (28 GHz):** At this much higher frequency, the Doppler shift reaches about 2.6 kHz. If using 15 kHz subcarrier spacing, this is a significant 17.3%, which could severely degrade performance. However, if 5G uses a wider subcarrier spacing of 240 kHz, the relative Doppler shift drops to only 1%, greatly reducing the impact on performance.

Thus, while Doppler shift increases linearly with carrier frequency, 5G's flexible subcarrier spacing allows it to keep the relative Doppler impact low, making it more efficient than 4G in high-mobility conditions.

3.9 Doppler Shift Issues in OFDM Systems

Orthogonal Frequency Division Multiplexing (OFDM) is known to suffer from significant performance degradation in high-mobility environments due to the presence of Doppler shifts. The Doppler effect, induced by relative motion between transmitter and receiver, introduces a frequency offset that destroys the orthogonality among subcarriers. This leads to the phenomenon of *Inter-Carrier Interference* (ICI), which severely impairs the reliability of the system.
The received OFDM signal in the presence of Doppler shift can be expressed as:

$$y(t) = \sum_{k=0}^{N-1} X_k e^{j2\pi f_k t}\, h(t)\, e^{j2\pi f_D t} + n(t) \tag{3.40}$$

where:

- X_k is the symbol transmitted on the k-th subcarrier,

- f_k is the frequency of the k-th subcarrier,
- f_D denotes the Doppler frequency shift,
- $h(t)$ represents the time-varying channel response,
- $n(t)$ is the additive noise.

The term $e^{j2\pi f_D t}$ introduces a time-dependent frequency offset, breaking the orthogonality of the subcarriers and resulting in ICI. The power of the resulting interference can be approximated by:

$$\text{ICI}_{\text{power}} \approx (\pi f_D T_s)^2 \tag{3.41}$$

where T_s denotes the OFDM symbol duration. As the Doppler frequency shift f_D increases, the ICI power increases quadratically, leading to a substantial reduction in system performance, particularly in terms of Bit Error Rate (BER) and spectral efficiency.
Additionally, the time-varying nature of the wireless channel causes symbol distortion and necessitates frequent and complex channel estimation and equalization techniques. These limitations make OFDM less effective in doubly dispersive channels, characterized by both time and frequency selectivity.
To address these challenges, alternative modulation schemes have been investigated. The next chapter introduces the *Orthogonal Time Frequency Space* (OTFS) modulation technique, which operates in the delay-Doppler domain. OTFS is specifically designed to exploit the sparsity of the wireless channel and to mitigate the adverse effects of Doppler, providing enhanced robustness and reliability in highly dynamic communication scenarios.

3.10 Channel estimation for mobile communications

The transmission channel in wireless communication systems is always changing because of things like Doppler shifts, multipath propagation, and environmental variations. Reliable data transmission requires precise understanding of the channel circumstances, especially in mobile settings where the channel fluctuates quickly over time. In order to enable effective equalization and demodulation at the receiver, channel estimate is essential for reducing the impacts of fading, interference, and signal distortions.
Effective channel estimation techniques are essential for modern communication technologies like OFDM and OTFS to maximize performance in a variety of scenarios. While more sophisticated techniques use time-frequency or delay-Doppler domain representations to improve resilience in extremely dynamic situations, traditional methods frequently presume quasi-static channels. The accuracy of channel estimation directly impacts key performance metrics such as bit error rate (BER) and spectral efficiency, making it a fundamental aspect of wireless system design.
This section explores the principles of channel estimation, the challenges posed by mobility, and the techniques employed in contemporary wireless systems to address these challenges.

In wireless communications, the baseband representation of a received signal can be expressed as:

$$\mathbf{y} = \mathbf{X}\mathbf{h} + \mathbf{n}, \tag{3.42}$$

where:

- $\mathbf{y} \in \mathbb{C}^{N\times 1}$ is the received signal vector,
- $\mathbf{X} \in \mathbb{C}^{N\times M}$ is the known pilot signal matrix,
- $\mathbf{h} \in \mathbb{C}^{M\times 1}$ is the channel coefficient vector to be estimated,
- $\mathbf{n} \in \mathbb{C}^{N\times 1}$ is the additive noise vector, typically modeled as complex Gaussian noise.

To estimate the channel vector $\mathbf{h}$, a common approach is the Least Squares (LS) estimation, which minimizes the squared error between the received and the modeled signal. The LS solution is derived by solving:

$$\min_{\mathbf{h}} \|\mathbf{y} - \mathbf{X}\mathbf{h}\|^2. \tag{3.43}$$

By differentiating with respect to $\mathbf{h}$ and setting the derivative to zero, we obtain the normal equation:

$$\mathbf{X}^T\mathbf{X}\hat{\mathbf{h}} = \mathbf{X}^T\mathbf{y}. \tag{3.44}$$

Solving for $\hat{\mathbf{h}}$, we get the LS channel estimate:

$$\hat{\mathbf{h}}_{\text{LS}} = (\mathbf{X}^T\mathbf{X})^{-1}\mathbf{X}^T\mathbf{y}. \tag{3.45}$$

This equation provides an estimate of the channel by projecting the received signal onto the transmitted pilot sequence. It assumes that $\mathbf{X}$ has full column rank so that $(\mathbf{X}^T\mathbf{X})^{-1}$ exists. Moreover, this estimation approach assumes that the channel remains constant over the duration of the pilot transmission, meaning that $\mathbf{h}$ does not change significantly within the observation window. This assumption is valid in slow-fading environments but may introduce estimation errors in fast time-varying channels.
The LS estimator does not exploit any statistical knowledge of the noise, making it suboptimal in scenarios with high noise levels. However, it remains computationally efficient and widely used in practical applications. More advanced estimators, such as the Minimum Mean Square Error (MMSE) estimator, incorporate prior knowledge of noise and channel statistics to improve performance.
In the most general scenario, the wireless channel exhibits time-varying characteristics. To estimate these variations, training bits can be transmitted at regular intervals, with data sent in between. By transmitting data at each discrete time interval, channel estimates can be obtained at those specific time points. However, the objective is to recover the channel state between these training intervals. This requires consideration of both time and frequency variations within the channel.
Frequency variation, in particular, introduces a challenge that makes regular sampling in the time domain insufficient. Instead of relying on uniformly spaced time intervals, a combination of time and frequency domain sampling is employed to achieve a more accurate representation of the channel's behavior.

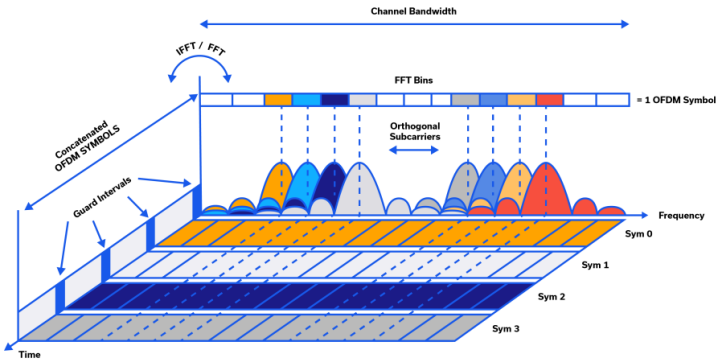

Figure 3.28: Frequency-time continuum showing OFDM symbols being binned, concatenated and transmitted sequentially.

This approach is facilitated through the use of **resource blocks**, which are fundamental to the operation of Orthogonal Frequency Division Multiplexing (OFDM). In OFDM, a resource block refers to a time-frequency unit, consisting of a set of subcarriers over a specific time duration. By utilizing the resource block structure, both time and frequency resources are allocated efficiently, allowing for effective management of time-varying and frequency-selective fading. This enables the channel's dynamic behavior to be captured and compensated for in a coherent manner.

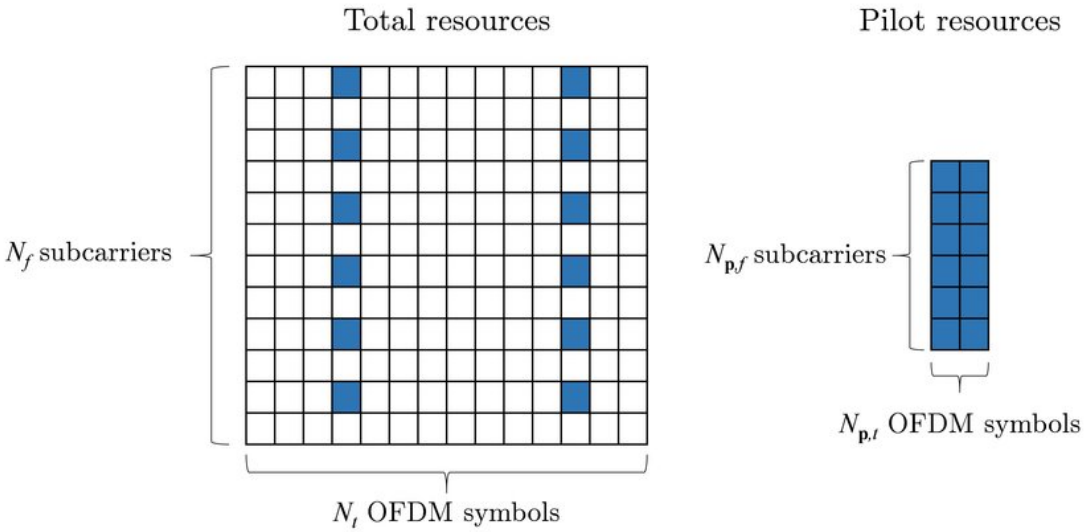

Figure 3.29: Resource block.

The resource block framework in OFDM facilitates the simultaneous management of

time and frequency variations, optimizing the channel estimation process. This strategic allocation of resources is essential for improving the reliability of data transmission in time-varying, frequency-selective channels, ultimately enhancing the overall system performance.

3.11 Channel Estimation using Cyclic Prefix and Fourier Matrix

The following section outlines the final channel estimation technique considered, which was selected for implementation based on various advantages that will be detailed below. This method is based on a Least Squares approach commonly used in the Universal Mobile Telecommunications System (UMTS), a standard within third-generation (3G) mobile networks that supports voice, data, and multimedia services.
One of the primary benefits of this approach is its efficient use of bandwidth enabled by **Time Division Duplexing (TDD)**. In TDD, the uplink and downlink transmissions share the same frequency band but occur in different time slots, resulting in symmetric channel characteristics such as fading, path loss, and interference. This symmetry simplifies the channel estimation process considerably.

3.11.1 Use of the Cyclic Prefix

A fundamental aspect that facilitates channel estimation is the introduction of a **cyclic prefix (CP)**. The CP is a repetition of the initial part of the transmitted signal, appended to its end. While originally intended to combat inter-symbol interference due to multipath propagation, in this context it enables the construction of a *circulant matrix*, which is a cornerstone of the estimation technique described.
The received signal can be mathematically modeled as:

$$y = w \cdot r \cdot h = w \cdot (r \cdot h)$$

Where:

- w represents the modulated signal,
- r denotes the Root Raised Cosine filter,
- h is the unknown channel response to be estimated.

3.11.2 Matrix Formulation

For estimation purposes, the system is expressed in matrix form:

$$y = A \cdot \tilde{h}$$

The matrix A is constructed as a circulant matrix from the sequence $w = [w_1, w_2, \ldots, w_n]$. The circulant structure enables the application of efficient diagonalization methods via the Fourier matrix F, defined as:

$$F_{N\times N} = [\bar{F}_{nm}], \quad \bar{F}_{nm} = e^{-j2\pi \frac{nm'}{N}}$$

Properties of the Fourier Matrix

The Fourier matrix F is employed due to its useful mathematical properties:

- **Unitarity**: The inverse is given by its Hermitian transpose,

$$F^{-1} = F^H = \frac{1}{N} F^*$$

  where F^H denotes the Hermitian transpose and F^* the complex conjugate.

- **Orthonormality**: The matrix satisfies the condition,

$$FF^H = F^H F = I$$

  where I is the identity matrix.

Based on these properties, the circulant matrix A can be expressed as:

$$A = F \cdot \tilde{A} \cdot F^H$$

3.11.3 Efficient Channel Estimation

By transforming the problem into the frequency domain, the computational complexity is significantly reduced:

- Direct matrix inversion has complexity $\mathcal{O}(N^3)$,
- Frequency domain methods reduce this to $\mathcal{O}(N \log N)$.

The estimation of the channel response is performed as follows:

$$\tilde{h} = F \cdot \tilde{A}^{-1} \cdot F^H \cdot y$$

3.11.4 Autocorrelation Properties of the Cyclic Prefix

It is essential that the cyclic prefix exhibit favorable **autocorrelation properties**. A CP with low sidelobe energy in its autocorrelation function leads to:

- Reduced inter-symbol interference (ISI),
- Increased reliability in channel estimation,
- Improved synchronization performance.

Poor autocorrelation characteristics can severely impact system synchronization and estimation accuracy.

3.11.5 Synchronization and Frequency Recovery

In practical implementations, the following operations are also crucial:

Frame Synchronization

Frame synchronization enables the receiver to identify the beginning of a signal frame accurately. Misalignment at this stage can destroy the circulant structure of the signal, leading to errors in the estimation process.

Frequency Recovery

Frequency offsets introduced by Doppler shifts or oscillator mismatches must be corrected through frequency recovery techniques. Without proper compensation, phase and amplitude distortions occur, undermining the accuracy of both synchronization and channel estimation.

3.12 Detection Techniques in OFDM Systems

Detection in Orthogonal Frequency Division Multiplexing (OFDM) systems is a critical process aimed at estimating the transmitted symbol vector from the received signal after it has propagated through a frequency-selective channel. Various detection schemes are employed depending on system requirements, noise conditions, and computational constraints.

3.12.1 Zero-Forcing (ZF) Detection

The Zero-Forcing (ZF) method aims to eliminate the channel effect by applying the inverse of the channel frequency response. Given the received signal in the frequency domain,

$$\mathbf{Y} = \mathbf{H}_f \mathbf{X} + \mathbf{W}, \tag{3.46}$$

where $\mathbf{H}_f$ is the diagonal matrix of the channel frequency response, $\mathbf{X}$ is the transmitted symbol vector, and $\mathbf{W}$ denotes additive white Gaussian noise (AWGN), the ZF estimate is obtained as:

$$\hat{\mathbf{X}}_{ZF} = \mathbf{H}_f^{-1} \mathbf{Y}. \tag{3.47}$$

Although straightforward, ZF amplifies noise significantly when the channel coefficients are small or close to zero.

3.12.2 Minimum Mean Square Error (MMSE) Detection

The Minimum Mean Square Error (MMSE) detector improves upon ZF by taking noise into account, minimizing the mean square error between the estimated and actual transmitted symbols. The MMSE estimate is given by:

$$\hat{\mathbf{X}}_{MMSE} = \left(\mathbf{H}_f^H \mathbf{H}_f + \sigma_w^2 \mathbf{I} \right)^{-1} \mathbf{H}_f^H \mathbf{Y}, \tag{3.48}$$

where σ_w^2 is the noise variance and $\mathbf{I}$ is the identity matrix. MMSE provides a compromise between noise enhancement and signal distortion, offering better performance than ZF in most practical scenarios.

3.12.3 Maximum Likelihood (ML) Detection

Maximum Likelihood (ML) detection provides optimal performance in terms of minimizing the probability of symbol error. The ML estimate is determined by solving the following optimization problem:

$$\hat{\mathbf{X}}_{ML} = \arg \min_{\mathbf{X} \in \mathcal{S}^N} \|\mathbf{Y} - \mathbf{H}_f \mathbf{X}\|^2, \tag{3.49}$$

where $\mathcal{S}$ is the symbol constellation (e.g., QPSK, 16-QAM). Despite its optimality, ML detection is computationally expensive due to the exhaustive search over all possible transmitted symbol combinations.

3.12.4 Iterative and Decision-Directed Techniques

For time-varying or imperfectly known channels, iterative methods such as Expectation-Maximization (EM) and Decision-Directed Channel Estimation (DDCE) are used to jointly refine symbol estimates and channel parameters. These approaches rely on previous symbol decisions to enhance detection accuracy over successive iterations, and are particularly useful in mobile or high Doppler environments.
Each detection technique presents a trade-off between complexity and performance. ZF is computationally simple but susceptible to noise enhancement, MMSE provides a noise-aware linear solution, and ML achieves optimal detection at the cost of exponential complexity. Iterative methods enhance performance under challenging channel conditions by leveraging temporal correlation and decision feedback.

Chapter 4

Orthogonal Time Frequency Space (OTFS)

Following the discussion of Orthogonal Frequency Division Multiplexing (OFDM) in the preceding chapter, it is necessary to present Orthogonal Time Frequency Space (OTFS), a revolutionary modulation approach that has lately drawn interest in the context of contemporary wireless communication systems. OFDM still has problems in high-mobility situations and strong Doppler shifts, while being widely used because of its resilience in frequency-selective fading conditions. In contrast, OTFS has been suggested as a viable way to get over these restrictions, providing better performance in terms of Doppler spread and robustness to delay. To comprehend the development of multi-carrier systems beyond OFDM, OTFS must be introduced. By dispersing the symbols over the time and frequency domains in a way that reduces interference from channel defects such time and frequency dispersion, OTFS's two-dimensional lattice structure improves signal transmission. This method is a strong contender for next-generation wireless networks, such as 5G and beyond, since it performs especially well in settings with significant Doppler shifts and fast time-varying channels. The purpose of this chapter is to examine the foundations of OTFS, emphasizing its main ideas, benefits, and possibilities for upcoming communication systems. The introduction of OTFS is necessary to give a thorough picture of the changing wireless communication technology landscape, even though a detailed comparison with OFDM will be discussed later.

In order to offer a comprehensive overview of the OTFS system, a schematic representation is provided below. The functional blocks illustrated in the diagram will be discussed and analyzed in detail in the subsequent sections, highlighting their specific roles within the modulation and demodulation processes.

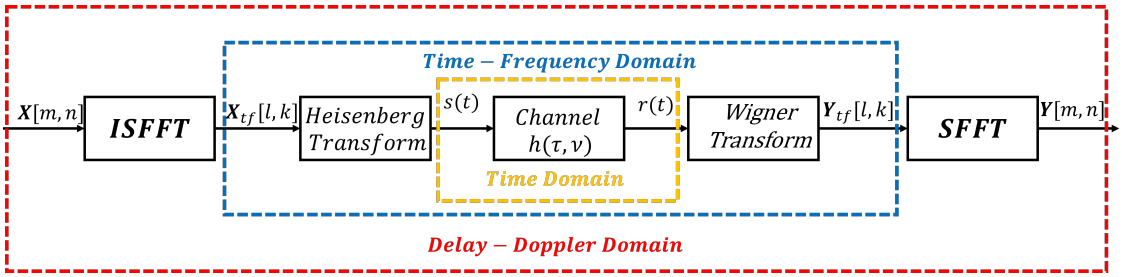

Figure 4.1: OTFS modulation/demodulation.

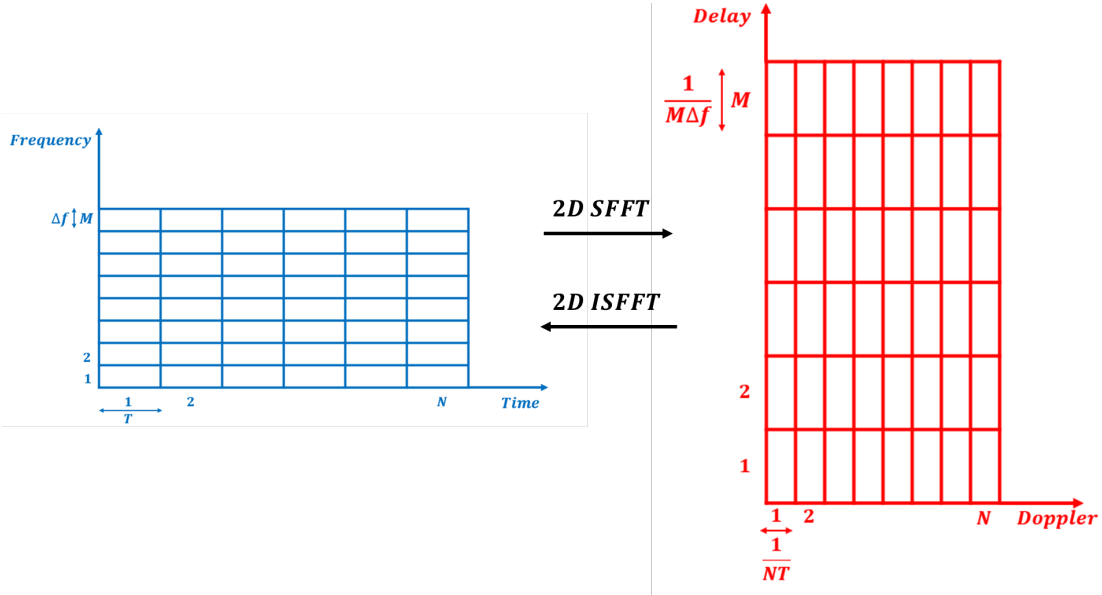

Figure 4.2: The discrete time-frequency grid (Λ) and delay-Doppler grid (Γ).

4.1 Modulation

1. The transmitter first maps symbols $\mathbf{X}[m,n]$ to NM samples $\mathbf{X}_{tf}[l,k]$ on the time-frequency grid Λ via **Inverse Symplectic Finite Fourier Transform (ISFFT)**

$$\mathbf{X}_{tf}[l,k] = \frac{1}{\sqrt{NM}} \sum_{n=0}^{N-1} \sum_{m=0}^{M-1} X[m,n]\, e^{j2\pi\left(\frac{nk}{N} - \frac{ml}{M}\right)} \tag{4.1}$$

for $l = 0, ..., M-1$ and $k = 0, ..., M-1$, where $\mathbf{X}_{tf} \in \mathbb{C}^{M \times N}$ represents the *time-frequency domain transmitted samples matrix*. The ISFFT corresponds to a 2D transformation which takes an M–point DFT of the columns of $\mathbf{X}$ and N–point IDFT of the rows of $\mathbf{X}$.

2. **2-D Modulator** – Heisenberg transform

Next, a time-frequency modulator converts the 2D samples $\mathbf{X}_{tf}[l,k]$ to a continuous-time waveform $s(t)$ using a transmit waveform $g_{tx}(t)$ as

$$s(t) = \sum_{k=0}^{N-1} \sum_{l=0}^{M-1} \mathbf{X}_{tf}[l,k] g_{\text{tx}}(t-kT) e^{j2\pi l \Delta f (t-kT)} \tag{4.2}$$

- $\mathbf{X}_{tf}[l,k]$: data symbols in time-frequency domain
- $g_{\text{tx}}(t)$: transmit pulse shaping function
- T: time spacing between symbols
- Δf: frequency spacing between subcarriers
- N, M: number of time and frequency slots

Simplifies to IFFT in the case of $N = 1$ and rectangular g_{tx}.

3. The signal $s(t)$ is transmitted over a time-varying channel with delay-Doppler channel response $h(\tau,\nu)$, corresponding to the delay-time response $g(\tau,t)$, where τ,ν are the channel delay and Doppler shift. Omitting the noise term, the received signal $r(t)$ is given by

$$r(t) = \iint h(\tau,\nu)\, s(t-\tau)\, e^{j2\pi\nu(t-\tau)}\, d\tau\, d\nu \tag{4.3}$$

$$= \int g(\tau,t)\, s(t-\tau) d\tau \tag{4.4}$$

where $g(\tau,t) = \int_\nu h(\tau,\nu) e^{j2\pi\nu(t-\tau)} d\nu$ is the *continuous delay-time channel response.*

4.2 Demodulation

1. **2-D Matched Filter** –Wigner transform

   At the receiver, the received signal $r(t)$ is passed through a matched filter computing the *cross-ambiguity function* $A_{g_{rx},r}(f,t)$ as

$$Y(f,t) = A_{g_{\text{rx}},r}(f,t) \triangleq \int r(t')\, g^*_{\text{rx}}(t'-t)\, e^{-j2\pi f(t'-t)} dt' \tag{4.5}$$

   and the sampling $Y(f,t)$ on the grid points Λ forms the *time-frequency domain received samples matrix* $\mathbf{Y}_{tf} \in \mathbb{C}^{M\times N}$ with entries

$$\mathbf{Y}_{tf}[l,k] = Y(f,t)\big|_{f=l\Delta f, t=kT} \tag{4.6}$$

   for $l = 0, ..., M-1$ and $k = 0, ..., M-1$

   - g_{rx}: receive pulse shaping function
   - $r(t)$: received signal

- $\mathbf{Y}_{tf}[l,k]$: demodulated time-frequency symbols

Simplifies to FFT in the case of $N = 1$ and rectangular g_{rx}.

2. Finally, the **Sympletic Fast Fourier Transform (SFFT)** is applied on $\mathbf{Y}_{tf}[m,n]$ to obtain the delay-Doppler domain samples as

$$\mathbf{Y}[m,n] = \frac{1}{\sqrt{NM}} \sum_{k=0}^{N-1} \sum_{l=0}^{M-1} \mathbf{Y}_{tf}[l,k]\, e^{-j2\pi\left(\frac{nk}{N} - \frac{ml}{M}\right)} \tag{4.7}$$

which form the *delay-Doppler domain received samples matrix* $Y \in \mathbb{C}^{M\times N}$. The SFFT corresponds to a 2D transformation which takes an M–point IDFT of the columns of $\mathbf{Y}$ and N-point DFT of the rows of $\mathbf{Y}$.

In summary, the OTFS modulation process begins by transforming the information symbols $\mathbf{X}[m,n]$, defined in the delay–Doppler domain, into the time–frequency domain representation $\mathbf{X}_{\text{tf}}[l,k]$ via the Inverse Symplectic Finite Fourier Transform (ISFFT). This intermediate signal is then converted into a continuous-time waveform $s(t)$ through the application of the Heisenberg transform. At the receiver, the incoming signal $r(t)$ is first projected onto the time–frequency domain using the Wigner transform. Subsequently, the Symplectic Finite Fourier Transform (SFFT) is employed to recover the symbols in the delay–Doppler domain, which are then processed for demodulation.

4.2.1 Alternative OTFS system

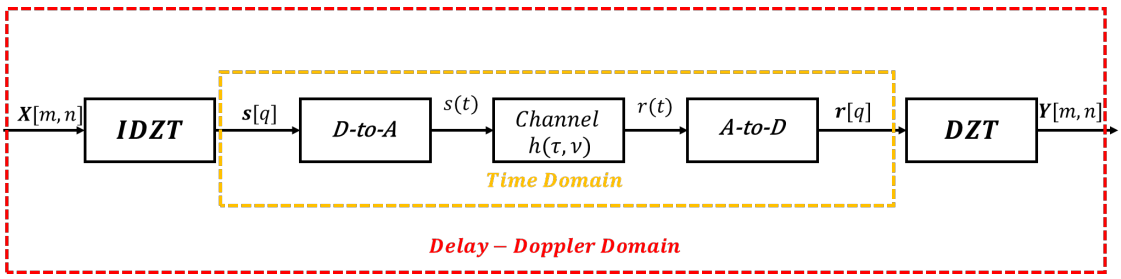

Figure 4.3: OTFS system diagram using the discrete Zak transform.

An alternative implementation of the OTFS transmitter involves the use of the **Inverse Discrete Zak Transform (IDZT)** to map symbols into the time domain, followed by a digital–to–analog (DA) conversion to generate the continuous-time transmit signal $s(t)$. On the receiver side, the received waveform $r(t)$ is first sampled using an analog–to–digital (AD) converter, after which the **Discrete Zak Transform (DZT)** is applied to retrieve the signal in the appropriate discrete domain for further processing.

4.2.2 Zak Transform in OTFS Modulation

In the context of OTFS modulation, the Zak transform provides a convenient way to convert between the delay-Doppler and time-domain representations through a two-dimensional to one-dimensional mapping and vice versa.

Transmitter Side: Inverse Discrete Zak Transform (IDZT). The inverse discrete Zak transform (IDZT) is used to convert the two-dimensional delay-Doppler domain symbol matrix $\mathbf{X}[m,n]$ into a one-dimensional time-domain signal $s[q]$. The IDZT is formally defined as:

$$\textbf{2D} \rightarrow \textbf{1D}$$

$$s[q] = s[m+nM] = \frac{1}{\sqrt{N}} \sum_{k=0}^{N-1} \mathbf{X}[m,k]\, e^{j2\pi kn/N}, \quad \text{with } m = 0,\ldots,M-1,\ n = 0,\ldots,N-1. \tag{7}$$

This process results in the one-dimensional signal $s[q]$, where the index $q = m + nM$ follows a row-wise stacking of the two-dimensional grid.

Receiver Side: Discrete Zak Transform (DZT). At the receiver, the time-domain signal $r[q]$ is converted back to the delay-Doppler domain using the Discrete Zak Transform (DZT), given by:

$$\textbf{1D} \rightarrow \textbf{2D}$$

$$\mathbf{Y}[m,n] = \frac{1}{\sqrt{N}} \sum_{k=0}^{N-1} r[m+kM]\, e^{-j2\pi kn/N}, \quad \text{with } m = 0,\ldots,M-1,\ n = 0,\ldots,N-1. \tag{8}$$

This inverse mapping re-establishes the two-dimensional structure of the signal in the delay-Doppler domain, which can then be used for further symbol detection.

For a more detailed discussion and additional properties of the Zak transform, the reader is referred to [7, Chapter 5].

4.3 Time-frequency domain analysis

If g_{tx} and g_{rx} are perfectly localized in time and frequency **(ideal pulses)**, then they satisfy the **bi-orthogonality condition**, and the input-output relation becomes:

$$\mathbf{Y}_{tf}[l,k] = \mathbf{H}_{tf}[l,k]\, \mathbf{X}_{tf}[l,k] \tag{4.8}$$

$\mathbf{H}_{tf} \in \mathbb{C}^{M\times N}$ is the *time-frequency domain channel matrix* with entries

$$\mathbf{H}_{tf}[l,k] = \iint h(\tau,\nu)\, e^{j2\pi\nu kT}\, e^{-j2\pi l\Delta f\tau}\, d\tau\, d\nu \tag{4.9}$$

for $l = 0, ..., M-1$ and $k = 0, ..., M-1$

- $h(\tau,\nu)$: delay-Doppler channel response
- T: symbol time spacing

- Δf: subcarrier spacing

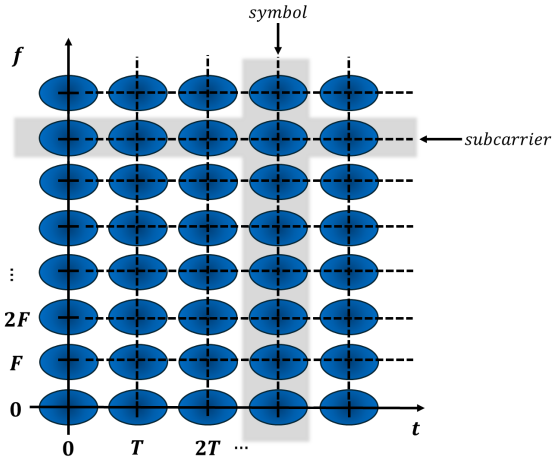

Figure 4.4: Time-Frequency domain.

When ideal transmit and receive pulses are used, each symbol transmitted in the time-frequency domain is independently scaled by a complex coefficient determined by the channel, resulting in a received symbol that is a complex-scaled version of the transmitted one. In practical scenarios, ideal pulse shaping is not achievable, and the wireless channel exhibits both delay and Doppler spread. As a result, inter-symbol interference (ISI) and inter-carrier interference (ICI) occur simultaneously in the time-frequency domain, preventing the use of simple single-tap equalization per symbol.

4.4 Delay-Doppler domain analysis

SFFT establishes a relationship between the delay-Doppler transmitted and received sample matrices and those in the time-frequency domain:

$$\mathbf{Y} = SFFT(\mathbf{Y}_{tf}), \tag{4.10}$$

$$\mathbf{X} = SFFT(\mathbf{X}_{tf}). \tag{4.11}$$

The delay-Doppler domain channel matrix of size $M \times N$ is related to the time-frequency channel matrix as

$$\mathbf{H}_{dd} = SFFT(\mathbf{H}_{tf}), \tag{4.12}$$

where

$$\mathbf{H}_{dd}[m,n] = \sum_{l}\sum_{k} \mathbf{H}_{tf}[l,k]\, e^{-j2\pi(\frac{nk}{N}-\frac{ml}{M})}. \tag{4.13}$$

The received signal in the delay-Doppler domain for pulses satisfying the biorthogonality criteria in the time-frequency domain can be expressed (by taking the SFFT of the left-hand side and the right-hand side of equation (4.8)) as

$$\begin{aligned}\mathbf{Y}[m,n] &= \mathbf{H}_{dd}[m,n] \circledast \mathbf{X}[m,n] \quad \text{(2D circular convolution)} \\ &= \sum_{m'} \sum_{n'} \mathbf{H}_{dd}[m',n']\, \mathbf{X}[[m-m']_M, [n-n']_N] \\ &= \sum_{i=1}^{P} g_i\, \mathbf{X}[[m-l_i]_M,\, [n-k_i]_N]\end{aligned} \tag{4.14}$$

for the case of integer delay and Doppler taps $l_i = \mathrm{l}_i$ and $k_i = \mathrm{k}_i$.

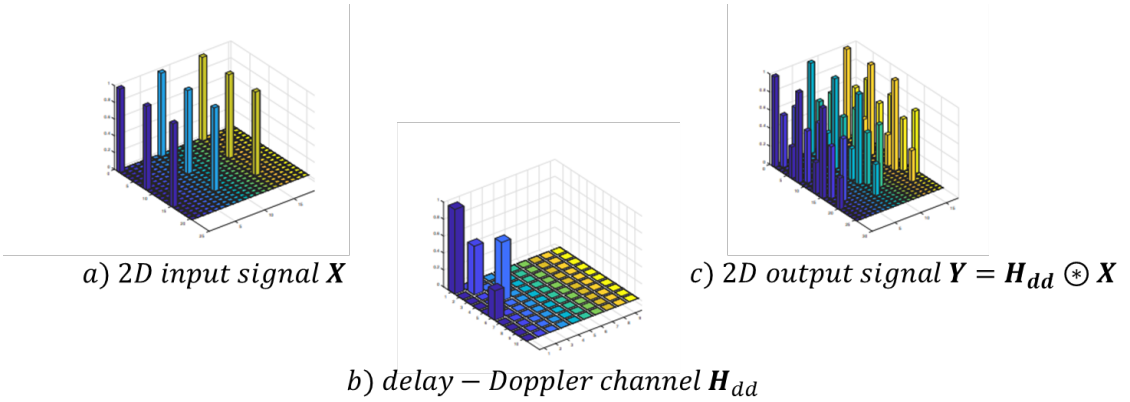

Figure 4.5: OTFS signals. Source: Adapted from [7]

Fig. 4.5 shows the received signal as a 2D circular convolution of the transmitted signal $\mathbf{X}$ with the channel $\mathbf{H}$. Even though, perfect biorthogonality cannot be achieved in practical cases, pulse shaping can be used to reduce the effect of the loss of the biorthogonality. This can be quantified by measuring the leakage outside each time-frequency block.

4.4.1 Ideal vs Rectangular Pulses (One CP per Frame)

The choice of transmit and receive pulses significantly impacts the system behavior. In particular, the comparison between *ideal* and *rectangular* pulses reveals key differences in both the time-frequency (TF) and delay-Doppler (DD) input-output relationships.

Ideal Pulses. When ideal pulses are employed, perfectly bi–orthogonal and well-localized in both time and frequency–the input-output relationship in the time–frequency domain is given by:

$$\mathbf{Y}_{\mathrm{tf}}[l,k] = \mathbf{H}_{\mathrm{tf}}[l,k]\, \mathbf{X}_{\mathrm{tf}}[l,k] \tag{4.15}$$

In this case, each symbol undergoes a simple complex scaling by the corresponding channel coefficient.
The corresponding delay-Doppler domain relation becomes a two-dimensional time-invariant convolution:

$$\mathbf{Y}[m,n] = \sum_{i=1}^{P} h_i\, \mathbf{X}[[m-l_i]_M, [n-k_i]_N] \tag{4.16}$$

where $[[\cdot]]_M$ and $[[\cdot]]_N$ denote modulo-M and modulo-N operations, respectively, ensuring circularity in both dimensions.

Rectangular Pulses. In practice, rectangular pulses are often used due to their simplicity and ease of implementation. However, they are not perfectly localized in the TF domain, leading to inter-symbol interference (ISI) and inter-carrier interference (ICI) caused by channel dispersion in both delay and Doppler:

$$\mathbf{Y}_{\text{tf}}[l,k] = \mathbf{H}_{\text{tf}}[l,k]\,\mathbf{X}_{\text{tf}}[l,k] + \text{ICI} + \text{ISI} \tag{4.17}$$

This degradation reflects the loss of perfect orthogonality due to pulse mismatch. Consequently, the DD domain relation becomes a two-dimensional time-variant filter:

$$\mathbf{Y}[m,n] = \sum_{i=1}^{P} h_i\,\alpha(m,n,l_i,k_i)\,\mathbf{X}[[m-l_i]_M,[n-k_i]_N] \tag{4.18}$$

where $\alpha(m,n,l_i,k_i)$ represents a phase rotation due to ICI and ISI, and is given by:

$$\alpha(m,n,l_i,k_i) = e^{\frac{j2\pi k_i(m-l_i)}{NM}} \cdot e^{j\frac{2\pi}{N}(n-k_i)\left\lfloor\frac{m-l_i}{M}\right\rfloor} \tag{4.19}$$

4.5 Compatibility with OFDM architecture

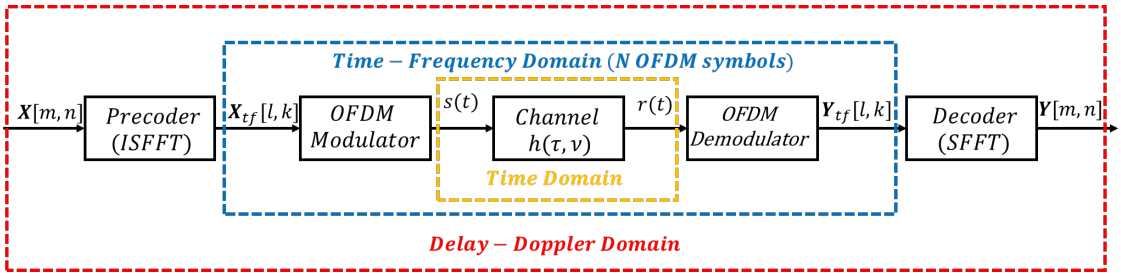

Figure 4.6: OTFS mod/demod, compatibility with OFDM architecture

This architecture allows OTFS to be layered on top of OFDM, making it easier to integrate into existing systems with minor modifications.

- OTFS is compatible with LTE system
- OTFS can be easily implemented by applying a precoding and decoding blocks on N consecutive OFDM symbols

4.6 OTFS Modulation: Matrix Form

The transformation from the delay-Doppler domain to the time domain can be described in two main steps:

- ISFFT

- Heisenberg Transform

4.6.1 Step 1: ISFFT (Inverse Symplectic Finite Fourier Transform)

The input symbols $\mathbf{X}[m,n]$ in the delay-Doppler (DD) domain are transformed into the time-frequency (TF) domain using the ISFFT:

$$\mathbf{X}_{\text{tf}} = \mathbf{F}_M \cdot \mathbf{X} \cdot \mathbf{F}_N^{\dagger} \tag{4.20}$$

where $\mathbf{F}_M, \mathbf{F}_N^{\dagger}$ represent the M-point Fourier transform and the N-point fourier transform.

4.6.2 Step 2: Heisenberg Transform

The time-frequency domain matrix $\mathbf{X}_{tf} \in \mathbb{C}^{M\times N}$ is then converted into a delay-time domain samples matrix $\tilde{\mathbf{X}} \in \mathbb{C}^{M\times N}$ through an M-point IFFT as

$$\tilde{\mathbf{X}} = \mathbf{F}_M^{\dagger} \cdot \mathbf{X}_{\text{tf}} = \mathbf{F}_M^{\dagger} \cdot \mathbf{F}_M \cdot \mathbf{X} \cdot \mathbf{F}_N^{\dagger} = \mathbf{X} \cdot \mathbf{F}_N^{\dagger} \tag{4.21}$$

where $\mathbf{I}_M = \mathbf{F}_M^{\dagger} \cdot \mathbf{F}_M$ denotes the $M \times M$ identity matrix, then the time domain samples vector is obtained as

$$\mathbf{s} = \text{vec}\left(\mathbf{G}_{\text{tx}} \cdot \mathbf{F}_M^{\dagger} \cdot \mathbf{X}_{\text{tf}}\right) = \text{vec}\left(\mathbf{G}_{\text{tx}} \cdot \mathbf{X} \cdot \mathbf{F}_N^{\dagger}\right) = \text{vec}\left(\mathbf{G}_{\text{tx}} \cdot \tilde{\mathbf{X}}\right) \in \mathbb{C}^{NM\times 1} \tag{4.22}$$

Here, $\mathbf{F}_M$ and $\mathbf{F}_N$ denote the DFT matrices of size M and N, respectively, and $\mathbf{G}_{\text{tx}} = \text{diag}[g_{\text{tx}}(0), g_{\text{tx}}(\frac{T}{M}), \ldots, g_{\text{tx}}(\frac{(M-1)T}{M})]$ is an $M \times M$ diagonal matrix representing the transmit pulse shaping.

4.6.3 Special Case: Rectangular Pulse Shaping

For rectangular pulse shaping, i.e., $\mathbf{G}_{\text{tx}} = \mathbf{I}_M$, the expression simplifies to:

$$\mathbf{s} = \text{vec}(\tilde{\mathbf{X}}) = \text{vec}(\mathbf{X} \cdot \mathbf{F}_N^{\dagger}) \tag{4.23}$$

This operation is equivalent to the well-known *Inverse Discrete Zak Transform (IDZT)*, and can be written as:

$$\mathbf{s} = \text{IDZT}\left\{\mathbf{X}\right\} = \text{vec}(\mathbf{X} \cdot \mathbf{F}_N^{\dagger}) \tag{4.24}$$

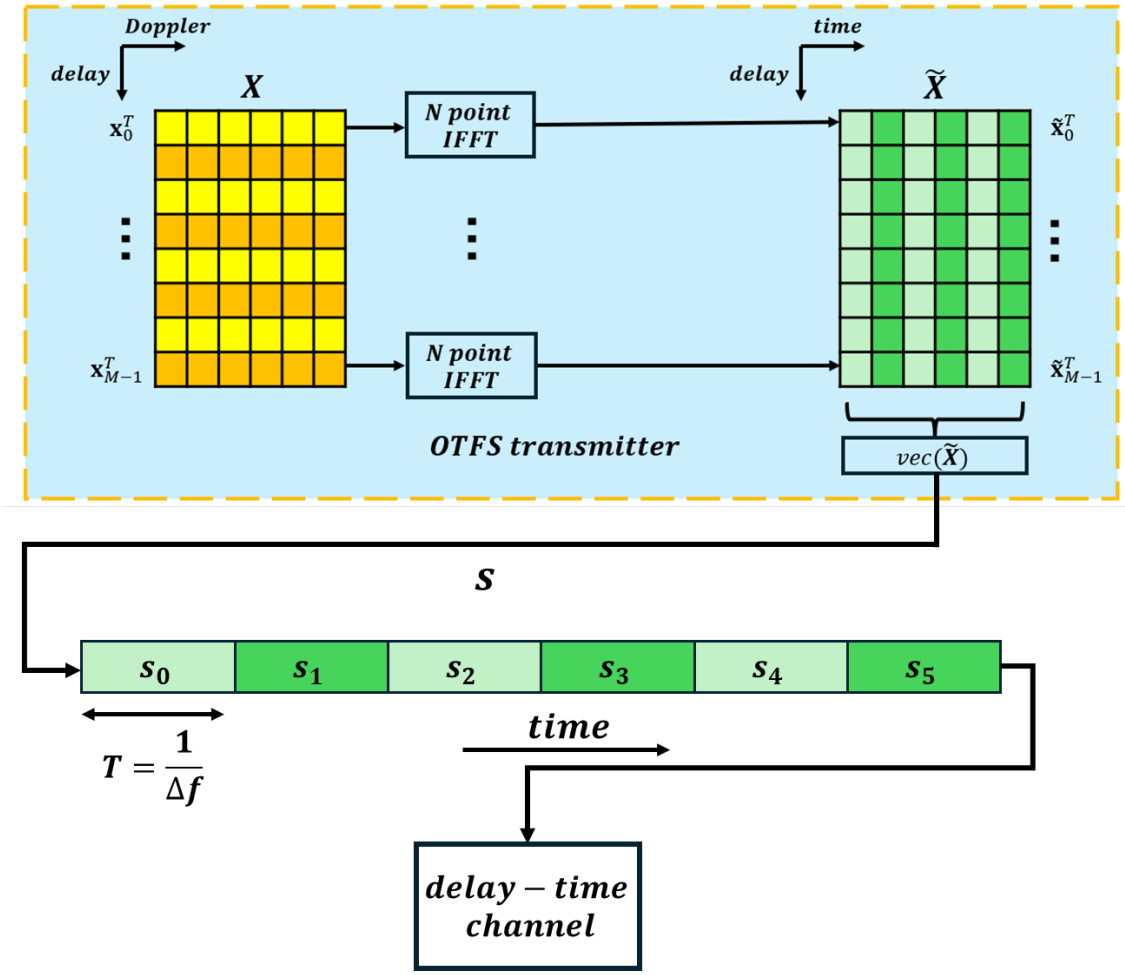

Figure 4.7: OTFS transmitter based on the IDZT using rectangular pulse shaping waveform (M=8, N=6). Reproduced by the author after [7].

4.7 OTFS Demodulation: Matrix Form

The OTFS demodulation process in matrix form consists of two main steps: transforming the received signal from the time domain to the time-frequency domain, and then applying a symplectic finite Fourier transform (SFFT) to reach the delay-Doppler domain.

4.7.1 Step 1: Wigner Transform (Time Domain to TF Domain)

The received vector $\mathbf{r} \in \mathbb{C}^{MN\times 1}$ is first reshaped into a matrix $\tilde{\mathbf{Y}} \in \mathbb{C}^{M\times N}$, using the inverse vectorization operation:

$$\tilde{\mathbf{Y}} = \mathbf{G}_{\text{rx}} \cdot \text{vec}_{M,N}^{-1}(\mathbf{r}) \tag{4.25}$$

where:

- the diagonal matrix $\mathbf{G}_{\text{rx}} = \text{diag}[g_{\text{rx}}(0), g_{\text{rx}}(\frac{T}{M}), \ldots, g_{\text{rx}}(\frac{(M-1)T}{M})] \in \mathbb{C}^{M\times M}$ is the receiver pulse shaping matrix.

The Wigner transform is then applied as:

$$\mathbf{Y}_{\text{tf}} = \mathbf{F}_M \cdot \tilde{\mathbf{Y}} \tag{4.26}$$

where:

- $\mathbf{F}_M$ is the DFT matrix of size $M \times M$,
- $\tilde{\mathbf{Y}}$ is the reshaped received signal.

4.7.2 Step 2: SFFT (TF to DD Domain)

The SFFT operation maps the TF domain representation to the delay-Doppler domain:

$$\mathbf{Y} = \mathbf{F}_M^{\dagger} \cdot \mathbf{Y}_{\text{tf}} \cdot \mathbf{F}_N \tag{4.27}$$

where:

- $\mathbf{F}_M^{\dagger}$ is the Hermitian (inverse) DFT matrix,
- $\mathbf{F}_N$ is the DFT matrix of size $N \times N$.

4.7.3 Special Case: Rectangular Pulse Shaping

When rectangular pulse shaping is used, the receive windowing becomes an identity matrix: $\mathbf{G}_{\text{rx}} = \mathbf{I}_M$. In this case, the transformation simplifies to:

$$\mathbf{Y} = \tilde{\mathbf{Y}} \cdot \mathbf{F}_N \tag{4.28}$$

4.7.4 Relation to the Discrete Zak Transform (DZT)

The entire demodulation process described above is equivalent to the application of the discrete Zak transform (DZT) to the received vector $\mathbf{r}$:

$$\mathbf{Y} = \text{DZT}\{\mathbf{r}\} = \text{vec}_{M,N}^{-1}(\mathbf{r}) \cdot \mathbf{F}_N \tag{4.29}$$

This highlights that the OTFS demodulator essentially applies a two-dimensional Fourier transform after proper reshaping of the received signal.

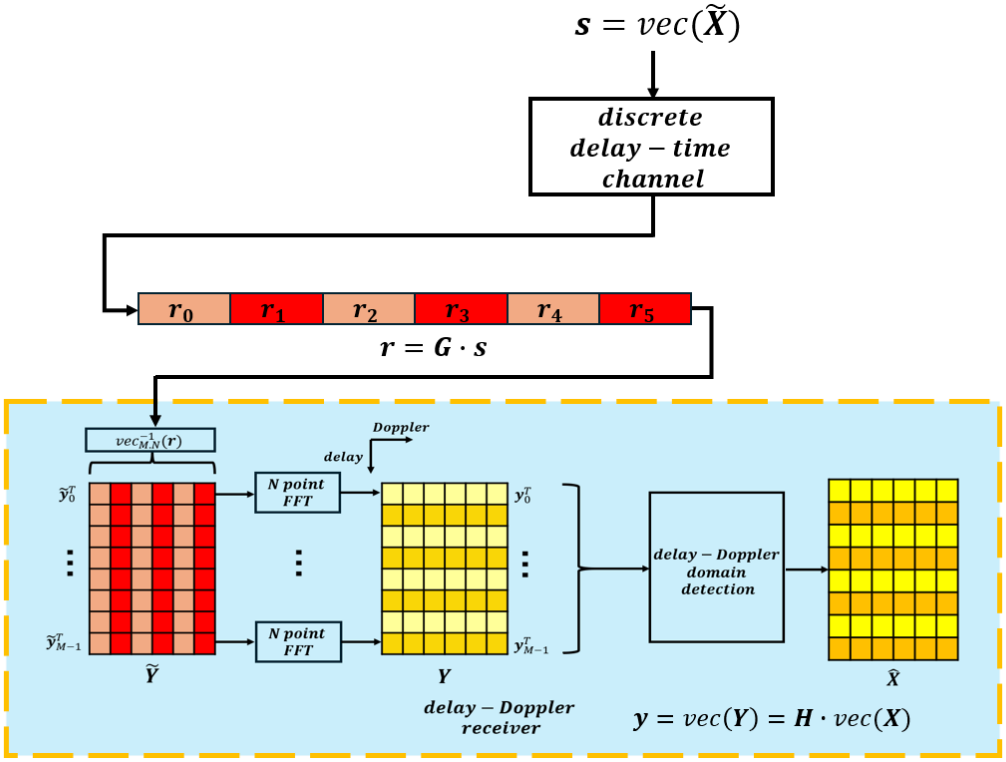

Figure 4.8: OTFS receiver based on the DZT using rectangular pulse shaping waveform (M=8, N=6). Reproduced by the author after [7].

For a more detailed treatment of the vectorized formulation of OTFS modulation and demodulation, the reader is referred to [7, Chapter 4].

4.8 OTFS Waveform Variants Based on Guard Interval

In practical OTFS implementations, the use of guard intervals is essential to mitigate inter-symbol interference (ISI) caused by multipath propagation. Two primary methods for guard interval insertion are *Cyclic Prefix* (CP) and *Zero Padding* (ZP). These can be applied either once per OTFS frame or to each symbol block within the frame, giving rise to different OTFS waveform structures. Additionally, reduced forms of both CP and ZP improve spectral efficiency at the cost of increased interference. These waveform variants are categorized into three main options, as described below.

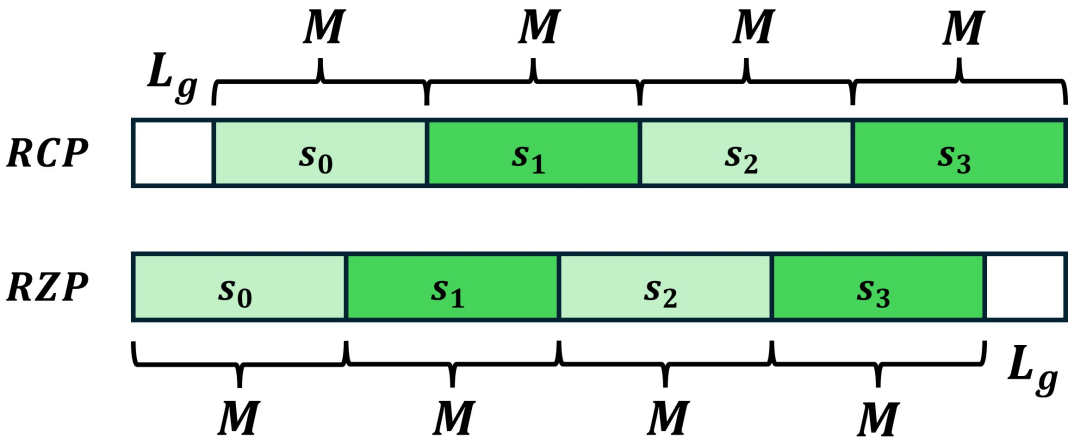

(a) A single CP/ZP is added to the frame.

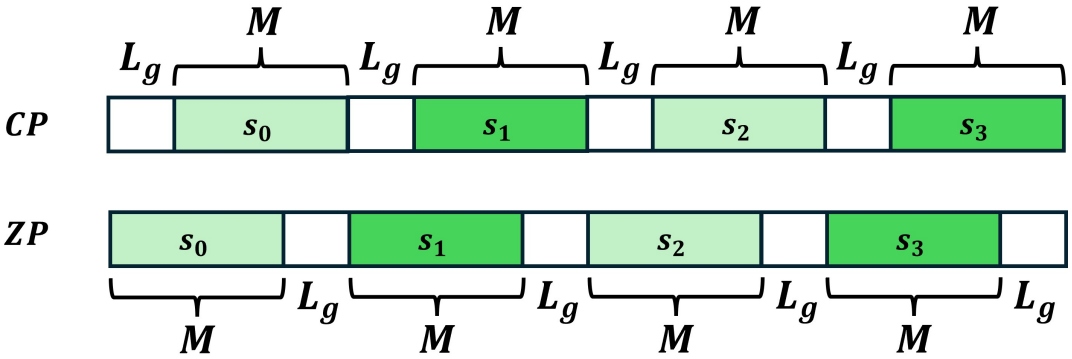

(b) A CP/ZP is added to each block.

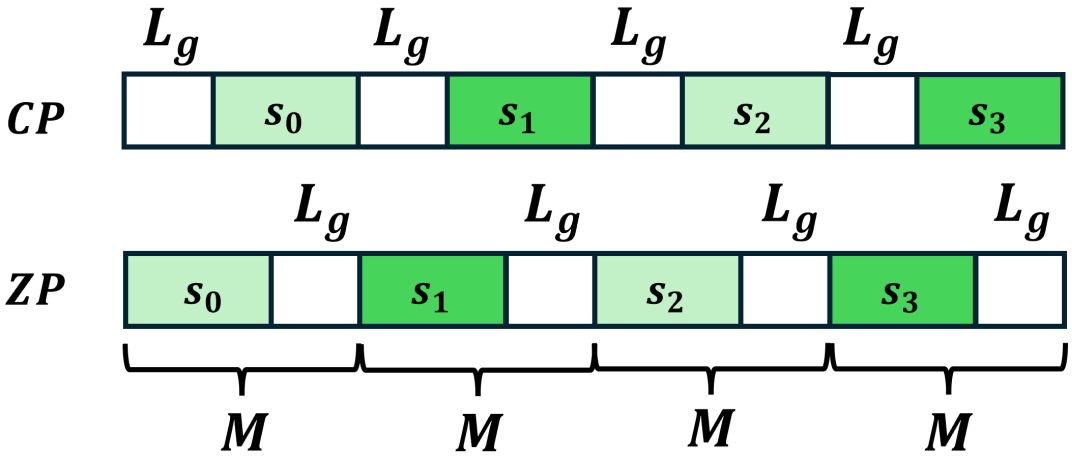

(c) A CP/ZP is included within each block.

Figure 4.9: Comparison of guard interval insertion methods in OTFS: (a) single CP/ZP for entire frame, (b) CP/ZP for each block, (c) embedded CP/ZP within each block. Reproduced by the author after [7].

Option (a): Single CP/ZP Per Frame (RCP/RZP-OTFS)

In this configuration, a single CP or ZP of length L_g is appended once at the beginning (for CP) or end (for ZP) of the complete OTFS frame consisting of NM samples:

$$\mathbf{x}_{\text{rcp}} = [\mathbf{x}[MN - L_g : MN - 1]; \mathbf{x}[0 : MN - 1]] \tag{4.30}$$

$$\mathbf{x}_{\text{rzp}} = [\mathbf{x}[0 : M - 1]; \mathbf{0}_{L_g}] \tag{4.31}$$

This structure minimizes guard overhead and improves spectral efficiency. However, the frame duration is extended to $T_f = (1 + \frac{L_g}{M})T$, which in turn reduces Doppler resolution $1/T_f$. Moreover, Doppler shifts are scaled by a factor $\gamma_g = 1 + \frac{L_g}{M}$, requiring correction at the receiver if the CP/ZP is discarded.

Option (b): CP/ZP Per Symbol Block (CP-OTFS / ZP-OTFS)

In this approach, a CP or ZP of length L_g is added to each symbol block of M samples:

$$\mathbf{x}_{\text{cp}} = \bigcup_{i=0}^{N-1} [\mathbf{x}_i[M - L_g : M - 1]; \mathbf{x}_i[0 : M - 1]] \tag{4.32}$$

$$\mathbf{x}_{\text{zp}} = \bigcup_{i=0}^{N-1} [\mathbf{x}_i[0 : M - 1]; \mathbf{0}_{L_g}] \tag{4.33}$$

This method preserves circular convolution (in the case of CP), enabling efficient FFT-based equalization and maintaining compatibility with traditional OFDM systems. However, the additional CP/ZP in every block increases the overall frame length and reduces the Doppler resolution due to the extended duration.

Option (c): Embedded CP/ZP with Frame Length Constraint

In this structure, the total frame duration is kept constant at MN samples by embedding CP or ZP within each symbol block. The number of information symbols per block is reduced to $M - L_g$:

$$\text{Frame length} = (M - L_g) \times N + L_g \times N = MN \tag{4.34}$$

The inserted CP/ZP is not discarded at the receiver, preserving the structure of the delay-Doppler grid without scaling. This option is advantageous when accurate Doppler shift estimation is required. However, the reduced data rate due to the smaller symbol block size must be considered.

Each waveform variant presents trade-offs between complexity, spectral efficiency, and Doppler resolution. The choice depends on the application scenario, with Option (a) suitable for bandwidth-limited systems, Option (b) offering compatibility with OFDM-based equalization, and Option (c) maintaining unscaled Doppler characteristics for high-precision estimation tasks.

For a more detailed discussion about all the variants of OTFS refer to [7, Chapter 4]

4.9 Channel Estimation in OTFS Systems

Accurate channel estimation is a critical component in Orthogonal Time Frequency Space (OTFS) modulation, as it directly impacts the performance of signal detection and equalization. Unlike conventional multicarrier systems such as OFDM, OTFS operates in the delay-Doppler domain, where the wireless channel is represented in a sparse and quasi-static manner, even under high mobility conditions. This unique property enables more robust and efficient communication in doubly dispersive environments. However, it also introduces specific challenges, as conventional estimation techniques based in the time-frequency domain may not directly apply.
In OTFS systems, the goal of channel estimation is to obtain an accurate representation of the delay-Doppler channel response $h[\nu, \tau]$, which captures the time delays and Doppler shifts induced by multipath and mobility. Estimation methods can be broadly categorized into pilot-based techniques, where known symbols or sequences are embedded within the OTFS frame, and blind techniques, which rely on statistical or structural properties of the transmitted data. Among pilot-based methods, two main strategies have emerged: embedded pilot schemes operating directly in the delay-Doppler domain, and time-domain schemes where pilots are processed before the SFFT demodulation. Each approach offers distinct trade-offs in terms of estimation accuracy, implementation complexity, and spectral efficiency. The following sections describe these methods in detail.

4.9.1 Embedded Pilot Delay-Doppler Channel Estimation

The Integer Doppler Case

Consider an OTFS system where each transmitted frame includes a single pilot symbol, N_g guard symbols, and $MN - N_g - 1$ data symbols. The transmitted symbols can be described as follows:

- The pilot symbol is denoted by x_p and has an associated pilot SNR given by:

$$\mathrm{SNR}_p = \frac{|x_p|^2}{\sigma_w^2}, \tag{4.35}$$

  where σ_w^2 represents the variance of the additive white Gaussian noise (AWGN).

- Data symbols are denoted as $x_d[m, n]$, where $[m, n]$ refers to their positions in the delay-Doppler grid. The data SNR is defined as:

$$\mathrm{SNR}_d = \frac{\mathbb{E}(|x_d[m, n]|^2)}{\sigma_w^2}. \tag{4.36}$$

- Guard symbols are represented by zeros and are used to eliminate interference between pilot and data symbols caused by multipath and Doppler spread.

Let $l_{\max}$ and $k_{\max}$ be the maximum delay and Doppler tap indices, respectively, across all channel paths.

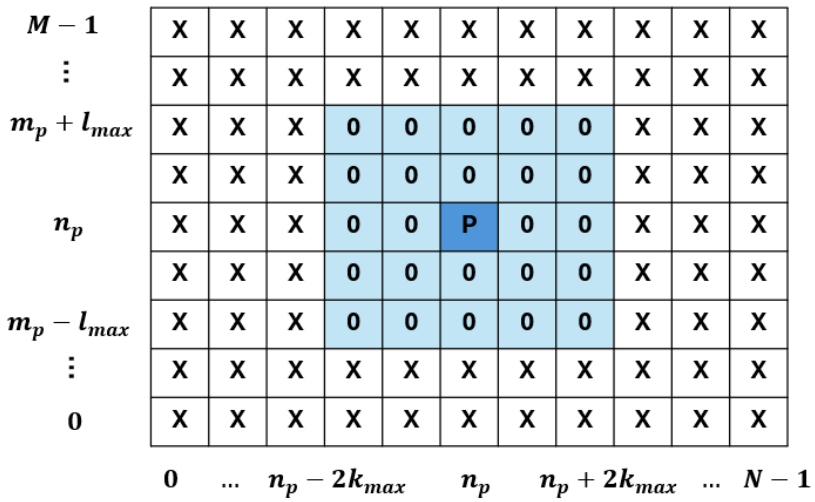

Figure 4.10: Tx symbol arrangement (P: pilot; 0: guard symbol; x: data symbol). Reproduced by the author after [7].

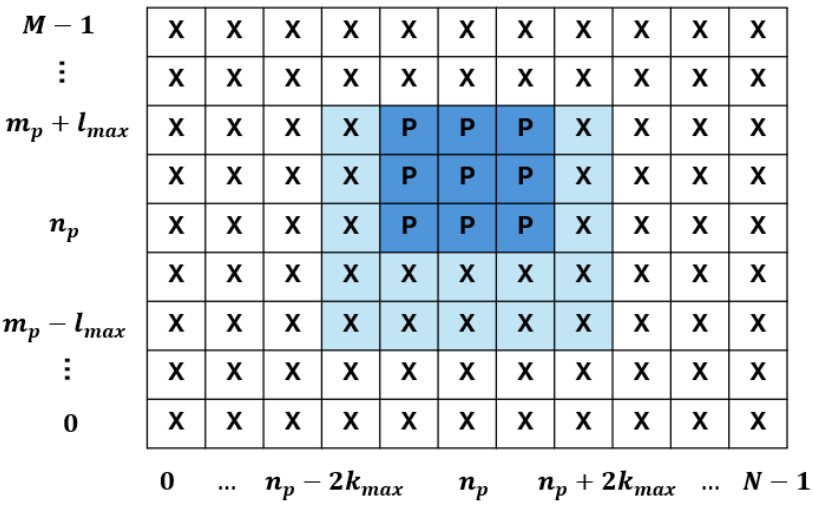

Figure 4.11: Rx symbol pattern (P: channel estimation; x: data detection). Reproduced by the author after [7].

The transmitted delay-Doppler grid $\mathbf{X}[m, n]$ is constructed as follows:

$$\mathbf{X}[m,n] = \begin{cases} x_p, & \text{if } m = m_p,\ n = n_p \\ 0, & \begin{cases} m_p - l_{\max} \le m \le m_p + l_{\max}, \\ n_p - 2k_{\max} \le n \le n_p + 2k_{\max},\ (m,n) \neq (m_p, n_p) \end{cases} \\ x_d[m,n], & \text{otherwise} \end{cases} \tag{4.37}$$

where (m_p, n_p) is the location of the pilot symbol in the grid. The guard region is chosen such that it fully absorbs any delay-Doppler spread from the pilot symbol, thereby avoiding pilot-data interference.
The number of guard symbols is computed as:

$$N_g = (2l_{\max} + 1)(4k_{\max} + 1) - 1, \tag{4.38}$$

resulting in a relative overhead:

$$\text{Overhead} = \frac{N_g + 1}{MN} = \frac{(2l_{\max} + 1)(4k_{\max} + 1)}{MN}. \tag{4.39}$$

At the receiver, channel estimation is performed using received symbols within the vicinity of the pilot symbol. Specifically, the received symbols used for estimation are $Y[m,n]$ such that $m_p \le m \le m_p + l_{\max}$ and $n_p - k_{\max} \le n \le n_p + k_{\max}$.
The received signal corresponding to a path with delay l_i and Doppler k_i is given by:

$$\mathbf{Y}[m_p + l_i, n_p + k_i] = g_i z^{k_i m_p} x_p, \tag{4.40}$$

where g_i is the channel gain and $z = e^{j2\pi/N}$. The goal is to estimate the set of channel parameters $\{g_i, l_i, k_i\}$ for each path $i = 1, \ldots, P$, where P is the (unknown) number of propagation paths.
The channel gain at each delay-Doppler location is estimated as:

$$\hat{g}[l,k] = \frac{\mathbf{Y}[m_p + l, n_p + k]}{x_p z^{k m_p}}. \tag{4.41}$$

To mitigate false path detections due to noise, a threshold-based criterion is applied. A binary decision variable $b[l,k]$ is defined as:

$$b[l,k] = \begin{cases} 1, & |\mathbf{Y}[m_p + l, n_p + k]| \ge T, \\ 0, & \text{otherwise}, \end{cases} \tag{4.42}$$

where T is a pre-defined threshold. The total number of detected paths is:

$$\hat{P} = \sum_{l,k} b[l,k]. \tag{4.43}$$

The channel input-output relationship in the delay-Doppler domain is reconstructed as:

$$\mathbf{Y}[m,n] = \sum_{l=0}^{l_{\max}} \sum_{k=-k_{\max}}^{k_{\max}} \hat{g}[l,k] b[l,k] z^{k(m-l)} \mathbf{X}[[m-l]_M, [n-k]_N]. \tag{4.44}$$

Additionally, the estimated Doppler response for each delay tap is given by:

$$\hat{\nu}_l(k) = b[l,k]\hat{g}[l,k], \tag{4.45}$$

and the Doppler spread vector per delay tap can be obtained as:

$$\hat{\nu}_{m,l}[[k]_N] = \hat{\nu}_l(k) z^{k(m-l)}. \tag{4.46}$$

The Fractional Doppler Case

In the presence of fractional Doppler shifts, each path contributes to all Doppler indices in a given delay bin. Thus, the received signal becomes:

$$\mathbf{Y}[m_p + l_i, n_p + k] = g_i z^{\kappa_i m_p} \zeta_N(\kappa_i - k) x_p, \tag{4.47}$$

where κ_i is the fractional Doppler shift and $\zeta_N(\cdot)$ denotes a periodic sinc function arising from the orthogonal basis used in the OTFS framework. Since the receiver observes only integer Doppler bins, each fractional Doppler component appears as multiple nearby components.
As in the integer case, a threshold-based scheme is used to suppress noise. The gain is estimated using the same expression:

$$\hat{g}[l,k] = \frac{\mathbf{Y}[m_p + l, n_p + k]}{x_p z^{k m_p}}, \tag{4.48}$$

with detection determined by:

$$b[l,k] = \begin{cases} 1, & |\mathbf{Y}[m_p + l, n_p + k]| \geq T, \\ 0, & \text{otherwise.} \end{cases} \tag{4.49}$$

Due to the non-zero nature of $\zeta_N(\kappa - k)$ over multiple k values, more paths than the actual number P may be detected. Nonetheless, many of these can be disregarded as $\zeta_N(\kappa - k)$ decays with increasing $|\kappa - k|$.
To prevent interference between pilot and data symbols, a wider guard region along the Doppler axis is required. Two schemes are typically employed:

Full Guard Symbols This approach involves placing the pilot in a completely isolated region:

$$\mathbf{X}[m,n] = \begin{cases} x_p, & m = m_p,\ n = n_p, \\ 0, & m_p - l_{\max} \leq m \leq m_p + l_{\max}, \\ x_d[m,n], & \text{otherwise.} \end{cases} \tag{4.50}$$

The number of guard symbols becomes:

$$N_g = (2l_{\max} + 1)N - 1, \tag{4.51}$$

with an overhead:

$$\text{Overhead} = \frac{2l_{\max} + 1}{M}. \tag{4.52}$$

Although this provides accurate estimation, it incurs higher spectral overhead (e.g., up to 8% in typical LTE scenarios).

Reduced Guard Symbols To improve spectral efficiency, only Doppler bins with significant pilot contributions are preserved. The transmitted grid is then:

$$\mathbf{X}[m,n] = \begin{cases} x_p, & m = m_p,\ n = n_p, \\ 0, & \begin{cases} m_p - l_{\max} \le m \le m_p + l_{\max}, \\ n_p - 2K'_{\max} \le n \le n_p + 2K'_{\max},\ (m,n) \neq (m_p, n_p) \end{cases} \\ x_d[m,n], & \text{otherwise} \end{cases} \tag{4.53}$$

Here, $k'_{\max} = \kappa_{\max} + k_g$, where $\kappa_{\max}$ is the maximum fractional Doppler shift and k_g is the number of additional guard bins to cover relevant Doppler spread. The total number of guard symbols and overhead is then the same as in the integer case:

$$N_g = (2l_{\max} + 1)(4k'_{\max} + 1) - 1, \tag{4.54}$$

$$\text{Overhead} = \frac{(2l_{\max} + 1)(4k'_{\max} + 1)}{MN}. \tag{4.55}$$

4.9.2 Embedded Pilot-Aided Delay-Time Domain Channel Estimation

Overview and System Setup

In OTFS systems, a simplified channel estimation method in the delay-time domain can be employed, particularly using the ZP-OTFS structure. In this model, a zero prefix (ZP) of length L_{ZP} is inserted into each OTFS block while keeping the overall frame length fixed at $M \times N$ samples. Unlike the configuration in Fig. 4.9(b), where adding and removing the ZP results in a scaling of the Doppler shifts by a factor $\gamma_g = \frac{M+L_{\text{ZP}}}{M}$, the configuration in Fig. 4.9(c) avoids this distortion and simplifies the estimation process.

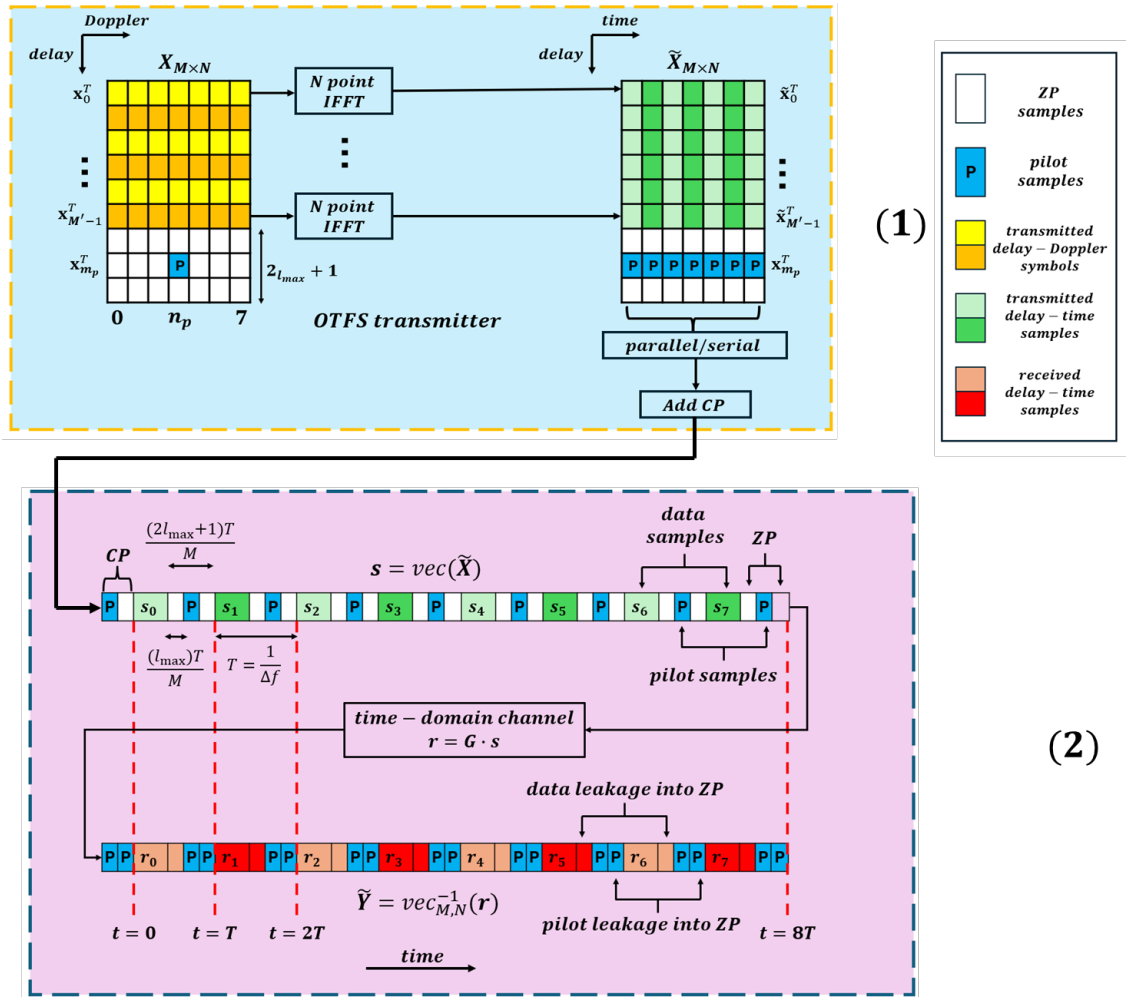

Figure 4.12: Pilot and data placement in ZP-OTFS (N=8,M=9) systems for time domain channel estimation. (1) ZP-OTFS transmitter. (2) Time domain operation. Reproduced by the author after [7].

Compared to estimation in the delay-Doppler domain, delay-time domain channel estimation requires fewer parameters, making it particularly efficient for high-mobility scenarios. As illustrated in Fig. 4.12, due to the periodic pilot insertion within the ZP, the channel impulse response at the l-th delay tap can be directly estimated at the pilot locations $(m_p + nM)T$ for $n = 0, \ldots, N-1$. These discrete estimates are then interpolated—either linearly or using spline methods—to reconstruct the full time-domain channel for each delay tap. Notably, for vehicular speeds up to 500 km/h, linear interpolation has been shown to be sufficient for accurate estimation.

Pilot Placement in the Delay-Doppler Grid

The pilot, guard, and data symbols are arranged on the delay-Doppler grid as shown in Fig. 4.12(1). Denote $x_m \in \mathbb{C}^{1\times N}$ as the m-th row of the OTFS matrix $\mathbf{X} \in \mathbb{C}^{M\times N}$. x_p

and $x_d[m,n]$ represent the pilot and data symbols at positions (m_p, n_p) and (m,n) in the delay-Doppler grid, respectively. Zero values are used to represent guard symbols. The symbol arrangement is thus given by

$$\mathbf{x}_m^T[n] = \begin{cases} x_p & \text{if } m = m_p,\ n = n_p, \\ 0 & \text{if } m \neq m_p,\ 0 < |n - n_p| \leq 2k_{\max}, \\ x_d[m,n] & 0 \leq n \leq N-1,\ 0 \leq m \leq M'-1. \end{cases} \tag{4.56}$$

To avoid interference between data and pilot due to channel delay spread, $l_{\max}$ guard symbols are inserted on either side of the pilot along the delay axis. The number of guard symbols is $N_g = (2l_{\max}+1)N - 1$, resulting in an overhead of $\frac{2l_{\max}+1}{M}$.
An N-point IFFT is applied to each row x_m. The pilot-embedded row x_{m_p} is transformed to:

$$\tilde{\mathbf{x}}_{m_p}^T = \mathbf{x}'_m \mathbf{F}_N^\dagger = x_p \left[\mathbf{F}_N^\dagger(n_p, 0), \ldots, \mathbf{F}_N^\dagger(n_p, N-1) \right],$$

where $\mathbf{F}_N^\dagger$ is the inverse DFT matrix. The resulting matrix $\tilde{\mathbf{X}} = [\tilde{\mathbf{x}}_0^T, \ldots, \tilde{\mathbf{x}}_{M-1}^T]^T$ is vectorized into $\mathbf{s} = \text{vec}(\tilde{\mathbf{X}})$ for transmission. To ensure continuity in the received signal, a cyclic prefix of $(l_{\max}+1)$ samples—copied from the end of the frame—is prepended. This prefix includes a replica of the pilot sample needed to interpolate earlier samples during estimation.

Delay-Time Domain Channel Estimation

After transmission over a time-varying channel, the received time-domain signal $r = Gs$, where G is the time-domain channel matrix. This is reshaped into the matrix $\tilde{\mathbf{Y}} = [\tilde{\mathbf{y}}_0, \ldots, \tilde{\mathbf{y}}_{M-1}]^T$. Based on the delay-time input-output relationship, we obtain:

$$\tilde{\mathbf{y}}_{m_p+l}[n] = \sum_{l' \in \mathcal{L}} g^{\text{s}}[l', m_p + l + nM]\, \tilde{\mathbf{x}}_{m_p+l-l'}[n]. \tag{4.57}$$

where $\mathcal{L}$ is the set of active delay taps. Due to the insertion of guard symbols, the term $\tilde{x}_{m_p+l-l'}[n] = 0$ for $0 < |l - l'| \leq l_{\max}$, leading to a simplified estimation:

$$\hat{g}^{\text{s}}[l, m_p + l + nM] = \frac{\tilde{\mathbf{y}}_{m_p+l}[n]}{\tilde{\mathbf{x}}_{m_p}[n]}, \quad \forall l \in \mathcal{L}. \tag{4.58}$$

These estimated values provide sampled instances of the delay-time domain channel, which must be interpolated to reconstruct the full channel profile over time.

Channel Reconstruction via Interpolation

The sampled estimates $\hat{g}^{\text{s}}[l, m_p + l + nM]$ are spaced by M samples along the time axis. To accurately reconstruct the delay-time channel, the Nyquist sampling theorem must be satisfied. In this scenario, the channel is sampled at pilot positions that are spaced every M symbols in time, leading to an effective subsampling frequency:

$$f_s' = \frac{f_s}{M}, \tag{4.59}$$

where f_s is the original sampling frequency, typically equal to the system bandwidth, and M is the number of Doppler bins in the OTFS grid.
According to the Nyquist criterion, in order to avoid aliasing and allow accurate reconstruction, the subsampling frequency must be at least twice the maximum Doppler frequency component $\nu_{\max}$. Therefore, the following condition must hold:

$$\nu_{\max} \leq \frac{f_s'}{2} = \frac{f_s}{2M}. \tag{4.60}$$

Given that the subcarrier spacing Δf in OTFS satisfies $f_s = N\Delta f$, where N is the number of delay bins, the inequality can also be expressed as:

$$\nu_{\max} \leq \frac{N\Delta f}{2M}. \tag{4.61}$$

This condition ensures that the time variation of each delay tap—due to different Doppler components—can be captured accurately using interpolation. For typical OTFS systems operating under the *underspread* channel assumption, this requirement is generally met. To reconstruct the full delay-time channel response, linear or spline interpolation is applied to the sampled values.

4.10 Detection Methods for OTFS

Detection in Orthogonal Time Frequency Space (OTFS) modulation plays a critical role in recovering transmitted information symbols from received signals that have undergone delay-Doppler spreading.
A range of detection methods have been proposed, including linear equalization techniques, such as Linear Minimum Mean Square Error (LMMSE), as well as more advanced iterative algorithms like Message Passing (MP), Maximum-ratio combining (MRC), and Turbo-based detection. Each method balances complexity and performance differently, depending on the channel conditions and system requirements.

4.10.1 Overview of OTFS input-output relation

In the context of a single-antenna OTFS system, a frame of duration NT is assumed to span a bandwidth of $M\Delta f$, where $T = 1/\Delta f$ and Δf denotes the subcarrier spacing. The transmitted and received data symbols in the delay-Doppler domain are represented by the matrices $\mathbf{X} \in \mathbb{C}^{M\times N}$ and $\mathbf{Y} \in \mathbb{C}^{M\times N}$, respectively. By vectorizing the transposes of these matrices, namely $\mathbf{X}^T$ and $\mathbf{Y}^T$, one obtains the corresponding sample vectors $\mathbf{x} \in \mathbb{C}^{NM\times 1}$ and $\mathbf{y} \in \mathbb{C}^{NM\times 1}$. These vectors consist of M sub-vectors of length N, each corresponding to a block along the Doppler axis:

$$\mathbf{x} = \begin{bmatrix} \mathbf{x}_0 \\ \vdots \\ \mathbf{x}_{M-1} \end{bmatrix} = \mathrm{vec}(\mathbf{X}^T), \quad \mathbf{y} = \begin{bmatrix} \mathbf{y}_0 \\ \vdots \\ \mathbf{y}_{M-1} \end{bmatrix} = \mathrm{vec}(\mathbf{Y}^T), \tag{4.62}$$

with $\mathbf{x}_m, \mathbf{y}_m \in \mathbb{C}^{N\times 1}$ for $m = 0, \ldots, M-1$. The relation between the transmitted and received vectors in the delay-Doppler domain can then be expressed as a linear system:

$$\mathbf{y} = \mathbf{H} \cdot \mathbf{x} + \mathbf{z}, \tag{4.63}$$

where $\mathbf{H} \in \mathbb{C}^{NM\times NM}$ represents the delay-Doppler channel matrix, and $\mathbf{z} \in \mathbb{C}^{NM\times 1}$ denotes the additive white Gaussian noise (AWGN) vector with zero mean and variance σ_w^2.

4.11 Single-tap frequency domain equalizer

The single-tap frequency domain equalization operates on the assumption that the multipath channel is slowly changing in time, with each subcarrier remaining orthogonal after transmission. In slowly time-varying channels, this enables a good OTFS detection approach by enabling low complexity equalization in the frequency domain.

4.11.1 Single-Tap Equalizer for RCP-OTFS

In the Reduced Cyclic Prefix OTFS (RCP-OTFS) configuration, a single cyclic prefix is applied to the entire OTFS frame. The vectors $\mathbf{s} \in \mathbb{C}^{NM\times 1}$ and $\mathbf{r} \in \mathbb{C}^{NM\times 1}$ represent the time-domain transmitted and received signals, respectively. These signals are derived from the corresponding delay-Doppler domain samples through an inverse discrete Fourier transform, as defined in prior formulations.
Assuming the use of rectangular pulse shaping waveforms, the vectorized input-output relationship in the time domain can be described by the linear model:

$$\mathbf{r} = \mathbf{G} \cdot \mathbf{s} + \mathbf{w}, \tag{4.64}$$

where $\mathbf{G} \in \mathbb{C}^{NM\times NM}$ denotes the time-domain channel matrix, and $\mathbf{w} \in \mathbb{C}^{NM\times 1}$ is the additive white Gaussian noise (AWGN) vector, characterized by a zero mean and variance σ_w^2.
In scenarios with low mobility, the channel matrix $\mathbf{G}$ can be approximated as circulant. Under this assumption, the model can be efficiently analyzed in the frequency domain. By applying an NM-point discrete Fourier transform, the time-domain vectors are converted as:

$$\check{\mathbf{s}} = \mathbf{F}_{MN} \cdot \mathbf{s}, \quad \check{\mathbf{r}} = \mathbf{F}_{MN} \cdot \mathbf{r}, \tag{4.65}$$

where $\mathbf{F}_{MN}$ is the normalized Fourier transform matrix. The frequency-domain representation of the received signal becomes:

$$\check{\mathbf{r}} = \check{\mathbf{G}} \cdot \check{\mathbf{s}} + \check{\mathbf{z}}, \tag{4.66}$$

with $\check{\mathbf{G}} = \mathbf{F}_{MN} \cdot \mathbf{G} \cdot \mathbf{F}_{MN}^{\dagger}$ and $\check{\mathbf{z}} = \mathbf{F}_{MN} \cdot \mathbf{w}$. Given the circulant structure of $\mathbf{G}$, the matrix $\check{\mathbf{G}}$ becomes diagonal in the frequency domain, which allows for simple per-tone equalization.

The transmitted frequency-domain samples can then be estimated using a Zero-Forcing (ZF) criterion as:

$$\check{\mathbf{s}}[q] = \frac{\check{\mathbf{r}}[q]}{\check{\mathbf{G}}[q,q]}, \quad q = 0, \ldots, NM-1. \tag{4.67}$$

To address the issue of noise amplification in cases where the channel frequency response $\hat{G}[q,q]$ has low magnitude, a Minimum Mean Square Error (MMSE) equalizer can be employed. The MMSE-based estimate is given by:

$$\check{\mathbf{s}}[q] = \frac{\check{\mathbf{G}}^*[q,q] \cdot \check{\mathbf{r}}[q]}{|\check{\mathbf{G}}[q,q]|^2 + \sigma_w^2}, \quad q = 0, \ldots, NM-1. \tag{4.68}$$

This approach generally provides improved robustness in the presence of deep fades or spectral nulls, as it mitigates the effects of channel inversion under low signal-to-noise ratio conditions. Then the equalized frequency domain samples vector is converted to time domain using the MN point IFFT operation as

$$\hat{\mathbf{s}} = \mathbf{F}_{MN}^{\dagger} \cdot \check{\mathbf{s}}, \tag{4.69}$$

that is then transformed back to the delay-Doppler domain to obtain the estimated symbols vector

$$\hat{\mathbf{x}} = \mathbf{I}_M \otimes \mathbf{F}_N \cdot \mathbf{I}^{\top} \cdot \hat{s}. \tag{4.70}$$

4.12 Block-wise single-tap equalizer for CP-OTFS

In time-frequency selective multipath channels, a block-wise single-tap equalizer is often employed to reduce computational complexity. For RCP-OTFS, diagonalizing the channel matrix $\mathbf{G}$ of size $NM \times NM$ results in a complexity of $\mathcal{O}(2NM\log_2(NM))$ complex multiplications. However, when using CP-OTFS, where a cyclic prefix is added to each of the N blocks, the matrix $\mathbf{G}$ becomes block diagonal with circulant submatrices $\mathbf{G}_{n,0} \in \mathbb{C}^{M\times M}$, allowing the complexity to drop significantly to $\mathcal{O}(2NM\log_2(M))$.
The time domain input-output relation is given block-wise for $n = 0, \ldots, N-1$ by:

$$\mathbf{r}_n = \mathbf{G}_{n,0} \cdot \mathbf{s}_n + \mathbf{w}_n, \tag{4.71}$$

where $\mathbf{s}_n, \mathbf{r}_n, \mathbf{w}_n \in \mathbb{C}^{M\times 1}$ denote the transmitted, received, and noise vectors, respectively. The corresponding block-wise relation in the time-frequency domain is:

$$\check{\mathbf{y}}_n = \check{\mathbf{H}}_{n,0} \cdot \check{\mathbf{x}}_n + \check{\mathbf{w}}_n, \tag{4.72}$$

with

$$\check{\mathbf{H}}_{n,0} = \mathbf{F}_M \cdot \mathbf{G}_{n,0} \cdot \mathbf{F}_M^{\dagger}, \tag{4.73}$$

$$\check{\mathbf{y}}_n = \mathbf{F}_M \cdot \mathbf{r}_n. \tag{4.74}$$

The MMSE-based single-tap equalizer for each subcarrier m is then given by:

$$\check{\mathbf{x}}_n[m] = \frac{\check{\mathbf{H}}^*_{n,0}[m,m]\check{\mathbf{y}}_n[m]}{|\check{\mathbf{H}}_{n,0}[m,m]|^2 + \sigma_w^2}, \tag{4.75}$$

where the estimated symbol includes contributions from intercarrier interference (ICI):

$$\check{\mathbf{y}}_n[m] = \tilde{\mathbf{H}}_{n,0}[m,m]\check{\mathbf{x}}_n[m] + \sum_{m'=0,m'\neq m}^{M-1} \check{\mathbf{H}}_{n,0}[m,m']\check{\mathbf{x}}_n[m'] + \check{\mathbf{w}}_n[m]. \tag{4.76}$$

The transformation of estimated frequency domain symbols back to the time domain and subsequently to the delay-Doppler domain is carried out via:

$$\hat{\mathbf{s}}_n = \mathbf{F}_M^\dagger \cdot \check{\mathbf{x}}_n, \tag{4.77}$$

$$\hat{\mathbf{x}} = (\mathbf{I}_M \otimes \mathbf{F}_N) \cdot \mathbf{P}^{\mathrm{T}} \cdot \hat{\mathbf{s}}. \tag{4.78}$$

Note that this processing chain, especially equations effectively constitutes the SFFT and ISFFT operations used in OTFS modulation.

4.13 LMMSE Detection for OTFS

In high mobility scenarios, the performance of the single-tap equalizer suffers due to Doppler-induced intercarrier interference (ICI). To mitigate this, a more robust detection scheme is employed: the *Linear Minimum Mean-Square Error* (LMMSE) detector. This method offers improved performance in both static and high mobility wireless channels, at the cost of higher computational complexity. It is particularly useful when the Doppler spread leads to dense channel matrices, which are not well-handled by simple equalizers.

Delay-Doppler Domain LMMSE Detection

Starting from the input-output relation in the delay-Doppler domain, the LMMSE estimate of the symbol vector $\mathbf{x}$ is given by:

$$\hat{\mathbf{x}} = \left(\mathbf{H}^\dagger\mathbf{H} + \sigma_w^2\mathbf{I}_{MN}\right)^{-1} \cdot \mathbf{H}^\dagger \cdot \mathbf{y}, \tag{4.79}$$

where $\mathbf{H}$ is the effective channel matrix in the delay-Doppler domain and σ_w^2 denotes the AWGN noise variance.
Although this operation provides good accuracy, it involves inverting an $NM \times NM$ matrix, which can be computationally intensive unless the matrix $\mathbf{H}$ has a sparse structure. For channels with a limited number of significant delay-Doppler taps, this sparsity can be exploited to reduce computational load.

Time Domain LMMSE Detection

Alternatively, detection can be performed directly in the time domain. For RCP-OTFS or RZP-OTFS, the corresponding LMMSE estimate of the transmitted time-domain samples is given by:

$$\hat{\mathbf{s}} = \left(\mathbf{G}^{\dagger}\mathbf{G} + \sigma_w^2 \mathbf{I}_{MN}\right)^{-1} \cdot \mathbf{G}^{\dagger} \cdot \mathbf{r}, \tag{4.80}$$

where $\mathbf{G}$ is the time-domain channel matrix and $\mathbf{r}$ is the received signal vector.
This computation also involves inversion of a large $NM \times NM$ matrix. However, in the case of CP-OTFS or ZP-OTFS, where $\mathbf{G}$ is block-diagonal with circulant blocks $\mathbf{G}_{n,0}$, the inversion can be performed block-wise for each n:

$$\hat{\mathbf{s}}_n = \left(\mathbf{G}_{n,0}^{\dagger}\mathbf{G}_{n,0} + \sigma_w^2 \mathbf{I}_M\right)^{-1} \cdot \mathbf{G}_{n,0}^{\dagger} \cdot \mathbf{r}_n, \tag{4.81}$$

for $n = 0, \ldots, N-1$. This significantly reduces complexity by operating on $M \times M$ matrices rather than the full $NM \times NM$ system.

4.14 Message Passing Detection for OTFS

Message Passing (MP) detection represents a low-complexity alternative to traditional techniques such as LMMSE or single-tap equalization for Orthogonal Time Frequency Space (OTFS) modulation. While LMMSE offers good performance in doubly selective channels, it comes at high computational cost. MP detection, by contrast, leverages the sparsity of the delay-Doppler domain to iteratively estimate transmitted symbols with significantly lower complexity.

4.14.1 MP Detection Algorithm

The MP algorithm models the delay-Doppler domain input-output relationship as a factor graph, where each variable node corresponds to a transmitted symbol and each observation node corresponds to a received signal sample. The detection problem is reformulated as a probabilistic inference task, where the goal is to compute the most likely transmitted symbols based on the received vector and the channel matrix.
Let $\mathbf{y}, \mathbf{z} \in \mathbb{C}^{NM \times 1}$ be the received signal and noise vectors, and let $\mathbf{H} \in \mathbb{C}^{NM \times NM}$ represent the delay-Doppler channel matrix. The transmitted symbols $\mathbf{x} \in \mathbb{C}^{NM \times 1}$ take values from a modulation alphabet $\mathcal{A} = \{a_1, \ldots, a_Q\}$.
The MP algorithm approximates the symbol-by-symbol maximum a posteriori (MAP) detection by exchanging messages between observation and variable nodes. Each message consists of the mean and variance of the interference, modeled as Gaussian noise due to the sparse structure of $\mathbf{H}$. The core idea is to iteratively update the posterior probabilities of the transmitted symbols based on these messages.

4.14.2 Algorithm Steps

1. **Initialization:** All symbol probabilities are initialized uniformly across the modulation alphabet.

2. **Message Passing:** At each iteration

   - Observation nodes compute the mean and variance of the interference for each connected variable node, excluding the symbol being updated. These statistics are passed to variable nodes.

   - Variable nodes update the symbol probabilities using the received messages from observation nodes.

3. **Decision Update:** Symbol decisions are updated based on the maximum a posteriori probability.

4. **Stopping Criterion:** The algorithm checks for convergence using a suitable indicator. If convergence is reached or a maximum number of iterations is met, the algorithm terminates.

This iterative process exploits the sparsity of the delay-Doppler channel matrix, allowing the complexity of detection to scale linearly with the number of symbols, making it suitable for large-scale OTFS systems.

4.15 Maximum-Ratio Combining Detection in OTFS

In Orthogonal Time Frequency Space (OTFS) systems, the signal received over a multipath fading channel undergoes various delays and Doppler shifts. These components can be viewed analogously to the delayed echoes processed by a rake receiver in CDMA systems. Maximum-Ratio Combining (MRC) detection is a low-complexity technique that capitalizes on this structure by coherently combining the signal energy spread across multiple delay branches, enhancing the signal-to-noise ratio (SNR) of the received symbols.

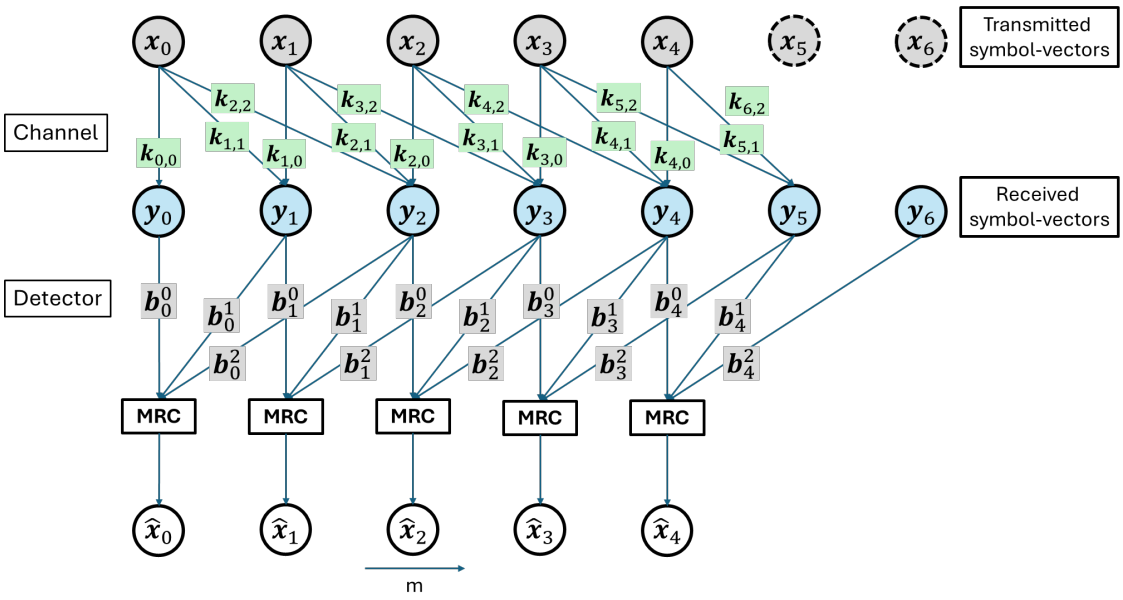

Figure 4.13: MRC delay-Doppler domain operation for M'=7, M=5, and the set of discrete delay indices $\mathcal{L} = [0,1,2]$. Reproduced by the author after [7].

4.15.1 Overview of MRC in Delay-Doppler Domain

MRC in the delay-Doppler domain works by identifying and coherently summing the delayed contributions of each transmitted symbol. These delayed components are extracted using matched filtering, which aligns with the known channel characteristics (delays and gains). This technique is optimal under additive white Gaussian noise (AWGN) conditions and remains effective in correlated noise environments when proper weighting is applied.
The implementation involves the following steps:

1. **System Model and Preliminaries:**

   Consider an OTFS frame padded with zero prefixes (ZP) to accommodate the maximum expected delay spread. The frame size is extended accordingly. The received signal vector $\mathbf{y}$ includes the effect of the zero-padding, and the relation between the transmitted symbols $\mathbf{x}$ and the received symbols $\mathbf{y}$ is given by:

   $$\mathbf{y}_{m'} = \sum_{l' \in \mathcal{L}} \mathbf{K}_{m',l'} \cdot \mathbf{x}_{m'-l'} + \mathbf{z}_{m'} \tag{4.82}$$

   where:

   - $\mathcal{L}$ is the set of discrete delay indices,
   - $\mathbf{K}_{m',l'}$ are channel submatrices for each delay branch,
   - $\mathbf{z}_{m'}$ is the additive noise.

2. **Interference Cancellation:**

   For each delay branch l, the method computes a partial signal $\mathbf{b}_m^l$ for symbol index m, subtracting the estimated interference from other branches:

$$\mathbf{b}_m^l = \mathbf{y}_{m+l} - \sum_{\substack{l' \in \mathcal{L} \\ l' \neq l}} \mathbf{K}_{m+l,l'} \cdot \hat{\mathbf{x}}_{m+l-l'} \tag{4.83}$$

   where $\hat{x}$ denotes the current estimate of the transmitted symbols from previous iterations.

3. **Maximum-Ratio Combining:**

   The MRC combines the partial estimates $\mathbf{b}_m^l$ using:

$$\mathbf{D}_m = \sum_{l \in \mathcal{L}} \mathbf{K}_{m+l,l}^{\dagger} \mathbf{K}_{m+l,l}, \tag{4.84}$$

$$\mathbf{g}_m = \sum_{l \in \mathcal{L}} \mathbf{K}_{m+l,l}^{\dagger} \mathbf{b}_m^l, \tag{4.85}$$

   to produce the combined output:

$$\mathbf{c}_m = \mathbf{D}_m^{-1} \mathbf{g}_m, \tag{4.86}$$

   where $\mathbf{c}_m \in \mathbb{C}^{N \times 1}$ is the combined vector for symbol index m.

4. **Symbol Detection:**

   The final symbol estimates are obtained through maximum likelihood detection:

$$\hat{\mathbf{x}}_m[n] = \arg\min_{a_j \in \mathcal{Q}} |a_j - c_m[n]|, \tag{4.87}$$

   where $\mathcal{Q}$ is the QAM alphabet, and a_j are its constellation points.

5. **Iterative Refinement (Optional):**

   This process can be repeated iteratively to refine symbol estimates. In each iteration, updated symbol estimates are used to recalculate the interference, progressively improving the signal-to-interference-plus-noise ratio (SINR).

4.15.2 Advantages

- **Lower Complexity:** Compared to maximum likelihood or message passing detection, MRC offers a favorable trade-off between complexity and performance.
- **Scalability:** The method scales efficiently with frame size and delay spread.
- **Practicality:** MRC principles align with existing technologies like CDMA rake receivers, simplifying implementation.

4.15.3 Limitations and Practical Considerations

- **Noise Correlation Sensitivity:** MRC assumes uncorrelated noise across delay branches. In scenarios with correlated noise or strong interference, the performance may degrade unless additional preprocessing (e.g., whitening) is applied.
- **Iterative Convergence:** The convergence speed depends on initial symbol estimates. Poor initial estimates can lead to slower convergence.
- **Channel Estimation Errors:** Accurate knowledge of $\mathbf{K}_{m',l'}$ is critical. Estimation errors degrade performance.

4.15.4 Comparison with Other Detection Methods

- **LMMSE:** Better for correlated noise but requires matrix inversions (higher complexity).
- **Message Passing:** Near-optimal but computationally intensive for large frames.
- **Low-Complexity Approximations:** May sacrifice accuracy for speed.

4.16 Iterative Rake Turbo Decoding for OTFS Systems

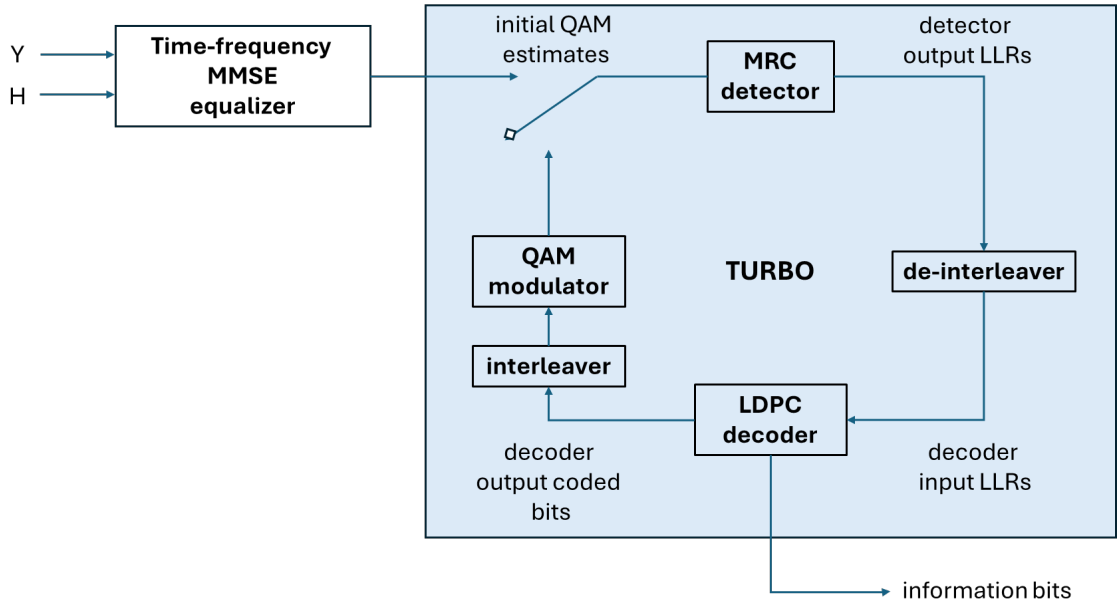

Figure 4.14: OTFS iterative rake turbo decoder operation. Reproduced by the author after [7].

4.16.1 System Architecture

The iterative rake turbo decoder represents an advanced receiver architecture for coded OTFS systems, combining maximum-ratio combining (MRC) detection with channel decoding in a feedback loop. As shown in Figure 4.14, the system employs:

- An LDPC encoder and random interleaver at the transmitter
- QAM symbol mapping and OTFS modulation
- A receiver with iterative processing between:
  - MRC-based symbol detection
  - LDPC decoding
  - Interleaving/deinterleaving stages

4.16.2 Iterative Processing Mechanism

The detection-decoding process operates through the following stages:

1. **Initial Estimation:** The receiver begins with coarse symbol estimates from a single-tap MMSE equalizer.
2. **MRC Detection:** The MRC stage processes these estimates, accounting for multipath effects through:
$$c_m^{(i)} = x_m + e_m^{(i)} \tag{4.88}$$
where $e_m^{(i)}$ represents the normalized post-MRC noise-plus-interference (NPI) vector in iteration i.
3. **LLR Computation:** The detector calculates bit-level log-likelihood ratios (LLRs) using:
$$L_{m,n,b}^{(i)} = \log \frac{\sum_{a \in A_{b=0}} e^{-\gamma_a}}{\sum_{a' \in A_{b=1}} e^{-\gamma_{a'}}}, \quad \gamma_a = \frac{|c_m^{(i)}[n] - a|^2}{(\sigma_m^{(i)})^2} \tag{4.89}$$
where $A_{b=0}$ and $A_{b=1}$ denote QAM constellation subsets.
4. **Channel Decoding:** After deinterleaving, the LDPC decoder produces hard decisions that are re-encoded, interleaved, and remodulated for feedback.

4.16.3 Key Technical Aspects

Noise Variance Estimation

The receiver tracks the evolving NPI characteristics through:

$$(\sigma_m^{(i)})^2 \approx \frac{1}{N} \sum_{l \in \mathcal{L}} \eta_{m,l} \mathrm{tr}(\mathbf{C}_{m+l}^{(i)}) \tag{4.90}$$

where $\mathbf{C}_m^{(i)}$ represents the covariance matrix of the residual error vector.

For a more detailed discussion about all the techniques and their complexity refer to [7, Chapter 6]

Chapter 5

OFDM Simulation Framework

This chapter presents a detailed framework for simulating OFDM performance in multi-path fading channels with Doppler effects. Pilot-assisted channel estimation is used, and system performance is evaluated in terms of bit error rate (BER) for various SNR values.

5.1 System Parameters

The OFDM system is configured with the parameters summarized in Table 5.1.

Parameter	**Value**
Number of subcarriers, M	64
Number of OFDM symbols per frame, N	30
Subcarrier spacing, Δf	15 kHz
Carrier frequency, f_c	5 GHz
Cyclic prefix length, L_{CP}	15 samples
Modulation	QPSK (4-PSK)
Pilot spacing	3 symbols
SNR range	0:5:40 dB

Table 5.1: OFDM System Parameters

The sampling frequency is

$$f_s = M \cdot \Delta f, \tag{5.1}$$

the total number of samples per OFDM symbol including cyclic prefix is

$$M_{\text{eff}} = M + L_{\text{CP}}, \tag{5.2}$$

and the OFDM symbol duration is

$$T_s = \frac{M + L_{\text{CP}}}{M \Delta f}. \tag{5.3}$$

5.2 OFDM Signal Generation

The frequency-domain OFDM symbol matrix is $X \in \mathbb{C}^{M \times N}$, with columns representing OFDM symbols and rows representing subcarriers. Each symbol is modulated using QPSK (4-PSK), mapping 2 bits per subcarrier.
The time-domain OFDM symbol for symbol n is obtained via inverse discrete Fourier transform (IDFT):

$$s_n[m] = \frac{1}{\sqrt{M}} \sum_{k=0}^{M-1} X[k,n]\, e^{j2\pi km/M}, \quad m = 0,1,\ldots,M-1. \tag{5.4}$$

Cyclic prefix of length L_{CP} is prepended:

$$s_n^{\mathrm{CP}}[m] = \begin{cases} s_n[m+M-L_{\mathrm{CP}}], & 0 \le m < L_{\mathrm{CP}} \\ s_n[m-L_{\mathrm{CP}}], & L_{\mathrm{CP}} \le m < M+L_{\mathrm{CP}} \end{cases}. \tag{5.5}$$

The transmitted OFDM frame is the concatenation of all OFDM symbols:

$$s[n] = [s_1^{\mathrm{CP}}, s_2^{\mathrm{CP}}, \ldots, s_N^{\mathrm{CP}}]. \tag{5.6}$$

5.3 Pilot Configuration

Pilot symbols are inserted periodically with spacing x:

$$\mathcal{P} = \{1, x+1, 2x+1, \ldots, N\}, \quad \mathcal{D} = \{1,\ldots,N\} \setminus \mathcal{P}. \tag{5.7}$$

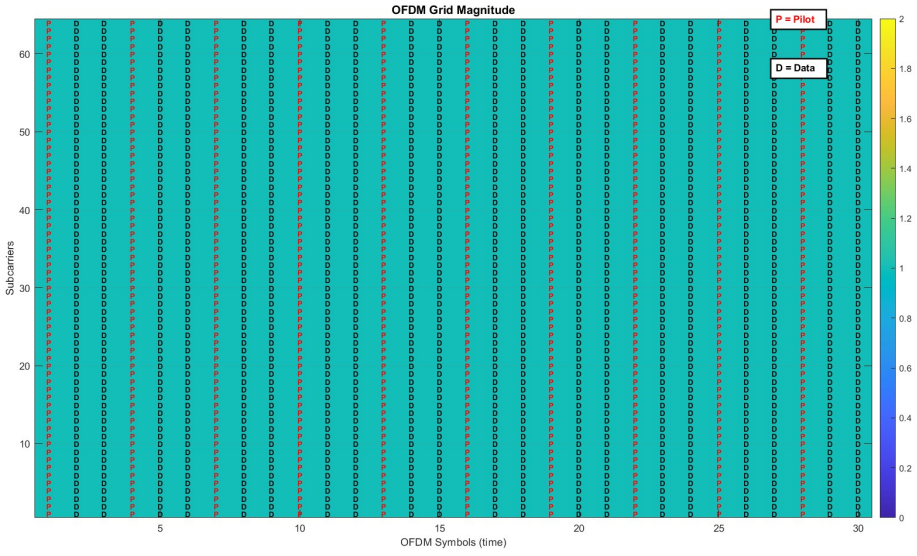

Figure 5.1: OFDM time-frequency grid showing pilot and data symbol allocation.

5.4 Multipath Fading with Doppler Channel

The transmitted signal propagates through a multipath fading channel with Doppler shifts. The channel consists of L discrete paths, each with delay τ_l, Doppler frequency ν_l, and complex gain g_l.
The received signal is

$$r[n] = \sum_{l=1}^{L} g_l \, s[n - \tau_l] \, e^{j2\pi\nu_l n/f_s} + w[n], \tag{5.8}$$

where $w[n]$ is additive white Gaussian noise.
Doppler shifts introduce time-varying phase rotations:

$$s_l[n] = s[n]e^{j2\pi\nu_l n/f_s}. \tag{5.9}$$

Each path is delayed and scaled by its gain:

$$s_l^{\text{delayed}}[n] = g_l s_l[n - \tau_l]. \tag{5.10}$$

The received signal is the superposition of all paths:

$$r[n] = \sum_{l=1}^{L} s_l^{\text{delayed}}[n] + w[n]. \tag{5.11}$$

Path	**Delay [μs]**	**Doppler shift [Hz]**	**Gain**
1	0.84	0	5.0
2	2.53	-1215	2.0
3	3.38	3443	0.7

Table 5.2: Channel Parameters

5.5 OFDM Reception and Channel Estimation

After removing the cyclic prefix, the DFT is applied to obtain frequency-domain symbols:

$$Y[k,n] = \frac{1}{\sqrt{M}} \sum_{m=0}^{M-1} r_n[m] e^{-j2\pi km/M}. \tag{5.12}$$

LMMSE estimation on pilot symbols is performed:

$$\hat{H}[k,p] = \frac{Y[k,p]X^*[k,p]}{|X[k,p]|^2 + \sigma_w^2}, \quad p \in \mathcal{P}. \tag{5.13}$$

Channel estimates for data symbols are obtained via linear interpolation:

$$\hat{H}[k,n] = \text{interp1}(\mathcal{P}, \hat{H}[k,\mathcal{P}], n), \quad n \in \mathcal{D}. \tag{5.14}$$

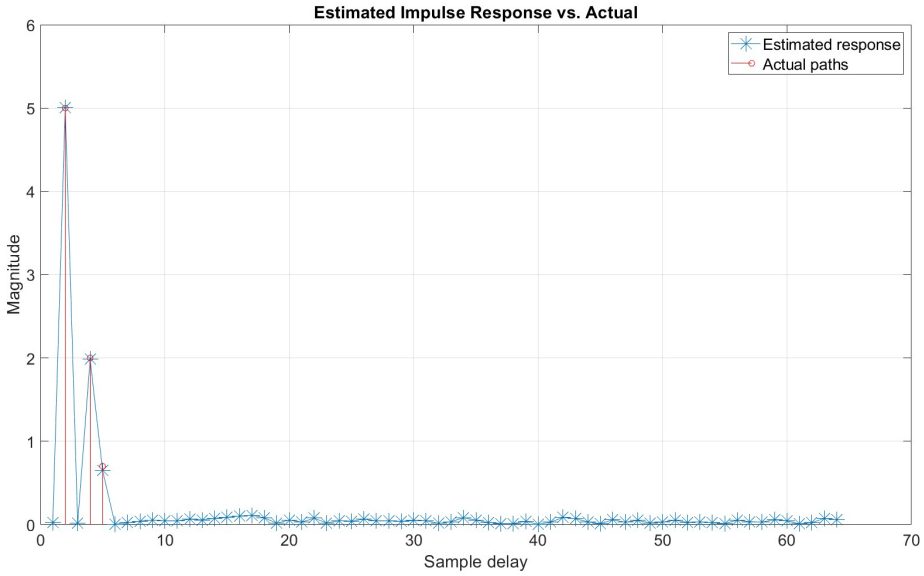

Figure 5.2: Estimated channel magnitude for all subcarriers across OFDM symbols using pilot-assisted LMMSE.

5.6 Equalization and Detection

Single-tap frequency-domain equalization is applied:

$$\hat{X}[k,n] = \frac{Y[k,n]\hat{H}^*[k,n]}{|\hat{H}[k,n]|^2 + \sigma_w^2}. \tag{5.15}$$

Detected bits are recovered via QPSK demodulation:

$$\hat{b}_k[n] = \text{QPSKDemod}(\hat{X}[k,n]), \tag{5.16}$$

where 2 bits per subcarrier are recovered according to the standard Gray mapping.

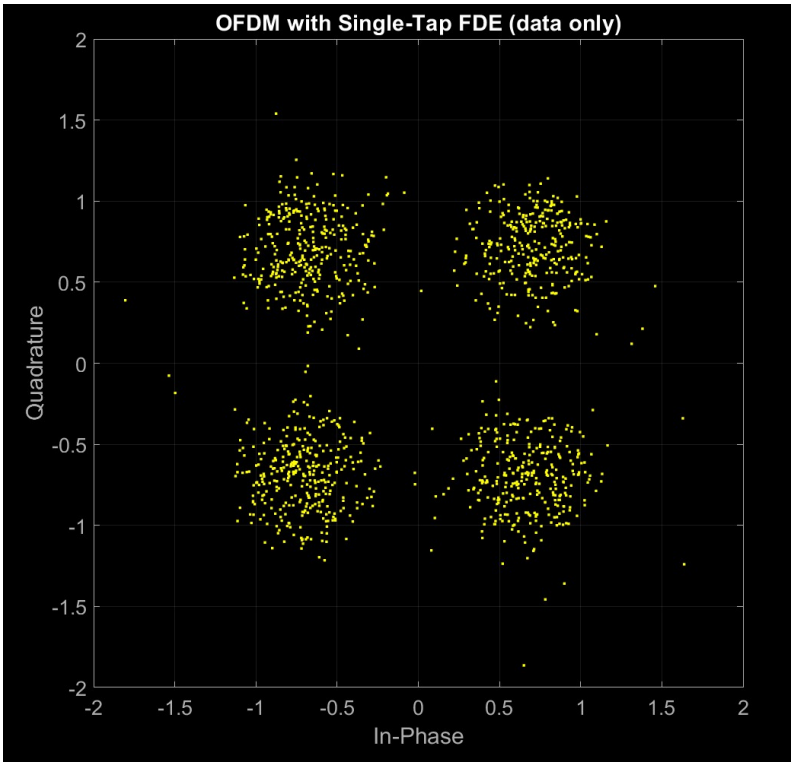

Figure 5.3: Scatter plot of received QPSK symbols after single-tap equalization.

5.7 Performance Metrics

Bit error rate (BER) is calculated as

$$\text{BER} = \frac{\sum_{n,k} \mathbf{1}\{b_k[n] \neq \hat{b}_k[n]\}}{\text{Total number of transmitted bits}}. \tag{5.17}$$

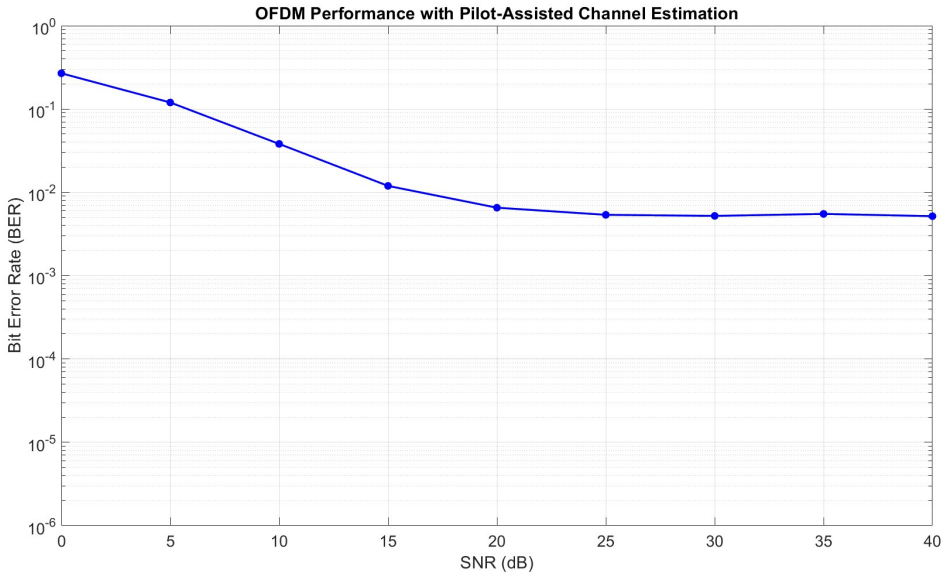

Figure 5.4: BER performance of the OFDM system with pilot-assisted channel estimation over a multipath fading channel.

Chapter 6

OTFS Simulation Framework

This chapter presents the simulation framework for OTFS (Orthogonal Time-Frequency Space) modulation over a multipath fading channel with Doppler effects. Pilot-assisted channel estimation and LMMSE equalization in the delay-Doppler domain are employed to recover transmitted data.

6.1 System Parameters

The OTFS system is configured with parameters summarized in Table 6.1.

Parameter	**Value**
Number of delay bins (rows), M	64
Number of Doppler bins (columns), N	30
Subcarrier spacing, Δf	15 kHz
Carrier frequency, f_c	5 GHz
Zero-padding length	15 samples
Modulation	QPSK (4-PSK)
Central pilot position (m_p, n_p)	$(M/2, N/2)$
SNR range	0:5:40 dB

Table 6.1: OTFS System Parameters

The sampling frequency is

$$f_s = M \cdot \Delta f, \tag{6.1}$$

the total number of samples per OTFS symbol including zero-padding is

$$M_{\text{eff}} = M + \text{padLen}, \tag{6.2}$$

and the OTFS symbol duration is

$$T_s = \frac{M_{\text{eff}}}{f_s}. \tag{6.3}$$

6.2 Delay-Doppler Grid and Symbol Mapping

OTFS maps information symbols onto the delay-Doppler grid $X \in \mathbb{C}^{M \times N}$:

- $X(m, n)$: transmitted symbol at delay bin m and Doppler bin n
- Central pilot inserted at (m_p, n_p)
- Guard symbols inserted around pilot to mitigate ISI
- Data symbols occupy remaining grid positions

The time-domain signal is obtained via the ISFFT:

$$s[n] = \text{vec}\left(\text{IFFT}\left(X^{\top}\right)\right), \quad n = 1, \ldots, M_{\text{eff}} \cdot N \tag{6.4}$$

and serialized for transmission.

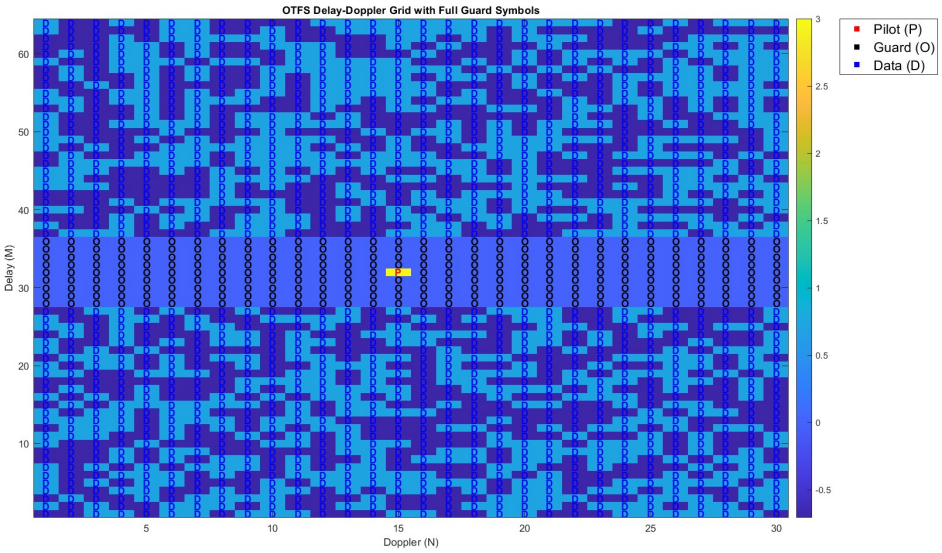

Figure 6.1: OTFS delay-Doppler grid with pilot, guard, and data symbols.

6.3 Channel Model

The multipath fading channel has L paths, each characterized by a delay τ_l, a Doppler shift ν_l, and a complex gain g_l. The received signal is

$$r[n] = \sum_{l=1}^{L} g_l \, s[n - \tau_l] \, e^{j2\pi\nu_l n / f_s} + w[n], \tag{6.5}$$

where $w[n]$ is additive white Gaussian noise. Doppler shifts induce time-varying phase rotations:

$$s_l[n] = s[n]\, e^{j2\pi\nu_l n/f_s}. \tag{6.6}$$

Each path is delayed and scaled:

$$s_l^{\text{delayed}}[n] = g_l\, s_l[n - \tau_l]. \tag{6.7}$$

The output signal is the superposition of all paths:

$$r[n] = \sum_{l=1}^{L} s_l^{\text{delayed}}[n] + w[n]. \tag{6.8}$$

Path	**Delay [μs]**	**Doppler shift [Hz]**	**Gain**
1	0.84	0	5.0
2	2.53	-1215	2.0
3	3.38	3443	0.7

Table 6.2: Channel Parameters

6.4 Receiver and Delay-Doppler Channel Estimation

After reception and reshaping, the received grid is transformed to the **delay-Doppler domain** via FFT:

$$Y_{\text{DD}} = \text{FFT}(\text{reshape}(r[n], M_{\text{eff}}, N))^{\top} \cdot M \tag{6.9}$$

Using the known pilot, the local channel response is estimated:

$$g_{\text{est}}(l,k) = \frac{Y_{\text{DD}}(m_p + l, n_p + k)}{x_p\, z^{k m_p}}, \quad z = e^{j2\pi/N} \tag{6.10}$$

Thresholding identifies significant paths:

$$b(l,k) = \begin{cases} 1, & |g_{\text{est}}(l,k)| > \text{threshold} \\ 0, & \text{otherwise} \end{cases} \tag{6.11}$$

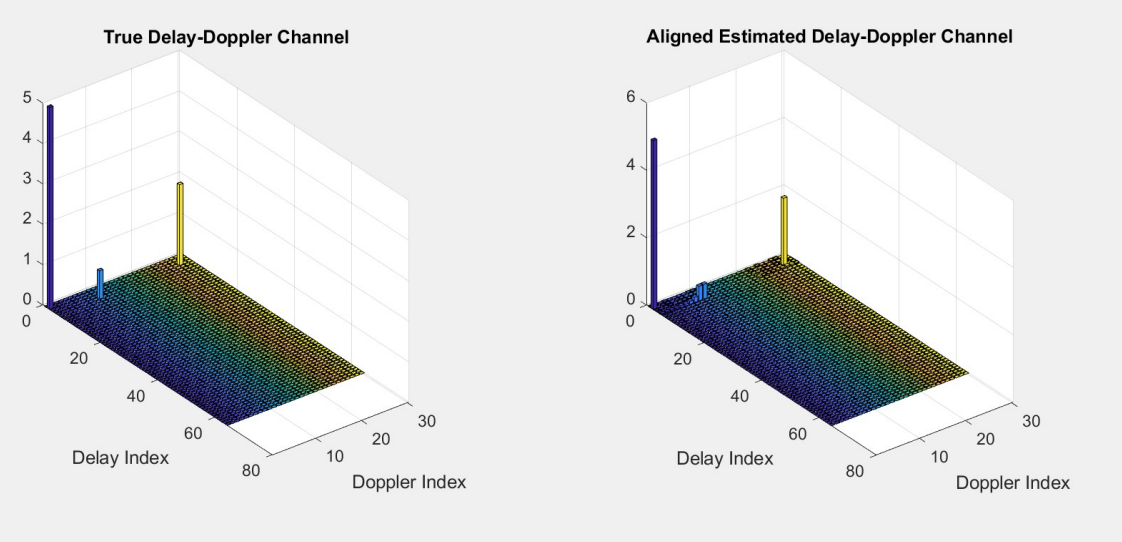

Figure 6.2: Estimated delay-Doppler channel magnitude.

6.5 Construction of the Time-Domain Channel Matrix G

To perform LMMSE equalization, the **time-domain channel matrix** G is constructed from the estimated delay-Doppler paths:

- Each path with delay τ_l and Doppler index ν_l contributes a shifted complex sinusoid across the transmitted vector.
- The total transmitted signal length is $M_{\text{eff}} \cdot N$.
- The contribution of each path forms diagonals in G, offset by the path delay.

Mathematically, the elements of G are

$$G = \sum_{l=0}^{L-1} \text{diag}\Big(g_l \, e^{j2\pi\nu_l n/(M_{\text{eff}}N)}, -\tau_l\Big), \tag{6.12}$$

where each $\text{diag}(\cdot, -\tau_l)$ shifts the path by its delay along the diagonal. This matrix fully represents the channel in the time domain and is used in LMMSE equalization.

6.6 Data Detection and Equalization

LMMSE equalization is applied using the channel matrix G:

$$\hat{x} = (G^H G + \sigma_n^2 I)^{-1} G^H r \tag{6.13}$$

Detected symbols are reshaped into the delay-Doppler grid, and only data symbols are considered for BER calculation.

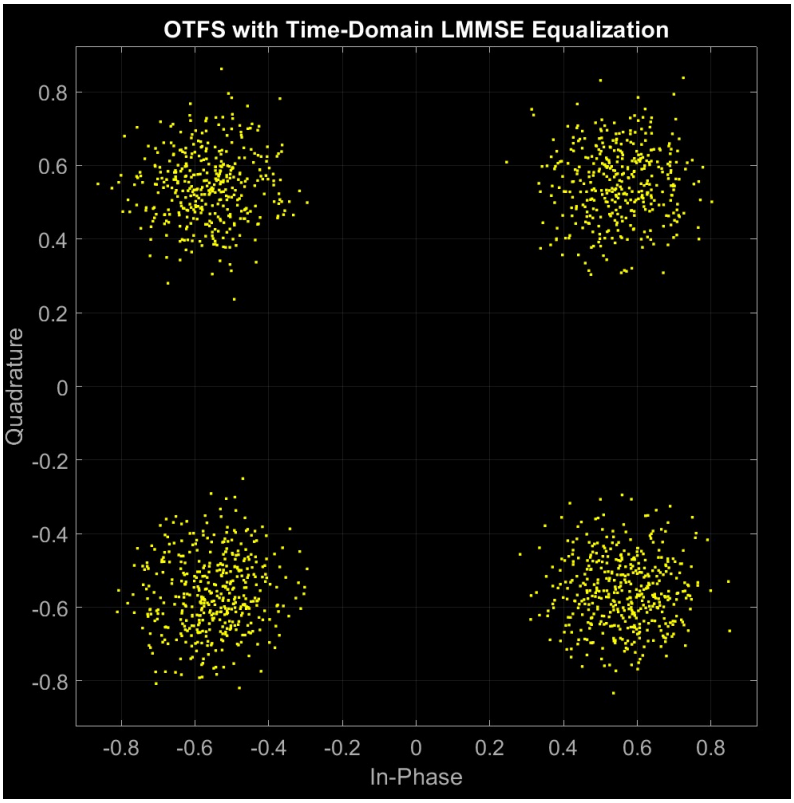

Figure 6.3: Scatter plot of received OTFS data symbols after time-domain LMMSE equalization.

6.7 Performance Metrics

The bit error rate (BER) is computed as:

$$\text{BER} = \frac{\text{Number of erroneous bits}}{\text{Total transmitted bits}} \tag{6.14}$$

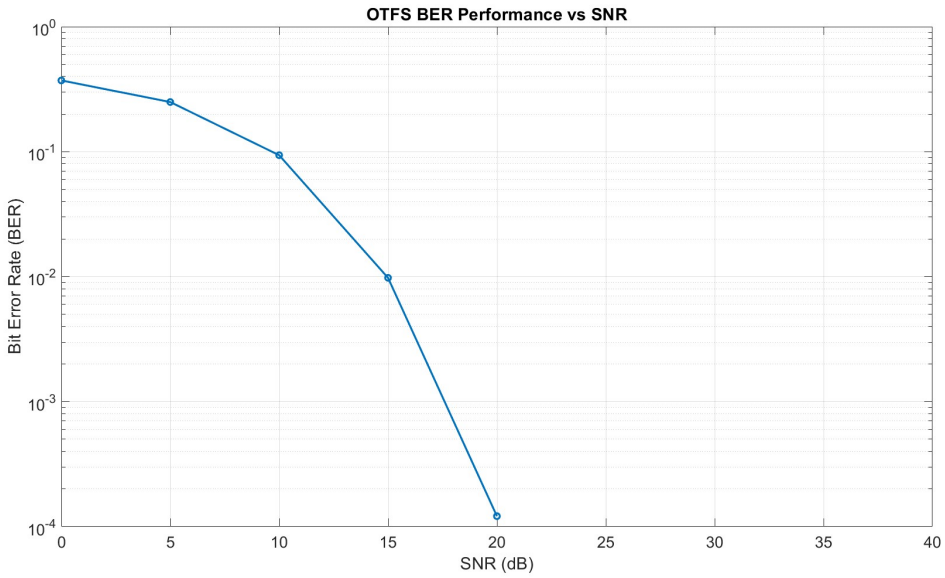

Figure 6.4: OTFS BER performance versus SNR.

6.8 ZP-OTFS: Zero-Padded OTFS Transmission

In this work, the Zero-Padded OTFS (ZP-OTFS) scheme has been adopted. In this approach a zero padding is applied after each time-domain OTFS symbol instead of using a cyclic prefix. This technique preserves the linearity of the channel convolution without introducing artificial periodicity, as done in traditional CP-OTFS systems. The modulation process consists of two key steps: a 2D inverse symplectic finite Fourier transform (ISFFT) followed by multicarrier modulation.
Let $\mathbf{X}_{\mathrm{DD}} \in \mathbb{C}^{M\times N}$ be the data matrix in the delay-Doppler domain, where M is the number of subcarriers and N is the number of OTFS symbols. The time-frequency domain signal $\mathbf{X}_{\mathrm{TF}} \in \mathbb{C}^{M\times N}$ is obtained via ISFFT:

$$\mathbf{X}_{\mathrm{TF}} = \mathbf{F}_M \cdot \mathbf{X}_{\mathrm{DD}} \cdot \mathbf{F}_N^{\mathrm{H}} \tag{6.15}$$

where $\mathbf{F}_M$ and $\mathbf{F}_N$ are the normalized DFT matrices of size $M \times M$ and $N \times N$, respectively. Then, each column of $\mathbf{X}_{\mathrm{TF}}$ is transformed to the time domain via an M-point IFFT:

$$\mathbf{s}_n = \mathrm{IFFT}\left(\mathbf{X}_{\mathrm{TF}}(:, n)\right), \quad n = 0, \ldots, N-1 \tag{6.16}$$

To construct the ZP-OTFS time-domain transmit signal, a zero-padding of length L samples is appended to each symbol:

$$\tilde{\mathbf{s}}_n = \begin{bmatrix} \mathbf{s}_n \\ \mathbf{0}_{L\times 1} \end{bmatrix} \tag{6.17}$$

The overall transmit signal $\mathbf{s}_{\mathrm{ZP}}$ is then:

$$\mathbf{s}_{\mathrm{ZP}} = \begin{bmatrix} \tilde{\mathbf{s}}_0^\top & \tilde{\mathbf{s}}_1^\top & \cdots & \tilde{\mathbf{s}}_{N-1}^\top \end{bmatrix}^\top \tag{6.18}$$

At the receiver, the inverse operations are applied. After segmentation and removal of the zero-padding, FFT is applied to recover the time-frequency samples, followed by the SFFT (symplectic FFT) to recover the delay-Doppler domain data:

$$\hat{\mathbf{X}}_{\mathrm{DD}} = \mathbf{F}_M^{\mathrm{H}} \cdot \mathbf{X}_{\mathrm{TF,rx}} \cdot \mathbf{F}_N \tag{6.19}$$

ZP-OTFS is advantageous in scenarios where the strict cyclicity required by CP may degrade system performance, or when a strictly linear channel convolution model is desired. However, it requires more sophisticated equalization schemes, as the circulant channel model no longer holds.

6.9 BER vs SNR Simulation Analysis of OFDM and OTFS

This section presents a comparative evaluation of OFDM and OTFS performance over the same multipath fading channel. The focus is on bit error rate (BER) versus signal-to-noise ratio (SNR), highlighting the advantages of each modulation scheme under Doppler effects.

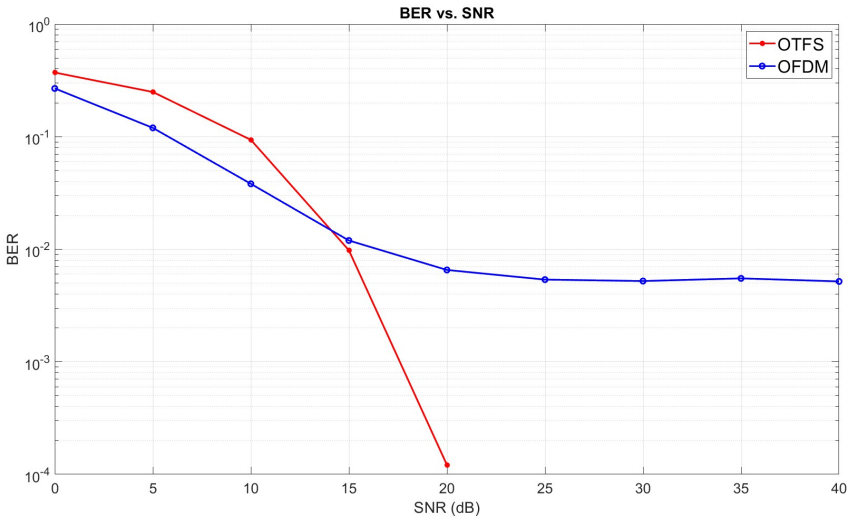

Figure 6.5: Comparison of BER performance between OFDM and OTFS over a multipath fading channel with Doppler.

6.10 Observations and Discussion

From the simulation results, the following observations can be made:

- **Channel Estimation:** Both OFDM and OTFS are able to correctly estimate the three dominant paths of the multipath channel. Minor noise is visible in the estimated channel magnitude plots (Figures 5.2 and 6.2), but the main channel components are accurately captured, enabling reliable equalization.
- **Detection Performance:** The scatter plots of received symbols after equalization (Figures 5.3 and 6.3) show that both modulations achieve good symbol recovery. Symbols are well clustered around their ideal constellation points, indicating effective compensation for multipath and Doppler effects.
- **BER Performance:** The BER curves in Figure 6.5 show that at low SNRs, both OFDM and OTFS exhibit similar error rates. As the SNR increases, OTFS demonstrates a clear advantage in high-Doppler scenarios, maintaining lower BER than OFDM. This highlights OTFS's robustness to time-varying channels, while OFDM performance is slightly degraded due to inter-carrier interference under Doppler spread.

Overall, both modulation schemes perform reliably in terms of channel estimation and symbol detection. However, OTFS provides superior BER performance in fast-fading channels, making it better suited for high-mobility scenarios.

Chapter 7

Comparative Analysis of OFDM and OTFS

7.1 Experimental Setup and Methodology

To perform the experiments, the following steps were necessary. For each modulation scheme, a transmitter (TX) file was created to generate a signal composed of:

- **Preamble:** selected from the 3GPP standard due to its excellent correlation properties.
- **Guard Interval (GuardLen)**
- **Data Payload**
- **Guard Interval (GuardLen)**

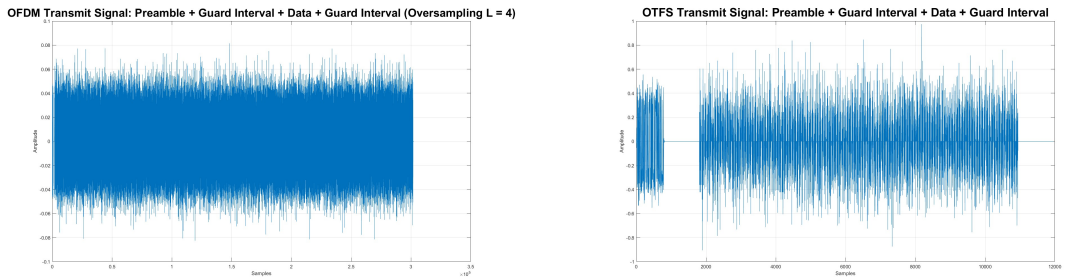

(a) OFDM transmit signal.

(b) OTFS transmit signal.

Figure 7.1: Comparison between OFDM (oversampling $L = 4$) and OTFS transmit signals (time-domain representation).

This signal was transmitted using the USRP for 1 second. A receiver (RX) file was then implemented to perform frame synchronization through correlation with the preamble, allowing post-processing to estimate the channel and perform data detection.

7.1.1 Importance of the Preamble choice

The preamble, a reference sequence or set of known symbols inserted periodically within a data transmission, plays a crucial role in ensuring the reliability and efficiency of communication systems. Its proper design and selection significantly impact various aspects of the transmission process.

First and foremost, the preamble enables accurate **channel estimation**, which is critical for mitigating the effects of channel impairments such as attenuation, delay, and distortion. A well-designed preamble allows precise estimation of channel characteristics, ensuring effective equalization and minimizing errors in data decoding. Conversely, an improperly chosen preamble can lead to inaccurate channel estimates, resulting in degraded performance.

In addition, the preamble facilitates **synchronization** between the transmitter and receiver. It provides a clear temporal reference point, ensuring that the receiver can correctly align with the transmitted data. Using distinctive sequences for the preamble reduces the risk of synchronization errors, which could otherwise lead to data loss or misinterpretation.

Another key benefit of a well-designed preamble is its robustness against **noise and interference**. Sequences with optimal autocorrelation properties, such as Zadoff-Chu sequences, help distinguish the preamble from background noise and interference, enhancing signal detectability even in challenging environments. Poorly designed preambles with suboptimal correlation properties, however, can struggle to perform this function effectively.

The preamble also affects the **spectral efficiency** of the system. Since it occupies bandwidth, the frequency and length of preamble insertions must be carefully balanced to maximize the transmission of useful data while maintaining system reliability. Excessively frequent or lengthy preambles can reduce data throughput, while too sparse or short preambles may compromise signal integrity.

Finally, in environments with **multi-path fading** or dispersive channels, the preamble assists in combating distortion by enabling effective compensation. Sequences that are spatially and spectrally well-distributed are better suited to handle these challenges, improving signal resilience.

For this thesis project, the following preamble has been chosen, as described in the document by 3rd Generation Partnership Project (3GPP) [3], Basic Midamble Codes for Burst Type 2.
This sequence was selected due to its excellent correlation properties, making it highly suitable for ensuring reliable channel estimation and synchronization in our system:

```
5D253744435A24EF0ECC21F43AA5B8144FBDB348C746080C
```

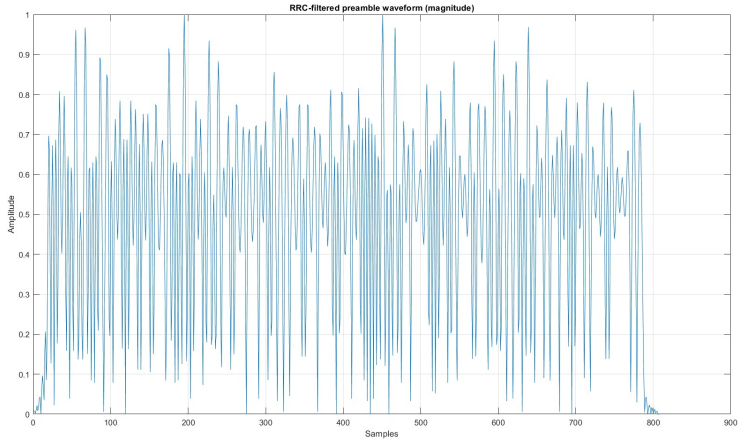

(a) RRC-filtered preamble waveform (oversampling $L = 4$).

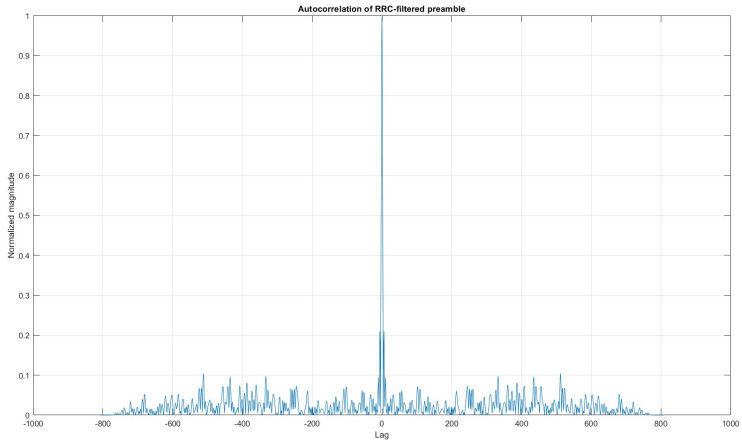

(b) Normalized autocorrelation of the preamble.

Figure 7.2: Preamble waveform and its autocorrelation. The 3GPP-based preamble was chosen due to its excellent correlation properties.

In summary, the choice of a proper preamble is a pivotal aspect of data transmission system design. It directly influences channel estimation, synchronization, noise resilience, spectral efficiency, and system compatibility. A carefully designed preamble ensures robust, efficient, and reliable communication, making it an essential component of any modern communication system.

Note on Frame Synchronization and CFO Correction Figures. The figures illustrating the concepts of frame synchronization and the effects of carrier frequency offset (CFO) estimation and correction are shown once for clarity and conceptual understanding. These examples specifically refer to the transmission performed with the coaxial

cable setup (OFDM modulation), which provides a clean and controlled reference scenario without the additional impairments introduced by wireless propagation. The same procedures for frame synchronization and CFO correction are then consistently applied across all subsequent experimental configurations.

7.1.2 Frame synchronization

Frame synchronization is a crucial step in signal processing to accurately align received signal frames. The following procedure describes the synchronization process:

To determine the starting point of the Rx sequence, a correlation operation has been performed between the selected preamble and received signal vector. The correlation function highlights areas of high similarity between the preamble and the received signal, enabling precise detection of synchronization points.

Finally, the peak in the correlation result has been located. This peak represents the point of maximum alignment between the preamble and the received signal, thus allowing to accurately recover the starting point of the Rx sequence.

This synchronization method ensures precise frame alignment, improving the reliability of further signal processing operations.

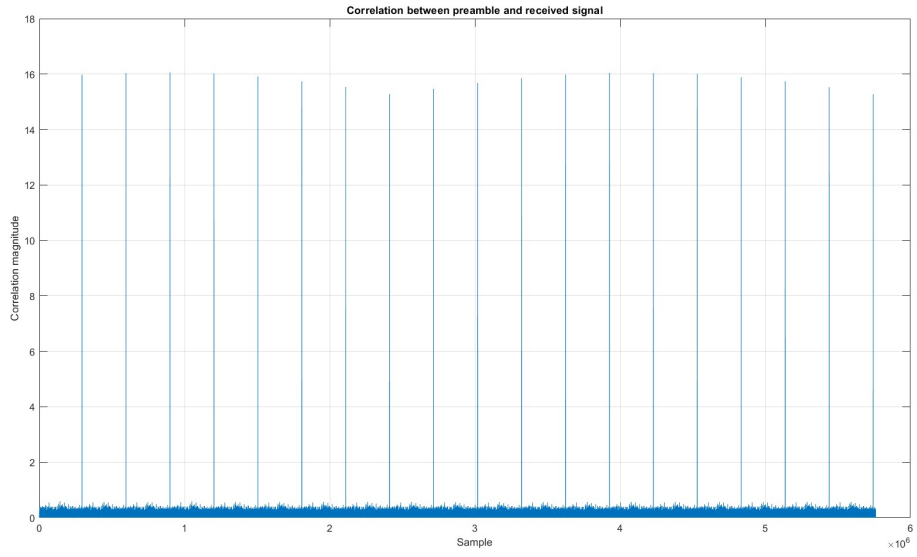

Figure 7.3: Correlation between preamble and received signal. The x-axis represents the sample index, and the y-axis shows the correlation magnitude.

7.1.3 Frequency recovery

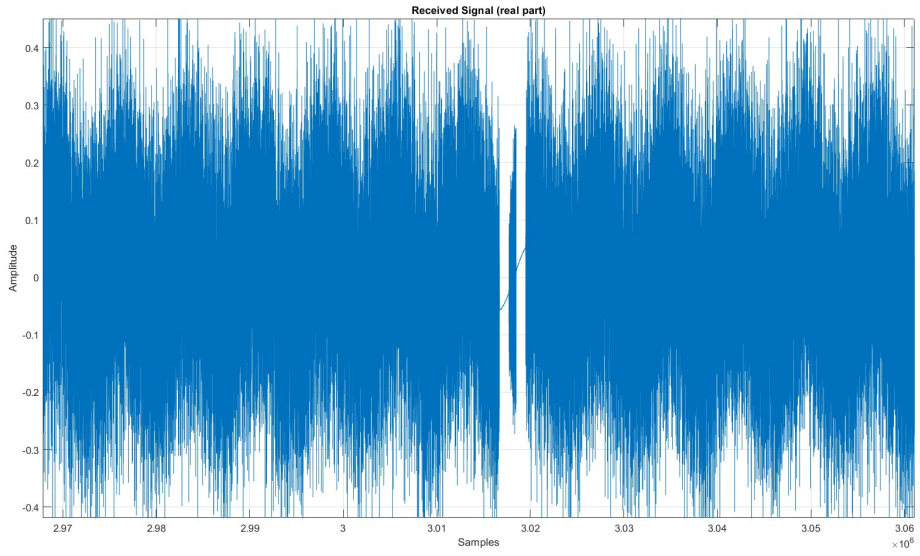

(a) Received signal (ZOOM, real part) before CFO correction.

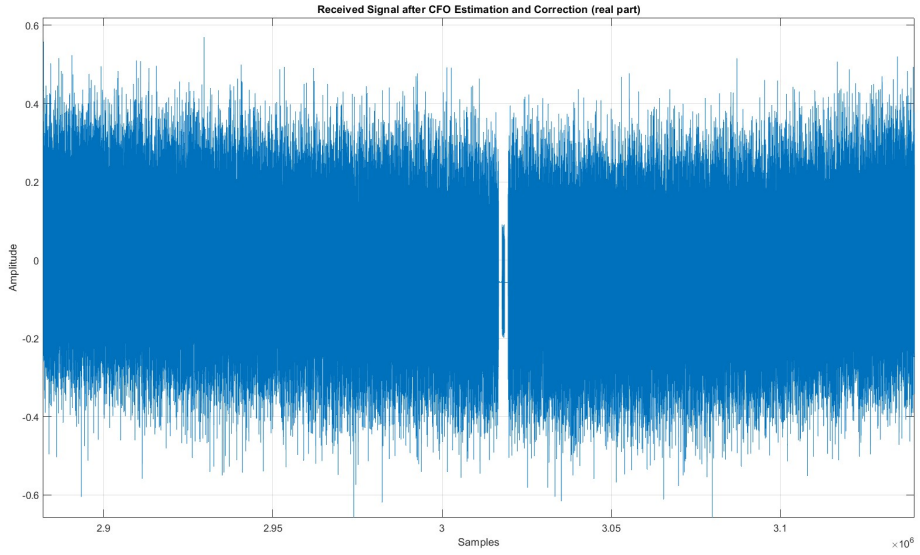

(b) Received signal (ZOOM, real part) after CFO estimation and correction.

Figure 7.4: Comparison of the received signal before and after carrier frequency offset (CFO) correction. The example refers to transmission using the coaxial cable setup.

The figure 7.4a shows a received signal with evident periodicity, which is likely due to the **lack of frequency recovery** in the synchronization process.

In a communication system, the transmitted and received signals should ideally have the same frequency. However, in practical scenarios, there can be a *frequency offset* caused by various factors, such as differences between the transmitter and receiver oscillators or Doppler shift due to movement. If this frequency offset is not properly corrected, the received signal experiences a **progressive phase rotation**, leading to periodic distortions, as observed in the figure.
Without frequency recovery, the signal exhibits an unintended periodic pattern due to the uncompensated frequency shift. This issue negatively impacts demodulation, as the receiver struggles to maintain accurate timing with the transmitted symbols. The correlation and symbol detection processes may become distorted, leading to a decrease in the **signal-to-noise ratio (SNR)** and an increase in **symbol errors**. Moreover, as the phase drift accumulates over time, the receiver may eventually lose synchronization with the incoming signal, further degrading the overall communication performance.
To mitigate this problem, communication systems employ **frequency recovery algorithms** to estimate and compensate for frequency offsets. Common approaches include:

- **Phase-Locked Loop (PLL)** – A closed-loop control system that continuously tracks and corrects frequency differences.
- **Correlation-based algorithms** – These detect the frequency offset by analyzing repetitive patterns and applying corrections digitally.
- **Pilot-based estimation** – Using known sequences (preambles) within the signal to measure and counteract frequency shifts.

Without proper frequency recovery, the periodic behavior observed in the figure will persist, causing severe degradation in signal detection and data decoding. Implementing an effective frequency correction mechanism is crucial to ensuring stable and accurate communication
In this case, the carrier frequency offset (CFO) is estimated and corrected using a correlation-based grid search with the known preamble. The procedure can be summarized as follows:

1. **Time axis definition:** The received signal rx_signal is sampled at $f_s = M \cdot \Delta f$, and a corresponding time vector t is created.
2. **Frequency search range:** Candidate frequency offsets are defined over a range f_{range} (e.g., from -2 kHz to +2 kHz) with a chosen step size.
3. **Hypothesis testing:** For each candidate frequency $f_i \in f_{\text{range}}$, the received signal is shifted:
$$rx_{\text{corr}} = rx\_signal \cdot e^{-j2\pi f_i t}$$
and correlated with the known preamble using convolution. The correlation peak indicates the quality of alignment.

4. **CFO estimation:** The frequency maximizing the correlation peak is selected as the estimated CFO $f_{\text{offset\_est}}$:

$$f_{\text{offset\_est}} = \arg\max_i \left|\text{conv}(rx_{\text{corr}}, \text{preamble})\right|$$

5. **CFO correction:** The estimated offset is removed from the received signal:

$$rx\_signal \leftarrow rx\_signal \cdot e^{-j2\pi f_{\text{offset\_est}} t}$$

This approach is robust in the controlled coaxial cable setup, leveraging the strong correlation properties of the 3GPP-based preamble.
The correction helps reduce the periodic distortions, improving the overall signal alignment 7.4b.

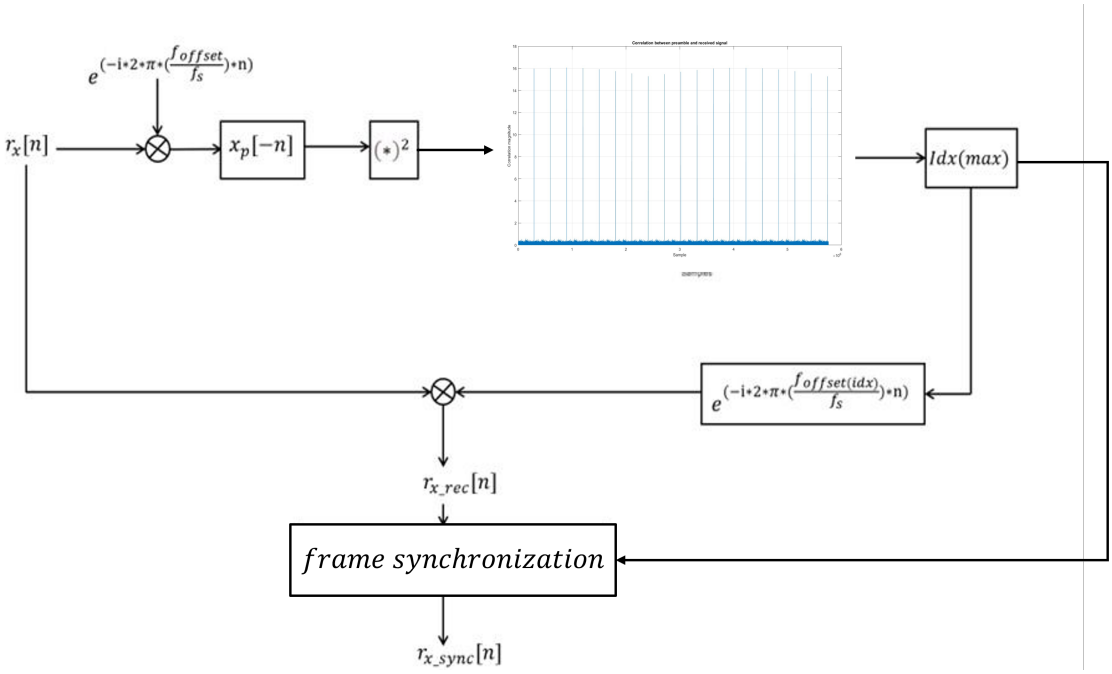

Figure 7.5: Block scheme frame synchronization + CFO estimation and correction.

7.1.4 Hardware Setup

All experiments were carried out in a controlled indoor laboratory environment.
The experiments were carried out using the following hardware:

- USRP X310 as the transmitter (TX)
- USRP X410 as the receiver (RX)
- Coaxial cable and whip antennas

7.1.5 MATLAB Toolbox for Transmission and Reception

Data transmission and reception were implemented using the MATLAB Communications Toolbox and the MATLAB Wireless Testbench, which provides pre-built system objects and workflows for prototyping and testing wireless communication systems. The following functionalities were employed:

- USRP transmitter and receiver system objects for direct control of hardware radios
- Modulation and demodulation functions to generate and process communication signals
- Signal visualization tools, including spectrum analyzers and constellation diagrams
- Synchronization and timing control to align transmission and reception

The toolbox enables real-time signal generation and reception, providing a flexible platform for testing different transmission scenarios within a controlled indoor environment. All parameters were adjusted according to the experiment configuration to ensure accurate and repeatable results.

The MATLAB Wireless Testbench was used to configure over-the-air experiments with USRP X310 and X410 radios. A `basebandTransmitter` object is created to set key transmission parameters, including the center frequency, radio gain, sample rate, and antenna port. This object allows direct control of the USRP radio from MATLAB and supports continuous transmission of signals. The transmitted waveform, an OFDM/OTFS signal loaded from a MAT-file, is first normalized to prevent hardware saturation. On the reception side, a `basebandReceiver` object is configured with matching frequency, gain, and sample rate settings, ensuring proper synchronization and reception of the transmitted signal. The `capture` function is then used to collect the received waveform over a specified time interval. After reception, `stopTransmission` halts the continuous transmission, and the received data can be stored for subsequent processing and analysis. This workflow allows for rapid experimentation with wireless signals and evaluation of transmission and reception performance without requiring low-level hardware programming.

Parameter	Symbol	Value	Unit
Number of subcarriers	M	96	–
Number of OFDM symbols	N_{sym}	781	–
Oversampling factor	L	4	–
Subcarrier spacing	Δf	15	kHz
Sampling frequency	$f_s = L \cdot M \cdot \Delta f$	57.6	MHz
Sampling period	$T_s = \frac{1}{f_s}$	173.6	ns
Guard length	$guardLen$	1000	-
Total preamble length	$N_{pre} = 192 \cdot L + 10$ (filter span) $\cdot L$	808	-
Guard interval	$T_{guard} = 2 \cdot guardLen \cdot T_{\text{s}}$	0.35	ms
Symbol duration	$T_{sym} = L \cdot M \cdot T_s = \frac{L \cdot M}{f_s} = \frac{1}{\Delta f}$	66.67	μs
Data duration	$T_{\text{data}} = N_{\text{sym}} \cdot T_{\text{sym}}$	52	ms
Frame preamble time	$T_{pre} = N_{pre} \cdot T_s$	140	μs
Total frame time	$T_{\text{tot}} = T_{\text{pre}} + T_{\text{guard}} + T_{\text{data}}$	52.5	ms

Table 7.1: OFDM Parameters and Timing Calculations

Parameter	Symbol	Value	Unit
Delay bins	M	128	–
Doppler bins	N	64	–
Pad length	$padLen$	15	–
Subcarrier spacing	Δf	15	kHz
Sampling frequency	$f_s = M \cdot \Delta f$	1.92	MHz
Sampling period	$T_s = \frac{1}{f_s}$	0.5208	ms
Guard length	$guardLen$	1000	-
Total preamble length (oversampled, L = 4)	$N_{pre} = 192 \cdot L + 10$ (filter span) $\cdot L$	808	-
Guard interval	$T_{guard} = 2 \cdot guardLen \cdot T_{\text{s}}$	1.042	ms
Subsymbol duration	$T_{subsym} = (M + padLen) \cdot T_s$	74.5	μs
Data duration	$T_{\text{data}} = N_{\text{sym}} \cdot T_{\text{subsym}}$	4.77	ms
Frame preamble time	$T_{pre} = N_{pre} \cdot T_s$	0.421	ms
Total frame time	$T_{\text{tot}} = T_{\text{pre}} + T_{\text{guard}} + T_{\text{data}}$	6.23	ms

Table 7.2: OTFS Parameters and Timing Calculations

Justification of Acquisition Duration:
The total acquisition duration of approximately one second has been chosen to ensure that several complete OFDM/OTFS frames, including guard intervals and synchronization preambles, are captured within a single measurement window. This approach guarantees statistical reliability of the demodulation process, stable synchronization, and adequate temporal resolution for signal averaging and channel estimation over multiple frames.

7.1.6 Experiment 1: Transmission via Coaxial Cable

The first experiment investigates data transmission using a direct coaxial connection between the USRP X310 and USRP X410. This configuration eliminates wireless channel effects and serves as a reference measurement for system performance.

Figure 7.6: Laboratory setup for coaxial cable transmission. USRP X310 is connected to USRP X410 via coaxial cable.

Results: OFDM

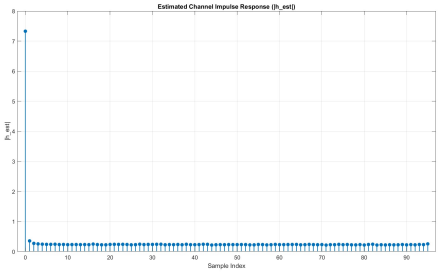

(a) OFDM – Channel estimation.

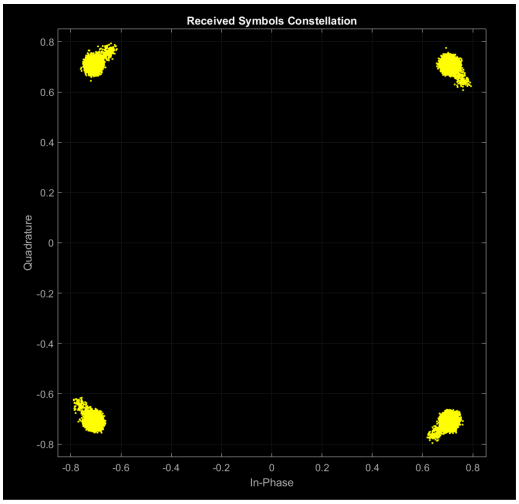

(b) OFDM – CFO and BER.

Figure 7.7: OFDM results for Experiment 1.

Results: OTFS

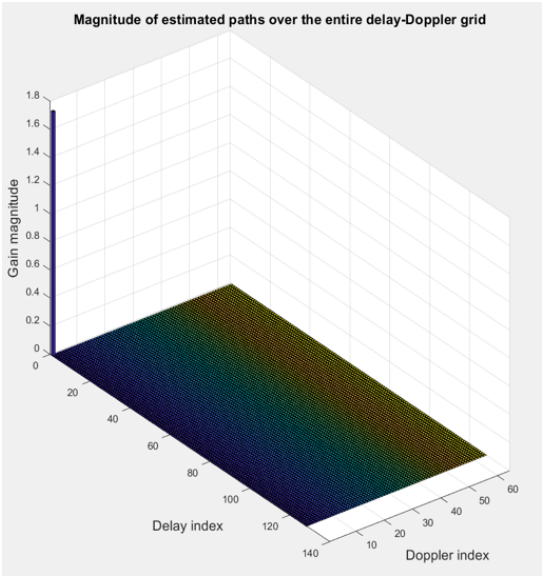

(a) OTFS – Channel estimation.

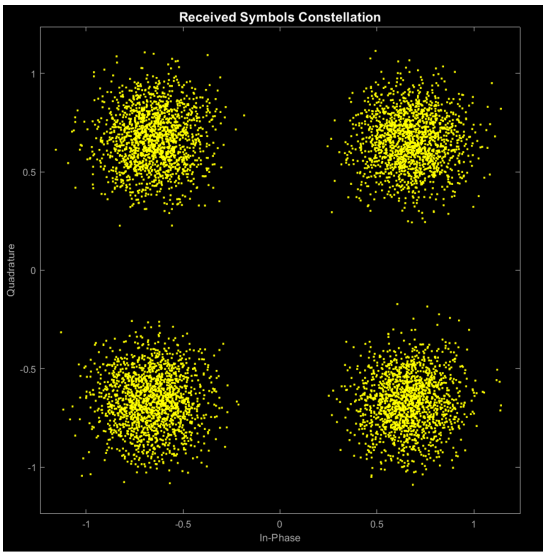


```
Estimated CFO = -820.00 Hz
BER: 0.000000e+00 (0 errors out of 3480 bits)
```

(b) OTFS – CFO and BER.

Figure 7.8: OTFS results for Experiment 1.

Discussion. For both OFDM and OTFS under coaxial transmission, the channel response is almost flat with negligible multipath. The estimated CFO is minimal, resulting in low BER. Scatterplots embedded in the CFO/BER figures show well-clustered symbols, establishing this setup as the baseline reference.

7.1.7 Experiment 2: Transmission via Antennas

Figure 7.9: Laboratory setup for wireless transmission with antennas. TX and RX are placed at a fixed distance.

Results: OFDM

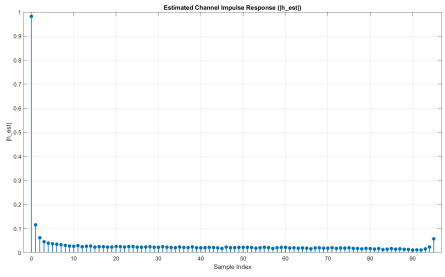

(a) OFDM – Channel estimation.

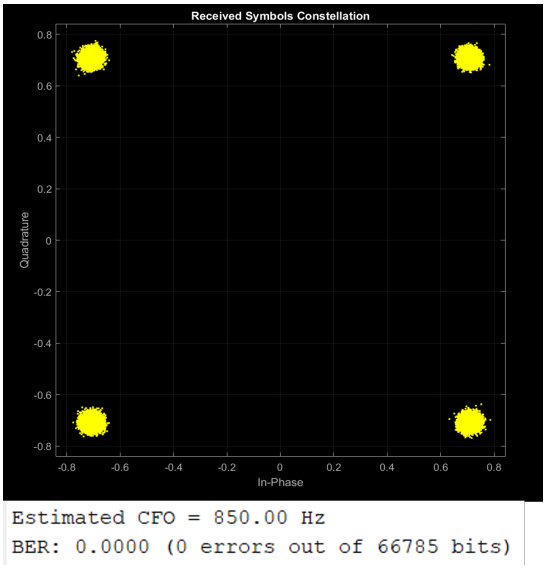

(b) OFDM – CFO and BER.

Figure 7.10: OFDM results for Experiment 2.

Results: OTFS

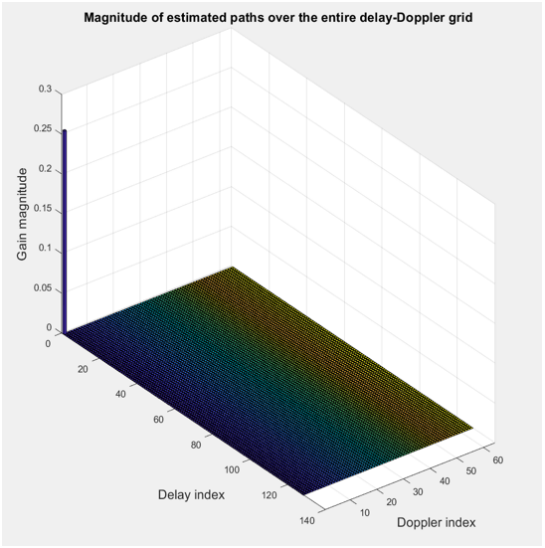

(a) OTFS – Channel estimation.

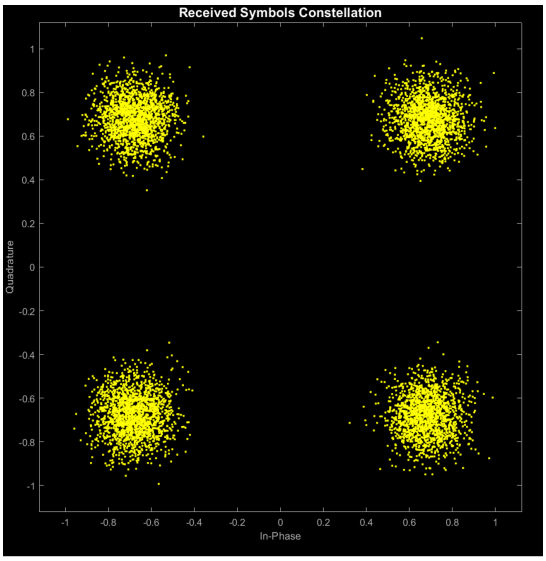


```
Estimated CFO = 3310.00 Hz
BER: 0.000000e+00 (0 errors out of 3484 bits)
```

(b) OTFS – CFO and BER.

Figure 7.11: OTFS results for Experiment 2.

Discussion. With antennas, the results are very similar to the coaxial cable case, with the line-of-sight (LOS) path clearly evident. CFO increases slightly compared to coaxial tests. Both OFDM and OTFS retain robustness, as visible in its scatterplots.

7.1.8 Experiment 3: Transmission via Antennas with Obstacles

Figure 7.12: Setup for antenna transmission with an obstacle to introduce attenuation and multipath effects.

Results: OFDM

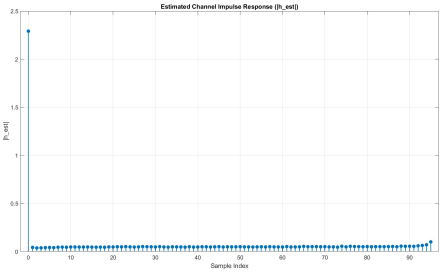

(a) OFDM – Channel estimation.

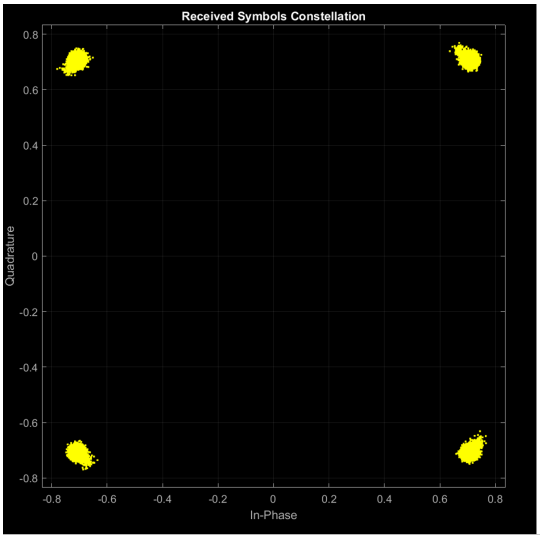

(b) OFDM – CFO and BER.

Figure 7.13: OFDM results for Experiment 3.

Results: OTFS

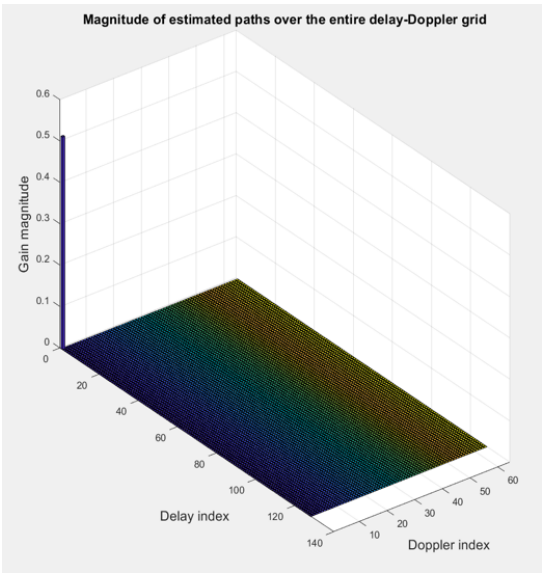

(a) OTFS – Channel estimation.

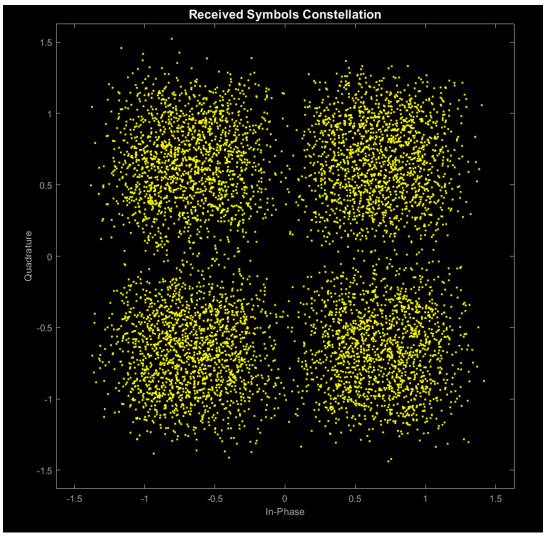


```
Estimated CFO = 3380.00 Hz
BER: 0.000000e+00 (0 errors out of 3484 bits)
```

(b) OTFS – CFO and BER.

Figure 7.14: OTFS results for Experiment 3.

Discussion. Despite the introduced obstacle, the line-of-sight (LOS) path remains clearly identifiable, and excellent performance is still achieved. CFO stays similar to previous wireless cases, and BER remains low for both schemes.

7.1.9 Experiment 4: Custom Doppler-Inducing Setup

The experimental campaign was carried out inside the laboratory by setting up a transmission and reception system designed to observe the Doppler effect. The experimental configuration consisted of a transmitter (Tx) and a receiver (Rx) aligned and both oriented towards a rotating fan. The fan served as a moving target, introducing Doppler shifts on the transmitted signal. To enhance the reflection properties and increase the backscattered power, the fan blades were covered with aluminum foil, thereby improving the effective reflection coefficient toward the receiver. The protective cage surrounding the fan was made of **plastic**, ensuring that it did not significantly interfere with the propagation of the signal. The transmission chain was implemented using a **USRP X310** software-defined radio (SDR) connected to a **VDI WR-6.5 upconverter**, while the reception chain employed a **USRP X410** SDR connected to a **VDI WR-6.5 downconverter**. Between the frequency extenders and the antennas, **waveguide attenuators** were inserted to control the transmitted and received power levels. Highly directive **horn antennas** were connected to both the upconverter and the downconverter, ensuring an efficient link budget and precise alignment between Tx and Rx. Each horn antenna exhibited a gain of approximately **20 dB**, contributing to the overall system sensitivity. Both the upconverter and downconverter required external **local oscillator (LO)** signals, whose frequencies depended on the multiplication factor specified in the manufacturer's datasheet. In transmission, the LO frequency was set to **10.517 GHz**, which, after multiplication, enabled operation at the desired **122 GHz** carrier. In reception, the LO frequency was set to **5.2585 GHz**, again according to the required multiplication factor, allowing proper downconversion of the 122 GHz carrier to the intermediate frequency (IF) handled by the USRP. The transmitted power at the output of the upconverter was set to **−6 dBm**, ensuring a sufficient signal-to-noise ratio at the receiver while preventing nonlinear effects or component saturation.

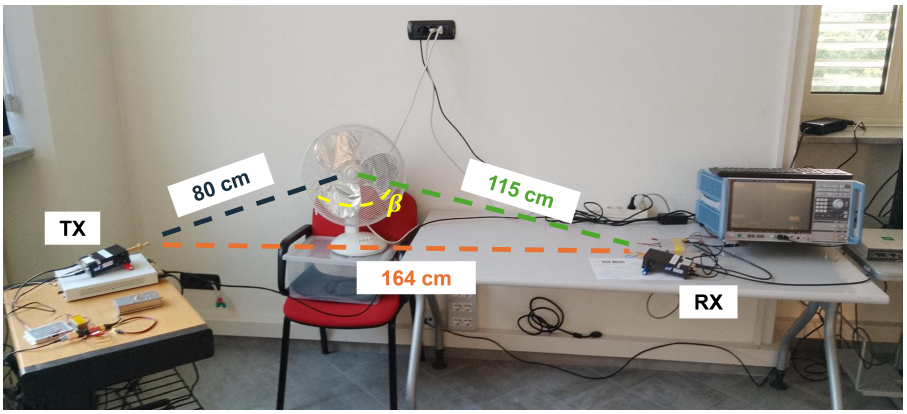

Figure 7.15: Schematic representation of the experimental setup: the Tx (USRP X310 with VDI WR-6.5 upconverter) and the Rx (USRP X410 with VDI WR-6.5 downconverter) are aligned and pointed toward a rotating fan with aluminum-covered blades to generate Doppler reflections at a carrier frequency of 122 GHz. The fan's protective cage, made of plastic, does not significantly affect signal propagation.

This setup enabled the observation and analysis of Doppler-induced frequency shifts generated by the rotating metallic blades, providing a controllable dynamic scattering scenario for evaluating the performance of the transmission and reception system.

(a) VDI WR-6.5 upconverter used in the transmission chain (TX).

(b) VDI WR-6.5 downconverter used in the reception chain (RX).

Figure 7.16: Photographs of the millimeter-wave converters used in the experiment, shown for illustrative purposes. The upconverter and downconverter are connected to highly directive antennas and driven by external LOs (10.517 GHz in TX, 5.2585 GHz in RX) to operate at a carrier frequency of 122 GHz.

Baseline Measurement with Stationary Fan

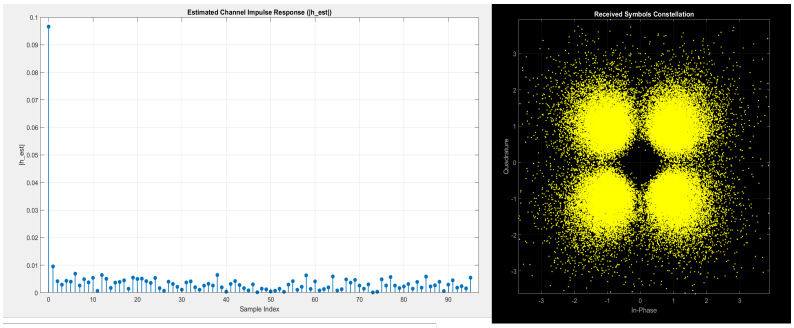

Figure 7.17: Channel estimation, data detection, and BER for OFDM under stationary fan (baseline measurement).

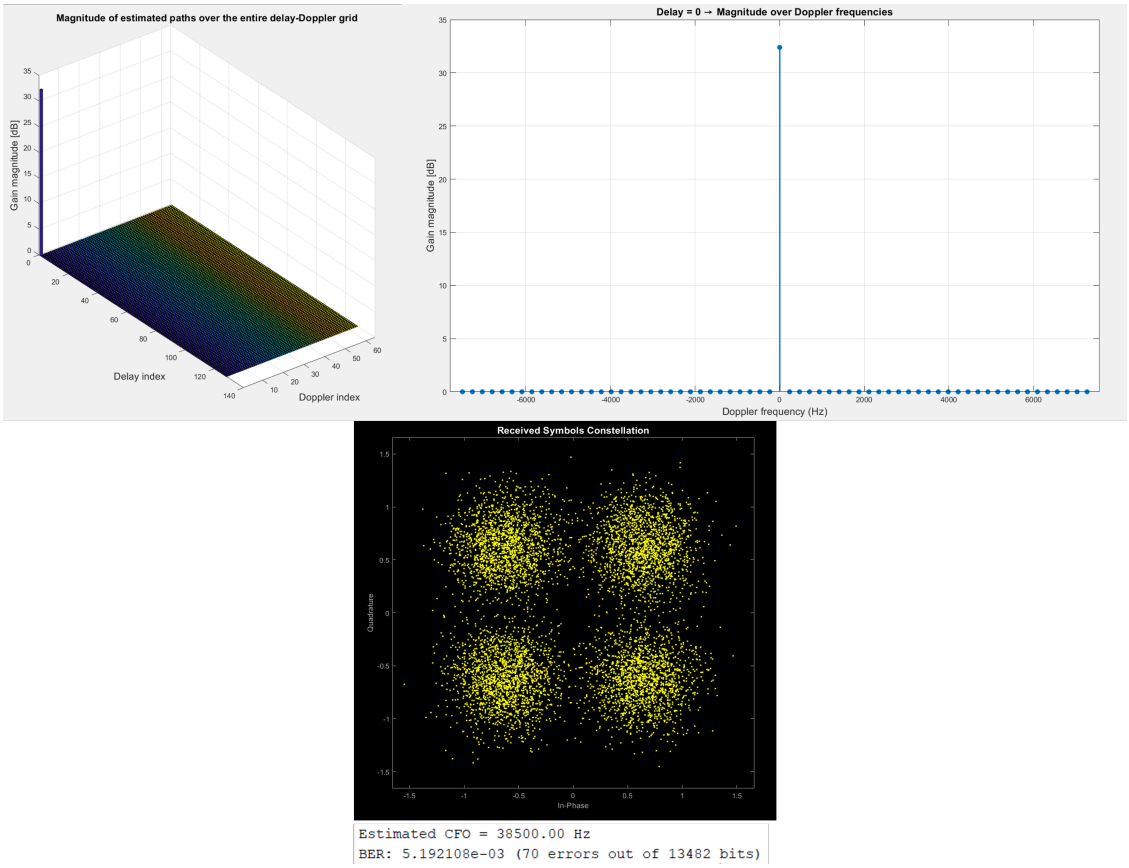

Figure 7.18: Channel estimation, data detection, and BER for OTFS under stationary fan (baseline measurement).

Intermittent Fan Rotation for Time-Varying Doppler

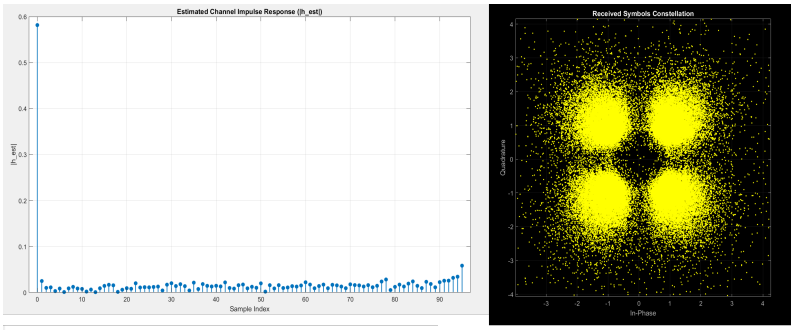

Figure 7.19: Channel estimation, data detection, and BER for OFDM with intermittent fan rotation (time-varying Doppler effect).

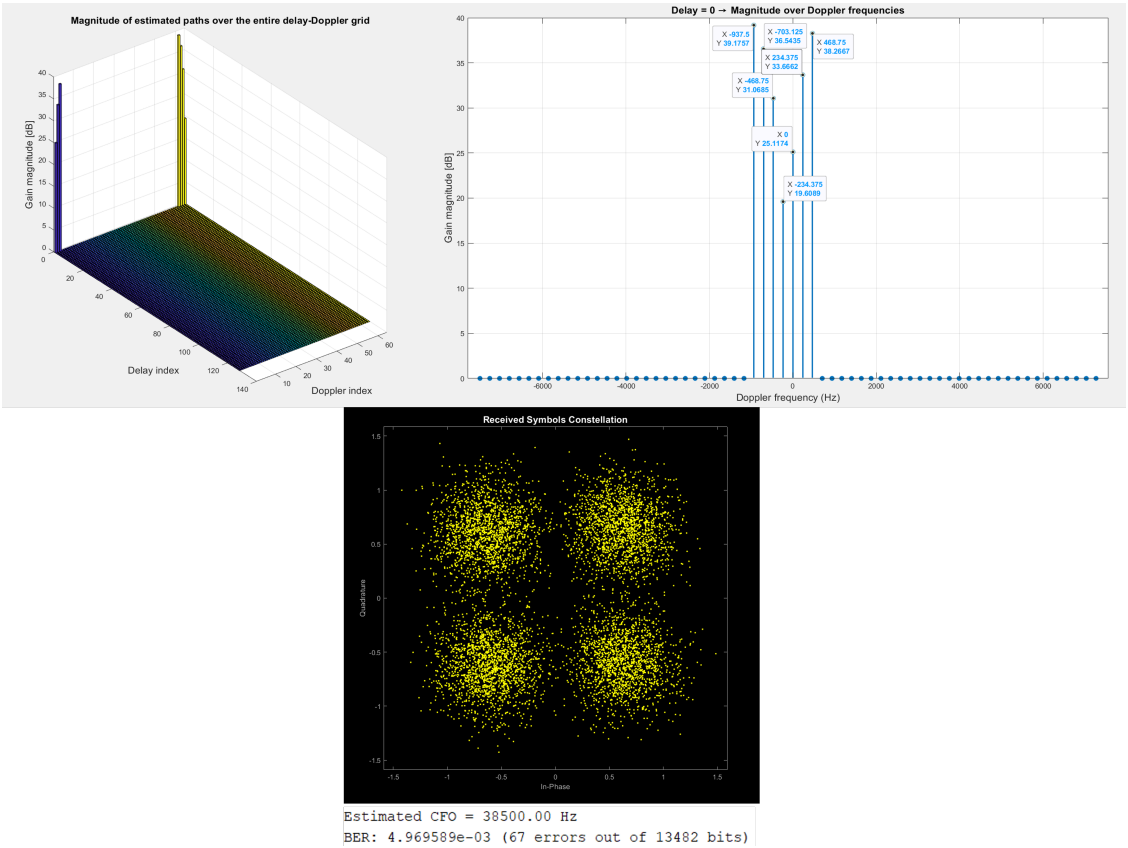

Figure 7.20: Channel estimation, data detection, and BER for OTFS with intermittent fan rotation (time-varying Doppler effect).

Continuous Fan Rotation: Dynamic Deceleration

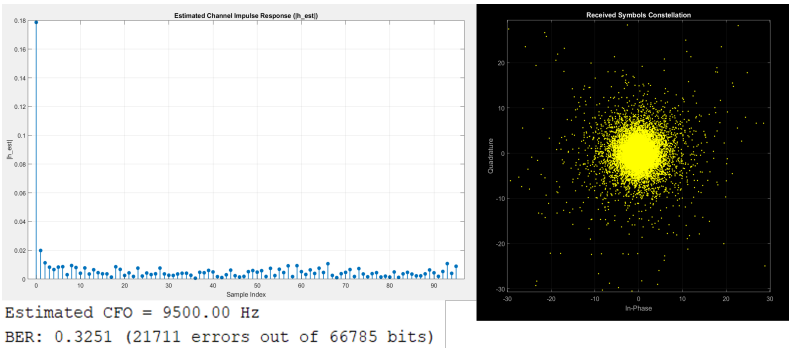

Figure 7.21: Channel estimation, data detection, and BER for OFDM with continuous fan rotation (dynamic deceleration).

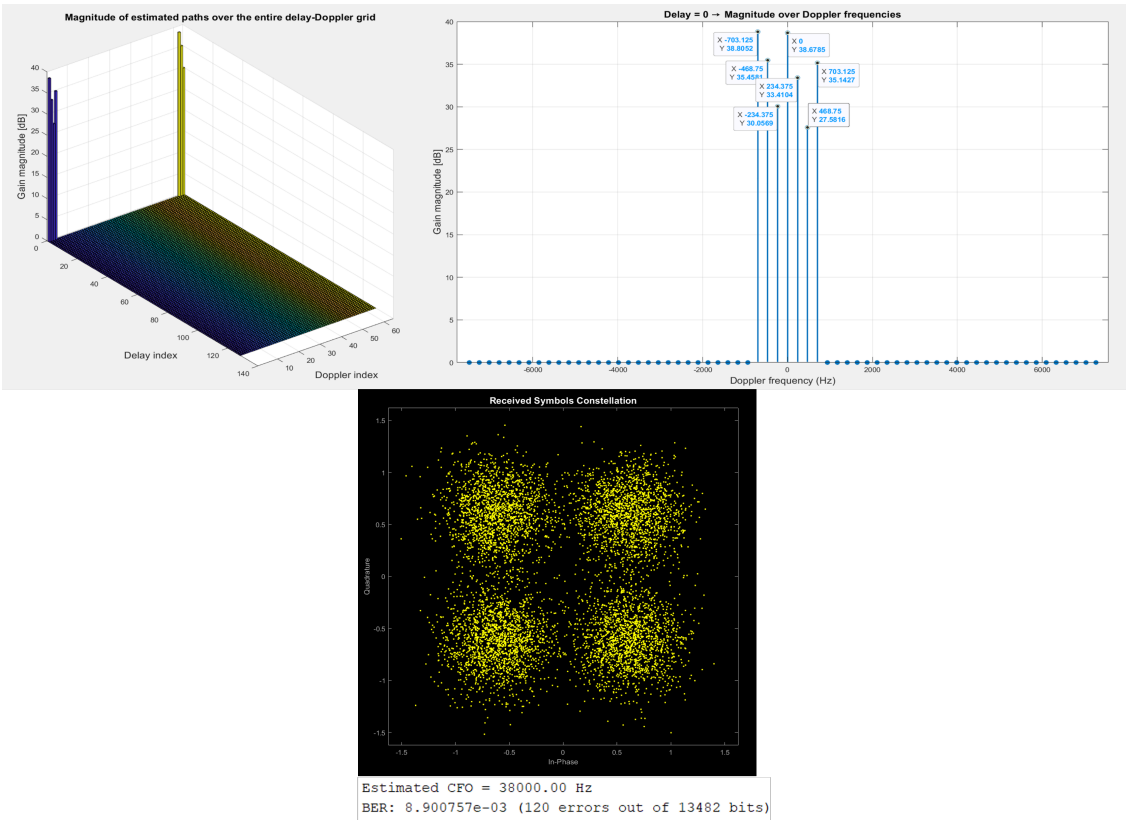

Figure 7.22: Channel estimation, data detection, and BER for OTFS with continuous low-speed fan rotation.

Comment on the Results: Across all three experiments, OTFS consistently outperforms OFDM in terms of Bit Error Rate (BER). In both the intermittent and continuous

fan operation scenarios, the presence of positive and negative (highlighted at the edges of the Doppler axis in yellow) Doppler shifts is clearly visible. In particular, when the fan rotates at around 10 revolutions per second, OTFS demonstrates its advantages by successfully performing data detection despite significant Doppler effects, whereas OFDM exhibits a single cluster and fails to resolve the channel variations. These results highlight the inherent robustness of OTFS in dynamic environments, confirming its superiority over OFDM under conditions of high mobility and Doppler dispersion.

7.2 Calculations for Understanding the Doppler Effect in the Experimental Setup

The geometric configuration of the setup is as follows:

- Distance Tx $\rightarrow$ Rx: 164 cm
- Distance Tx $\rightarrow$ Fan: 80 cm
- Distance Rx $\rightarrow$ Fan: 115 cm
- Carrier frequency: $f_0 = 122\,\text{GHz}$

Wavelength Calculation

The wavelength corresponding to the carrier frequency is:

$$\lambda = \frac{c}{f_0} = \frac{3 \times 10^8\,\text{m/s}}{122 \times 10^9\,\text{Hz}} \approx 2.46 \times 10^{-3}\,\text{m}$$

Fan Blade Tip Velocity

The fan has a blade radius:

$$r = 0.2\,\text{m}$$

- Rotation speed case 1: $f_{\text{rot}} = 1\,\text{rev/s}$
- Rotation speed case 2: $f_{\text{rot}} = 10\,\text{rev/s}$

The linear velocity at the blade tip is:

$$v_{\text{tip}} = 2\pi r f_{\text{rot}}$$

- Case 1: $v_{\text{tip}} \approx 1.2566\,\text{m/s}$
- Case 2: $v_{\text{tip}} \approx 12.566\,\text{m/s}$

Monostatic Doppler Frequency

The monostatic Doppler shift is:

$$f_D^{\text{mono}} = \frac{2v_{\text{tip}}}{\lambda}$$

- Case 1: $f_D^{\text{mono}} \approx 1021.62\,\text{Hz}$
- Case 2: $f_D^{\text{mono}} \approx 10216.26\,\text{Hz}$

Bistatic Geometry

The angle β at the scatterer (fan) is calculated using the law of cosines:

$$\cos\beta = \frac{80^2 + 115^2 - 164^2}{2 \cdot 80 \cdot 115} \approx -0.38516$$

$$\beta \approx \arccos(-0.38516) \approx 1.977\,\text{rad} \approx 113.28^\circ$$

The bistatic Doppler shift is then:

$$f_D^{\text{bist}} = f_D^{\text{mono}} \cdot \cos\left(\frac{\beta}{2}\right)$$

- Case 1: ${f_D^{\text{bist}}}_{max} \approx 562\,\text{Hz}$
- Case 2: ${f_D^{\text{bist}}}_{max} \approx 5.618\,\text{KHz}$

Therefore, the Doppler shift due to the rotating fan can appear in the interval:

$$f_D \in [-{f_D^{\text{bist}}}_{max}, +{f_D^{\text{bist}}}_{max}]$$

for both rotation speeds.

Considerations for OTFS

The subcarrier spacing adopted in the OTFS system is:

$$\Delta f = 15\,\text{kHz}$$

The Doppler resolution of the OTFS grid, determined by the number of Doppler bins N and the OFDM symbol duration $T_s = 1/\Delta f$, is:

$$\Delta\nu = \frac{1}{NT_s} = \frac{\Delta f}{N}$$

For the adopted parameters ($N = 64$, $\Delta f = 15\,\text{kHz}$):

$$\Delta\nu \approx 234.375\,\text{Hz}$$

Doppler Bin Index and Expected Behaviour

The OTFS Doppler grid used consists of 64 Doppler bins with a resolution of 234 Hz, thus covering an overall Doppler interval of approximately 15 kHz, i.e., ±7.5 kHz split between negative and positive frequencies.
In the signal reflected from the rotating fan, approximately 4 positive and 4 negative bins can be observed, corresponding to the central portion of the Doppler distribution generated by the blades. Since the theoretical maximum Doppler shift is calculated to lie between 5 and 11 kHz, the extreme peaks are not fully resolved. However, the majority of the Doppler energy is captured by the central bins.
This observation confirms that OTFS correctly detects the velocity variations due to the blade rotation, even though with limited resolution for the most extreme peaks—those generated by the tips of the blades. Therefore, the focus of the measurement remains on the larger and slower-moving regions of the blades, which contribute the majority of the reflected signal energy.
In this work, the analysis focuses primarily on the Doppler domain rather than on the delay axis. The delay resolution in OTFS is defined as

$$\Delta\tau = \frac{1}{M\,\Delta f},$$

where M denotes the number of delay bins and $\Delta f = 15$ kHz is the subcarrier spacing. For $M = 128$, the resulting delay resolution is

$$\Delta\tau = \frac{1}{128 \times 15 \times 10^3} \approx 0.53\ \mu\text{s}.$$

The experimental geometry yields a direct path length of $L_{\text{direct}} = 1.64$ m (TX $\rightarrow$ RX) and a reflected path via the fan of $L_{\text{refl}} = 0.80 + 1.15 = 1.95$ m. The resulting path difference is $\Delta d_{\text{path}} = 0.31$ m, corresponding to a delay difference

$$\Delta\tau = \frac{\Delta d_{\text{path}}}{c} \approx \frac{0.31}{3 \times 10^8} \approx 1.03\ \text{ns}.$$

Given the system's delay resolution of approximately 0.53 μs (i.e., $\sim$ 530 ns), this delay difference is far below the resolution limit and therefore the reflected and direct components are not separable along the delay axis. Consequently, delay-domain discrimination of the fan reflection is not feasible with the current bandwidth; analysis is therefore focused on Doppler-domain effects.

Chapter 8

Conclusion

This thesis has provided a comprehensive comparative study between OFDM and OTFS modulation schemes within the context of emerging 6G communication systems. The analysis has demonstrated that OTFS offers significant potential advantages over OFDM, particularly in environments characterized by high mobility and pronounced Doppler effects, due to its inherent resilience to time-frequency variations. Through extensive simulations and experimental evaluations conducted in an indoor laboratory setting, key performance trends have been observed, highlighting scenarios where OTFS can outperform conventional OFDM.

Nevertheless, it is important to recognize the limitations inherent to this study. The indoor experimental environment naturally constrains the creation of significant Doppler spreads, which are critical to fully assess OTFS's capabilities. Therefore, the research could be greatly expanded by conducting additional experiments in more realistic and dynamic conditions, including outdoor deployments, as well as by varying signal durations, grid configurations, and guard band dimensions. Fine-tuning these parameters would enable the collection of a richer set of performance metrics and offer a more complete understanding of the relative strengths and weaknesses of both modulation schemes.

Moreover, while this work has highlighted the promising potential of OTFS, in my view, the technology still requires a substantial period of focused research before it can realistically achieve widespread adoption and potentially surpass OFDM in practical applications. Discovering its advantages is only the first step; significant efforts remain necessary to optimize system design, standardize implementations, and ensure reliable performance across diverse operational scenarios.

In conclusion, this thesis lays the groundwork for further exploration of OTFS in 6G contexts and provides a foundation upon which future research can build to fully realize the capabilities of this emerging modulation scheme. The journey toward standardization and real-world deployment is long, but the insights gained here affirm that OTFS is a promising candidate worthy of continued investigation.

Bibliography

[1] Mahmoud Aldababsa, Güneş Karabulut Kurt, Serdar Özyurt, and Oğuz Kucur. A survey on orthogonal time frequency space modulation. *IEEE Open Journal of the Communications Society*, 2024. Received 22 May 2024; accepted 21 June 2024; published 3 July 2024; current version 1 August 2024.

[2] Suvra Sekhar Das. *Techniques to Enhance Spectral Efficiency of OFDM Wireless Systems*. Ph.d. dissertation, Aalborg University, Aalborg, Denmark, 2007. Presented to the International Doctoral School of Technology and Science in partial fulfillment of the requirements for the degree of Doctor of Philosophy.

[3] European Telecommunications Standards Institute (ETSI). Universal mobile telecommunications system (umts); physical channels and mapping of transport channels onto physical channels (tdd). 2001.

[4] Iain Explains. Iain explains - youtube channel. YouTube Channel, 2023. Accessed: 2025-04-06.

[5] Roberto Garello. Communication and network systems. Course lectures, Politecnico di Torino, 2023. Academic year 2023-2024, Unpublished material.

[6] Lorenzo Gaudio, Giulio Colavolpe, and Giuseppe Caire. Otfs vs. ofdm in the presence of sparsity: A fair comparison. *IEEE Transactions on Wireless Communications*, 21(6):4401–4415, June 2022.

[7] Yi Hong, Tharaj Thaj, and Emanuele Viterbo. *Delay-Doppler Communications: Principles and Applications*. Elsevier, 2022.

[8] Shihao Ju, Yunchou Xing, Ojas Kanhere, and Theodore S. Rappaport. Sub-terahertz channel measurements and characterization in a factory building. In *2022 IEEE International Conference on Communications (ICC)*, pages 1–6, Brooklyn, NY, USA, 2022. IEEE.

[9] Oltjon Kodheli. Ofdm-based schemes for next generation wireless systems. Master's thesis, Alma Mater Studiorum - University of Bologna, Bologna, Italy, 2016. Master of Science in Electronic Engineering, II Session, Academic Year 2015/2016.

[10] Shuangyang Li. *Orthogonal Time Frequency Space (OTFS) Modulation for Wireless Communications*. Phd thesis, The University of New South Wales, 2022. Faculty of Engineering, School of Electrical Engineering and Telecommunications, submitted in August 2022.

[11] Lorenzo Luzzo. Otfs modulation for isac: Waveform analysis and radar system implementation based on pilot frames. Master's thesis, University of Pisa, 2024. Academic year 2023–2024.

[12] Abderrahim Mohammadi, Saad Chakkor, Ahmed El Oualkadi, Mohamed Moussaoui, Aziz Dkiouak, and Mostafa Baghouri. Performance evaluation of otfs and ofdm for 6g waveform. *Journal Name*, 2023. LabTIC, ENSA of Tangier, University of Abdelmalek Essaâdi, and collaborators from ENSA Tetouan and ENSAM Casablanca. Results based on MATLAB simulations.

[13] Mounika Siluveru, Dharavath Nanda, and RadhaKrishna Karne. Study and analysis of otfs and ofdm. *Journal of Artificial Intelligence, Machine Learning and Neural Network*, 2(6):13–23, Oct–Nov 2022. Received: 08 August 2022; Accepted: 24 October 2022; Published: 28 November 2022.

[14] Yao Xiao. Orthogonal frequency division multiplexing modulation and inter-carrier interference cancellation. Master's thesis, Louisiana State University and Agricultural and Mechanical College, Baton Rouge, Louisiana, 2003. Part of the Electrical and Computer Engineering Commons.

[15] Orestis Zekai. Study and sdr implementation of ofdm modulation, 2017. Submitted in fulfillment of the requirements for the degree of BSc in Engineering, Department of Electrical and Computer Engineering.